

INFORMATION TO USERS

This manuscript has been reproduced from the microfilm master. UMI films the text directly from the original or copy submitted. Thus, some thesis and dissertation copies are in typewriter face, while others may be from any type of computer printer.

The quality of this reproduction is dependent upon the quality of the copy submitted. Broken or indistinct print, colored or poor quality illustrations and photographs, print bleedthrough, substandard margins, and improper alignment can adversely affect reproduction.

In the unlikely event that the author did not send UMI a complete manuscript and there are missing pages, these will be noted. Also, if unauthorized copyright material had to be removed, a note will indicate the deletion.

Oversize materials (e.g., maps, drawings, charts) are reproduced by sectioning the original, beginning at the upper left-hand corner and continuing from left to right in equal sections with small overlaps. Each original is also photographed in one exposure and is included in reduced form at the back of the book.

Photographs included in the original manuscript have been reproduced xerographically in this copy. Higher quality 6" x 9" black and white photographic prints are available for any photographs or illustrations appearing in this copy for an additional charge. Contact UMI directly to order.

UMI[®]

Bell & Howell Information and Learning
300 North Zeeb Road, Ann Arbor, MI 48106-1346 USA
800-521-0600

**TEXTURAL AND STRUCTURAL DEVELOPMENT
OF OBSIDIAN LAVAS**

by

JONATHAN MICHAEL CASTRO

A DISSERTATION

**Presented to the Department of Geological Sciences
and the Graduate School of the University of Oregon
in partial fulfillment of the requirements
for the degree of
Doctor of Philosophy**

June 1999

UMI Number: 9940394

**Copyright 1999 by
Castro, Jonathan Michael**

All rights reserved.

**UMI Microform 9940394
Copyright 1999, by UMI Company. All rights reserved.**

**This microform edition is protected against unauthorized
copying under Title 17, United States Code.**

UMI
300 North Zeeb Road
Ann Arbor, MI 48103

"Textural and Structural Development of Obsidian Lavas," a dissertation prepared by Jonathan M. Castro in partial fulfillment of the requirements for the Doctor of Philosophy degree in the Department of Geological Sciences. This dissertation has been approved and accepted by:

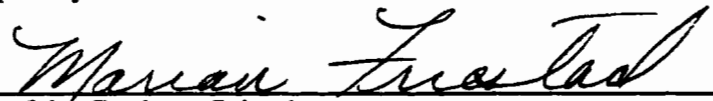


Dr. Katharine V. Cashman

6-1-99
Date

Committee in charge: Dr. Katharine V. Cashman, Chair
 Dr. A. Dana Johnston
 Dr. Michael Manga
 Dr. Kenneth Doxsee

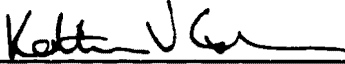
Accepted by:



Dean of the Graduate School

© 1999 Jonathan Michael Castro

An Abstract of the Dissertation of
Jonathan Michael Castro for the degree of Doctor of Philosophy
in the Department of Geological Sciences to be taken June 1999
Title: TEXTURAL AND STRUCTURAL DEVELOPMENT OF OBSIDIAN
LAVAS

Approved: 
Dr. Katharine V. Cashman

Rhyolitic obsidian flows were emplaced as recently as 500 years ago in California and 1300 years ago in Oregon, and yet have not been observed to erupt in historic times. This dissertation presents constraints on the physical volcanologic processes governing the structural and textural development of several late-Holocene obsidian flows in California and Oregon, and consists of three major studies, each drawing from textures and structures preserved on three different scales of observation.

Microlite abundance, size, shape, and orientation distributions were measured in obsidian from the flow, conduit, and dike of Obsidian Dome, California, to quantify syn-eruptive crystallization and flow. Microlite number densities and size distributions suggest an initial phase of nucleation-dominated crystallization of pyroxene and plagioclase, followed by growth-dominated plagioclase crystallization with continued pyroxene nucleation and growth. Microlite orientation distributions in the flow front correlate with the inferred flow direction and suggest that early extrusion took place from an elongate vent. Orientation distributions also indicate that simple shear strains increase from

approximately 2.4 in the dike to 3.3 on the flow surface and suggest that microlite alignment occurs mostly in the dike.

Mesoscopic single and multilayer folds form during flow emplacement by buckling of obsidian in a matrix of pumice. Buckling forms a continuum of fold styles which is controlled by the thickness ratio of pumice to obsidian. All folds indicate that bubble-free rhyolite is more viscous than bubbly rhyolite. Wavelength-to-thickness ratios of single-layer folds indicate shear viscosity ratios of approximately 10-500 based on Newtonian rheologies. Shear viscosity ratios based on power law rheologies may be more than an order of magnitude less than Newtonian estimates.

Large cavities were mapped on the Big Obsidian Flow, Oregon as a means of determining the link between large scale surface folding and hazardous explosive activity originating from within the flow. Structural analysis indicates that cavities are near cylindrical folds formed during thin-skinned detachment folding of the flow surface. Explosion pits are correlated spatially with both cavities and large surface folds and may form as a result of flow induced deformation.

CURRICULUM VITA

NAME OF AUTHOR: Jonathan Michael Castro

PLACE OF BIRTH: Sacramento, California

DATE OF BIRTH: November 22, 1969

GRADUATE AND UNDERGRADUATE SCHOOLS ATTENDED:

University of Oregon
Humboldt State University

DEGREES AWARDED:

Doctor of Philosophy in Geological Sciences, 1999, University of Oregon
Bachelor of Science, Geology, 1993, Humboldt State University

AREAS OF SPECIAL INTEREST:

Physical Volcanology
Silicic Lava Dynamics

PROFESSIONAL EXPERIENCE:

Graduate Teaching Fellow, Department of Geological Sciences, University of Oregon, Eugene, 1993-1998

Graduate Research Assistant, Department of Geological Sciences, University of Oregon, Eugene, 1998-1999

AWARDS AND HONORS:

Geological Society of America, Grant-in-Aid of Research, 1995
Geological Society of America, Grant-in-Aid of Research, 1996
Sigma Xi, Grant-in-Aid of Research, 1995

PUBLICATIONS:

- Castro, J.M., 1993. Petrography of the Eltapom Ophiolite Remnant, Rattlesnake Creek Terrane, western Klamath Mountains California. Senior Thesis, Humboldt State University.
- Castro, J.M., and Cashman, K.V., 1995. Strain Partitioning in Obsidian Dome, Eastern California. Geological Society of America, Abstract with Programs.
- Castro, J.M., and Cashman, K.V., 1996. Rheologic Behavior of Obsidian and Coarsely Vesicular Pumice in Little Glass Mountain and Obsidian Dome, California. EOS v.77.
- Castro, J. and Cashman, K.V., 1999. Constraints on rheology of obsidian and pumice based on folds in obsidian lavas. *The Journal of Structural Geology* 21, 807-819.
- Castro, J.M., Manga, M., and Cashman, K.V., 1997. Field-based and Numerical Investigation of the Rheology of Bubble-bearing Lavas. Geological Society of America, Abstract with Programs.
- Castro, J.M., Manga, M., Olmstead, B., and Cashman, K.V., 1998. Textural Development of Obsidian Domes. EOS v.79.
- Manga, M., Castro, J.M., Cashman, K.V., and Loewenberg, M., 1998. Rheology of bubble-bearing magmas. *Journal of Volcanology and Geothermal Research* 87, 15-28.

ACKNOWLEDGEMENTS

I dedicate this work to my parents. My mother and father gave me never-ending support through the difficult and smooth parts of this journey. Thanks to Jason and Jeff for providing inspiration. Katharine V. Cashman and Michael Manga were an integral part of my growth as a scientist and professional. I am grateful for their support on all levels and benefited from our many meetings and classes. I am especially thankful for their encouragement during the early stages of this project, when our questions greatly outweighed explanations. Thank you A. Dana Johnston for your guidance from the start of this program. My heartfelt thanks to Bretagne Hygelund, for your support, companionship, training, tutoring, caring and sharing, and being a truly wonderful friend. Thanks goes out to everyone in touch with me during this six-year-long trek towards a dream in my life: Chris, Nick, Brian, Brando, Leroy, Ellen, John Longshore, the Hemphill-Haleys, Mr. Kenney, Bud Burke.

TABLE OF CONTENTS

Chapter	Page
I. INTRODUCTION	1
Background	3
II. MICROLITE CRYSTALLIZATION AND ORIENTATION DISTRIBUTION IN OBSIDIAN DOME, CA	8
Introduction	8
Geologic Background	9
Sample Collection	9
Measurement Techniques	11
Crystal Size Distributions	17
Results	19
Discussion	60
Summary	78
III. CONSTRAINTS ON RHEOLOGY OF OBSIDIAN FLOWS BASED ON MESOSCOPIC FOLDS	83
Introduction	83
Rheologic Background	84
Mesoscale Deformation in Obsidian Flows	84
Results	103
Discussion	105
Conclusions	112
IV. STRUCTURAL RELATIONS OF LARGE CAVITY STRUCTURES IN THE BIG OBSIDIAN FLOW, NEWBERRY VOLCANO, OR	116
Introduction	116
Geologic Background	117
Methods	120
Results	123
Discussion	138
Summary	143
V. SUMMARY AND CONCLUSIONS	150

Page

APPENDIX 154

REFERENCES 156

LIST OF FIGURES

Figure	Page
1. Location Map of California, Oregon, and Washington Showing Recent Obsidian flows	2
2. Schematic View of a Rhyolitic Obsidian Eruption.	4
3. Backscattered Electron Images of CVP, FVP, Obsidian, and Vent Facies Rhyolite	6
4. Textural Stratigraphy as Determined by Drill Cores Through Holocene Obsidian Domes	7
5. Map of Obsidian Dome, CA, Showing the Locations of Flow Front Samples and Approximate Drill Core Locations.	10
6. AutoCAD Drawing of Microlites in Obsidian.	13
7. Backscattered Electron Image of Conduit Sample C-1 Showing Rod-Shaped Pyroxene Microlites.	15
8. Backscattered Electron Image of Obsidian Showing the Technique for Measuring Microphenocrysts	16
9. Comparison of Crystal Size Distributions (CSD) for Plagioclase Microphenocrysts.	20
10. Photomicrographs of Obsidian from the Flow Front, Dike, and Shallow Vent	21
11. Microlites in Plane Polarized Light and Back Scattered Electron Imaging.	23
12. Microlitic Obsidian in Plane Polarized Light and Reflected Light.	24
13. BSE Images of Obsidian from the Flow Front, Dike, and Shallow Vent.	25
14. Energy Dispersive X-Ray Spectra for Pyroxene and Plagioclase Microlites.	26
15. Photomicrograph of Obsidian from the Dike.	27
16. Log N_a for Microlites in the Dike Conduit, and Flow Front.	30

17. Microlite Number Density Versus Volume Fraction.	32
18. Mean Microphenocryst Number Per Area Versus Length for Pyroxene and Plagioclase	33
19. Aspect Ratio Histogram for Plagioclase Microphenocrysts	37
20. Aspect Ratio Histogram for Pyroxene Microphenocrysts.	38
21. Microlite Size Histograms for the Flow Front, Dike, and Shallow Vent.	40
22. Individual Flow Front length Distributions	42
23. Plagioclase Microphenocryst Length and Width Histograms	43
24. CSD for Microlites in Flow Front Sample OD9.	46
25. Individual Microlite CSDs for Flow Front Samples.	48
26. CSD for Microlites in all Flow Front Samples.	49
27. CSD for Dike Samples.	51
28. CSD for the Shallow Vent Sample.	52
29. CSD for Plagioclase Microphenocrysts in Flow Front Samples	54
30. CSD for Plagioclase Microphenocrysts in Flow Front Samples	55
31. CSD for Plagioclase Microphenocrysts in the Dike.	56
32. Microlite Orientations in Flow Front Samples.	57
33. Microlite Orientation in the Conduit and Dike of Obsidian Dome	61
34. CSDs for Flow Front, Dike, and Vent Samples.	64
35. Crystallization Kinetics for Plutonic and Volcanic Regimes	67
36. Plagioclase Microphenocryst CSDs for the Dike and Flow Front.	69
37. CSDs for Plagioclase Microlites in Dike Samples and Microphenocrysts in the Flow Front.	70
38. Obsidian Dome and the Inferred Trace of the Subsurface Feeder Dike Showing Mean Microlite Lineation Directions	76
39. Standard Deviation of Microlite Trend Versus Strain for Rods of Aspect Ratio 5 for Simple and Pure Shear Flows.	77

40. Pure Shear Strain Calculation for Surface Flow.	79
41. Schematic View of Microlite Orientation Development in Obsidian Dome.	82
42. Map Showing the Location of Little and Big Glass Mountain Obsidian Flows (LGM and BGM Respectively) on the Medicine Lake Volcano, CA.	86
43. Upright and Recumbent Folds in Interlayered Obsidian and Coarsely Vesicular Pumice at Big Glass Mountain, California..	87
44. Oblique View of Mesoscopic Deformation Features in Poorly Vesicular Rhyolite and Finely Vesicular Pumice.	89
45. Three Types of Flow Layering in Obsidian Lavas.	90
46. Single and Multi-layered Glassy Folds in Coarse Pumice.	91
47. Boudinage of Glassy Rhyolite within Finely Vesicular Pumice.	93
48. Parasitic Glassy Folds in Coarse Pumice.	95
49. Photomicrograph of Pumice in Contact with a Folded Obsidian Layer	96
50. Tracings of Glassy Folds Ranging From Multilayered Harmonic, Disharmonic, to Single-Layer Ptygmatic.	97
51. Phase Diagram of Multilayered and Single Layer Folds.	99
52. Photomicrograph of a Single-Layer Obsidian Buckle Fold and its Pumiceous Matrix.	100
53. Vertical Exposure of a Folded Obsidian Layer in Coarsely Vesicular Pumice from Big Glass Mountain, California	102
54. Plot of Dominant Wavelength Versus Competent Layer Thickness for 73 Folds from Big and Little Glass Mountains, CA.	108
55. Distribution of Normalized Wavelength of Folds from Big and Little Glass Mountains, and Obsidian Dome, CA	109
56. Normalized Wavelength plotted against the Shear Viscosity Ratio for Newtonian Folds.	113
57. Relative Viscosity Versus Matrix Porosity.	114
58. Location of Newberry Volcano and the Big Obsidian Flow.	119
59. Oblique Aerial View of the Big Obsidian Flow.	121

60. Aerial Photograph Mosaic of the Big Obsidian Flow.	122
61. Explosion Pit on the Surface of the Big Obsidian Flow.	124
62. Cavity Structures G and A.	125
63. Topographic Map of the Big Obsidian Flow Showing the Locations of Several Explosion Pits Mapped by Jensen (1993).	126
64. Cavity Structure Cross Sections.	127
65. Flow Layering in Obsidian Over Cavity SNJ.	130
66. Platy flow Layered Obsidian from the Roof of Cavity G	132
67. Mesoscopic Pull-Apart Fold on the Roof of Cavity SNJ.	133
68. Linear Structures on Cavity Walls	134
69. Sample of Obsidian from Cavity A Showing Both Chattermarks and Striations	136
70. Lower Hemisphere Stereographic Projections.	137
71. Digital Elevation Model of Cavity A.	139
72. Illustration of a Superposed Deformation Experiment Conducted by Ghosh et al. (1993)	142
73. Mesoscopic Pull-Apart Fold in Interlayered Obsidian and Pumice.	144
74. Topographic Map and Aerial Photo Mosaic of the Big Obsidian Flow.	146
75. Schematic Model of the Formation of Cavity Structures	148
76. Circular and Elliptical Explosion Pits (Outlined) on the Surface of Big Glass Mountain, CA.	149
77. Cross Section of Distal Obsidian Dome.	153

LIST OF TABLES

Table	Page
1. Measured Microlite Properties in Flow Front, Dike, and Conduit Samples	29
2. Measured Microphenocryst Properties	35
3. CSD Parameters for Obsidian Dome Microlites	45
4. CSD Parameters for Plagioclase Microphenocrysts.	58
5. Measured Microlite Number Density and N_T Calculated from CSDs	59
6. Measured and Computed Parameters on Obsidian Folds from Big and Little Glass Mountains, CA.	106
7. Shear Viscosity Ratios of Folded Obsidian Layers and Pumiceous Matrices from Big and Little Glass Mountains, CA.	111
8. Mesoscopic Structures Found in Cavity Structures	129

CHAPTER I

INTRODUCTION

Obsidian domes and flows are a significant part of the late Holocene volcanic record in the Pacific Northwest. Glassy rhyolitic lavas erupted as recently as 1912 in Alaska, and have erupted at least 6 times in Oregon and California during the past 2000 years (Figure 1). Because "no geologist has ever witnessed an obsidian in motion" (Nichols, 1941), knowledge of eruptive timescales and the physical volcanologic processes governing their emplacement is limited. Meanwhile, dacite and andesite dome eruptions have proven to be extremely hazardous (e.g., Merapi, Indonesia; Mt. Unzen, Japan, Mt. St. Helens, USA; Soufriere Hills, Montserrat), and pyroclastic activity associated with their emplacement has claimed many lives. Given that the likelihood of another obsidian dome eruption in the western United States is high, efforts have been made to better understand their crystallization histories (e.g., Swanson et al., 1989), modes of degassing (e.g., Fink et al., 1992), rheology (e.g., Stevenson et al., 1993), and deformation style (e.g., Smith and Houston, 1994). These studies have primarily involved direct physical examination of textures and structures preserved in lavas. In a similar approach, this dissertation was conducted as a means of quantifying the (1) timescales of crystallization and flow, (2) rheologic properties, and (3) large scale deformation mechanisms of obsidian lavas. The projects comprising this dissertation consist of quantitative measurements of textures and structures preserved on microscopic, mesoscopic, and macroscopic scales.

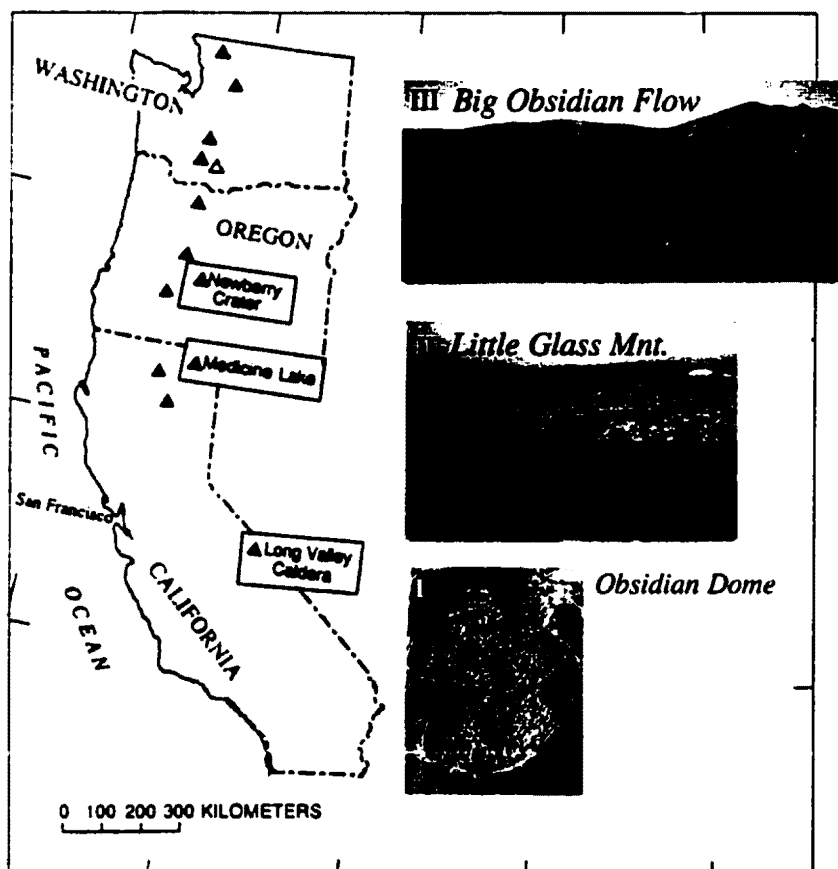


Figure 1. Location map of California, Oregon, and Washington showing recent obsidian flows. Modified from Brantley (1995).

In chapter II, I present a study of microlite crystallization and flow in the Obsidian Dome system, California. This project integrates measured microlite size and orientation data to estimate the timescales of crystallization and flow of the late Holocene Obsidian Dome complex. Estimating eruption rates is an essential component of hazards assessment involving emplacement of silicic magmas. Chapter III consists of an analysis of mesoscopic folds and boudinage in the Big and Little Glass Mountain obsidian flows. Analysis of mesoscopic structures yields insights into both the deformation mechanisms and relative rheologic properties of obsidian lavas. A kinematic analysis of large scale deformation features in the Big Obsidian Flow, Oregon is presented in Chapter IV to highlight deformation mechanisms responsible for the formation large gas cavities within obsidian flows. Results from each project are summarized in Chapter V, where the implications of studies conducted on microscopic, mesoscopic, and macroscopic scales for understanding flow-scale processes are discussed.

Background

Rhyolitic eruptions typically involve an initial phase of explosive Plinian activity followed by quiet effusions of lava (Figure 2). Rhyolitic lavas form steep-sided flows and coulees. Flow fronts range in thickness from approximately 20 meters to greater than 50 meters. Flow surfaces are typically rubbly and consist of angular blocks varying in size from 1-10 meters.

Rhyolitic lavas are texturally and structurally heterogeneous. Fink (1983) noted that chemically homogeneous lavas of rhyolitic obsidian flows generally exhibit three textural types: coarsely vesicular pumice (CVP), finely vesicular pumice (FVP), and obsidian (OBS). These lavas differ primarily in their vesicularities and microcrystallinities, and boundaries between types may be sharp or gradational (Figure 3). CVP has numerous (>50%) large vesicles (diameter > 1 mm), while FVP has both lower vesicularity (<40%)

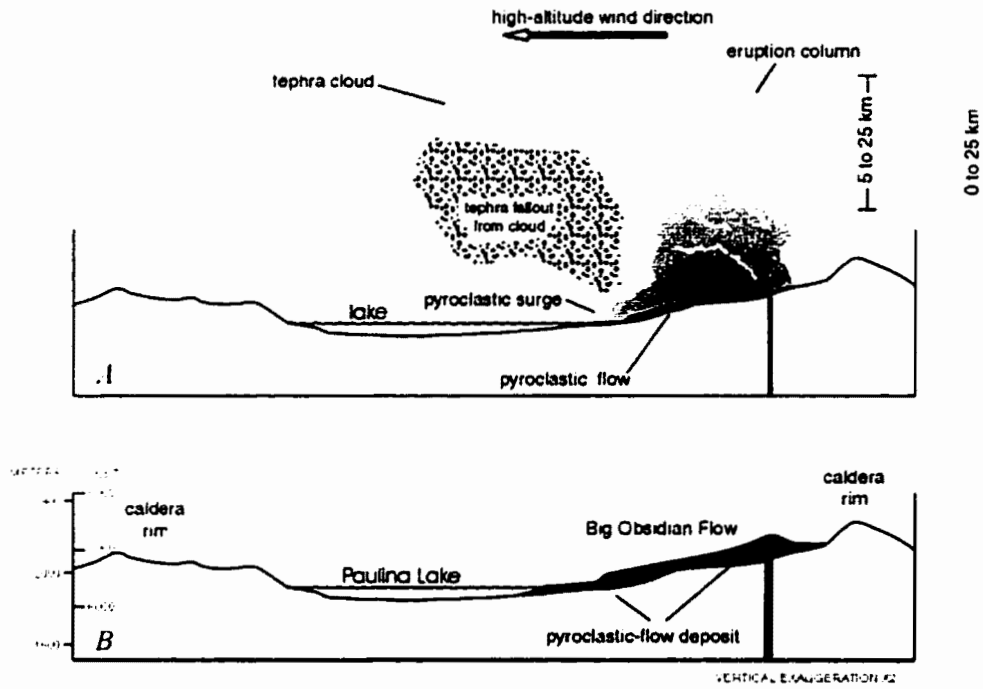


Figure 2. Schematic view of a rhyolitic obsidian eruption (Big Obsidian Flow, OR). Silicic volcanism involves initial explosive activity (A) followed by quiescent effusion of an obsidian dome (B). From Sherrod et al. (1997).

and smaller vesicles (diameter < 1 mm). Obsidian is, by definition, vesicle poor. The three lava types have consistent contact relations throughout flows and occur in a characteristic stratigraphic order (Figure 4).

Two contrasting models have been proposed to explain the transition between initial explosive activity and quiescent effusion of obsidian flows. The first calls on lava extrusion following explosive activity from a magma chamber strongly zoned in volatiles (Eichelberger and Westrich, 1981; Fink, 1983). According to this model, volatile-rich magma concentrated in the roof of a magma chamber causes initial explosive activity. As the eruption continues, the volatile-rich magma is depleted, and the eruptive style changes to quiescent effusion of extensively degassed magma. In this scenario, the textural complexity of flows (i.e., pumiceous zones and apparent textural stratigraphy; Figure 4) develops in response to surface vesiculation and post-emplacement redistribution of volatiles (e.g., Fink and Manley, 1987; Fink et al., 1992). An alternative model (e.g., Eichelberger et al., 1986) proposes that obsidian domes form from eruption of highly inflated and gas-charged magma that undergoes collapse during flow advance to form dense black obsidian. According to this model, the magma reservoir has a homogeneous pre-eruption water content, and the eruptive style is dictated by the rate of upward migration of volatiles through a highly inflated and permeable magmatic foam. The erupted magma is vesicular at the vent, and subsequently collapses under its own weight during flow. In this model, pumiceous zones within obsidian flows are remnant zones of vesiculated lava that did not collapse during flow advance. This permeable foam model requires internal shearing to form obsidian, although structures recording such shear have not been identified.

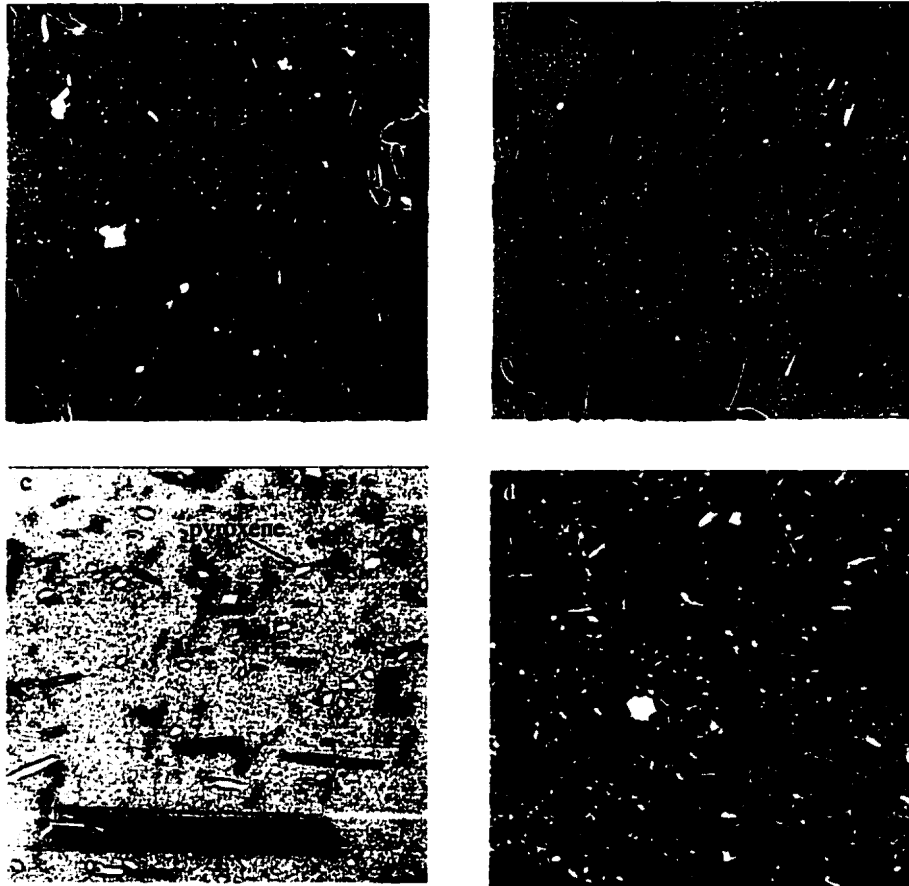


Figure 3. Backscattered electron images (1000X) of (a) CVP, (b) FVP, (c) Obsidian, and (d) vent facies rhyolite. Note differences in groundmass crystallinity. Bright phases are ferromagnesian silicates or oxides while dull grey phases are feldspar. Vent facies rhyolite is nearly totally crystalline. Black spaces are vesicles.

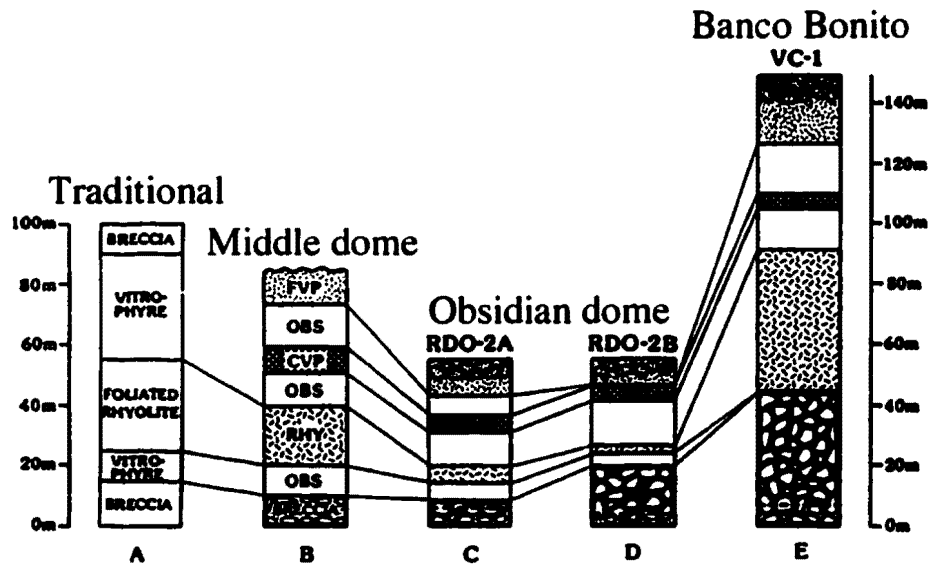


Figure 4. Textural stratigraphy as determined by drill cores through Holocene obsidian flows. From Fink and Manley (1987).

CHAPTER II

MICROLITE SIZE AND ORIENTATION DISTRIBUTION IN OBSIDIAN DOME, CA

Introduction

This chapter presents results from a study of the dynamics of crystallization and flow in the late Holocene Obsidian Dome eruption, eastern CA. Late stage crystallization and flow in the Obsidian Dome system was studied by measuring microlite and microphenocryst size, shape, and orientation in samples collected from the flow front and drill cores through the glassy dike margin and the conduit. Size and shape measurements provide constraints on the (1) crystallization behavior in the system, (2) amount of crystal nucleation and growth during flow, and (3) timescales of crystal growth. Three dimensional microlite orientations are quantified as a means of understanding the eruptive style and strain history of the Obsidian Dome magma. When combined, results from size and orientation analysis provide estimates of eruptive duration and flow rate.

Processes of magmatic flow, degassing, and crystallization can be inferred from textures preserved in volcanic rocks. Microlites act as records of both magmatic flow and chemical evolution and thus, they serve to monitor the physico-chemical properties of the magma as it ascends, deforms, and solidifies. Crystal size and abundance have been used to decipher volcanic processes such as degassing interval, crystal nucleation and growth rates, and degrees of undercooling in basaltic (e.g., Cashman and Marsh, 1988), andesitic (Hammer et al., in press), dacitic (Cashman, 1992; Hammer et al., 1999), and rhyolitic systems (e.g., Sharp et al., 1996). Crystal preferred orientations have been used to infer

strains (e.g., Shelley, 1985; Manga, 1998). In this chapter, I present three-dimensional microlite orientation and size distributions useful for quantifying the kinetics of microlite nucleation and growth, the duration and magnitude of crystallization, the style of magma extrusion, and the relative amount of strain recorded in different volcanic regimes.

Geologic Background

Obsidian Dome was extruded during the most recent series of rhyolitic eruptions in eastern California (Figure 5 ; 550 y.b.p.; Miller, 1985). Owing to its youth, microstructures and textures in lavas from Obsidian Dome are well preserved. This flow is perhaps the most extensively studied obsidian flow on Earth, with abundant data on the petrologic and textural development of the flow made available through the Inyo Domes Research Drilling Project (e.g., Eichelberger et al., 1985). In this chapter I present an analysis of the three-dimensional size and orientation of microlites in samples of obsidian collected from the flow front, dike, and conduit of the system with the goal of deciphering the nature of late stage crystallization and flow in the Obsidian Dome system.

Sample Collection

Oriented samples were collected from five locations along the western flow front of Obsidian Dome (Figure 5). Samples were taken from the uppermost obsidian layer, approximately 10 meters below the surface, where the lava is exposed in laterally-continuous flow banded outcrops approximately 10-20 meters thick. Each sample was oriented by noting the strike and dip of banding, geographic north, and the up direction on the sample. Thin sections were made such that the strike direction of the flow banding is parallel to the long dimension of the slide and the dip direction is perpendicular to the slide.

Additional samples were obtained from the Inyo drilling program, which produced

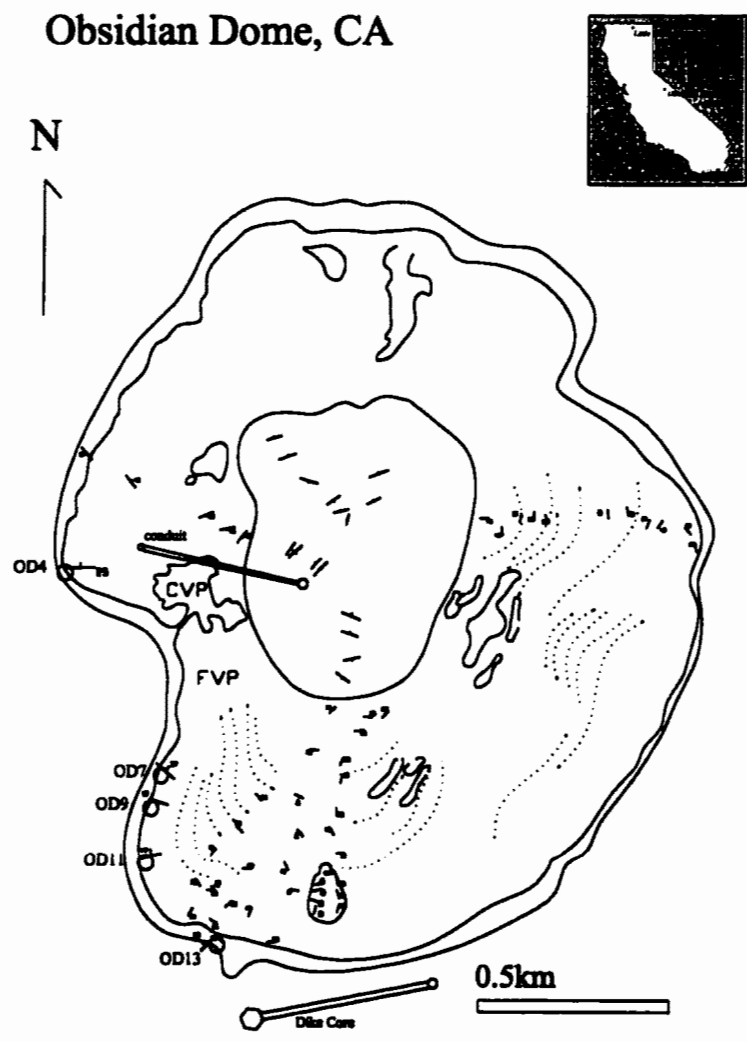


Figure 5. Map of Obsidian Dome, CA, showing the locations of flow front samples and approximate drill core locations. Strike and dip of flow banding is also shown at each sample locality.

nearly continuous core from the dome, conduit, and dike of the obsidian dome complex. Although core samples are not oriented (samples rotated when extracted), they provide an important record of crystallization and textural development in the dike and conduit. Measurements of three-dimensional microlite size and orientation were limited to three glassy samples. One sample was analyzed from the shallow conduit (obtained from drill core RDO-2A), and two samples from the glassy selvage of the western margin of the dike (drill core RDO-3A). Samples from deeper sections of the conduit core were fully crystalline and microlites were difficult to recognize. The vent sample was obtained from an approximate vertical depth of 31.1 feet, and consists of coarsely vesicular pumice. The dike samples were collected from a vertical depth of approximately 650 feet (Westrich et al., 1988). Dike samples come from a thin, 10 cm thick glassy chill margin at the contact of the dike and granitic basement rock. The dike samples have approximately 4% vesicles by volume while the conduit samples contain approximately 20% vesicles.

Measurement Techniques

The following measurements were made to characterize the textural and structural elements of obsidian: 1) three-dimensional microlite length and width, 2) microlite trend and plunge, 3) microlite number density (N_v), 4) microlite number per unit area (N_a), 5) microphenocryst length and width, and 6) microphenocryst N_a .

Three-dimensional microlite length, width, orientation, and number density were determined in doubly polished thin sections made parallel to the strike of microlitic flow bands, and normal to the dip of flow bands. Thin sections were doubly-polished to reduce the amount of scattering that occurs as light propagates into and out of the sample. A series of high magnification (500X) digital photomicrographs were collected from successive 2 μm focal depths within each thin section, by means of an Olympus petrographic microscope fitted with a Panasonic digital camera. NIH Image 1.61 software was used to

grab and store images from thin sections. The resulting series of photomicrographs was imported into the program AutoCAD 14, where the outlines and focal points of each microlite in each section were digitized (Manga, 1998). The vertical position of each digitized slice was shifted relative to the next in the series by a 2 μm interval to produce a stacked array of images which was geometrically consistent with the different focusing planes in the thin section. Next, the series of stacked images was viewed in plan and lines connecting the focal point markers were drawn to create a stick representation of the length of each rod-shaped microlite in the thin section. Sticks representing microlite widths are normal to the length sticks and connect the digitized boundaries of the microlites (Figure 6).

In flow front samples, microlite orientations determined from these reconstructions are represented as trends and plunges of rods and are plotted relative to geographic north. Since the true orientations of the dike and conduit samples are unknown, I documented their microlite orientations using a horizontal angle and a vertical angle plotted with respect to an arbitrary reference frame. The horizontal angle, or azimuth, was denoted as the trend of the microlite and the angle away from horizontal is denoted the plunge of the microlite. The orientation, length, width, and position of each microlite are tabulated automatically by AutoCAD. Microlite volume fraction (N_V) was calculated as the total volume of microlites divided by the total volume analyzed. Individual microlite volumes were calculated from length and width measurements, and assume that crystals are cylindrical.

Microlite and microphenocryst number per area (N_A) and microphenocryst size were also measured in two dimensions from backscattered electron (BSE) images. BSE images were obtained from polished, carbon-coated thin sections (30 μm thick) using a JEOL 6300V Scanning Electron Microscope operating at 15 keV acceleration potential, 3-6 nA beam current, and a 15 μm working distance. Energy Dispersive X-ray spectroscopy (EDX) was utilized for qualitative assessment of mineral compositions. As the average atomic number of pyroxene microlites is considerably higher than crystal-free

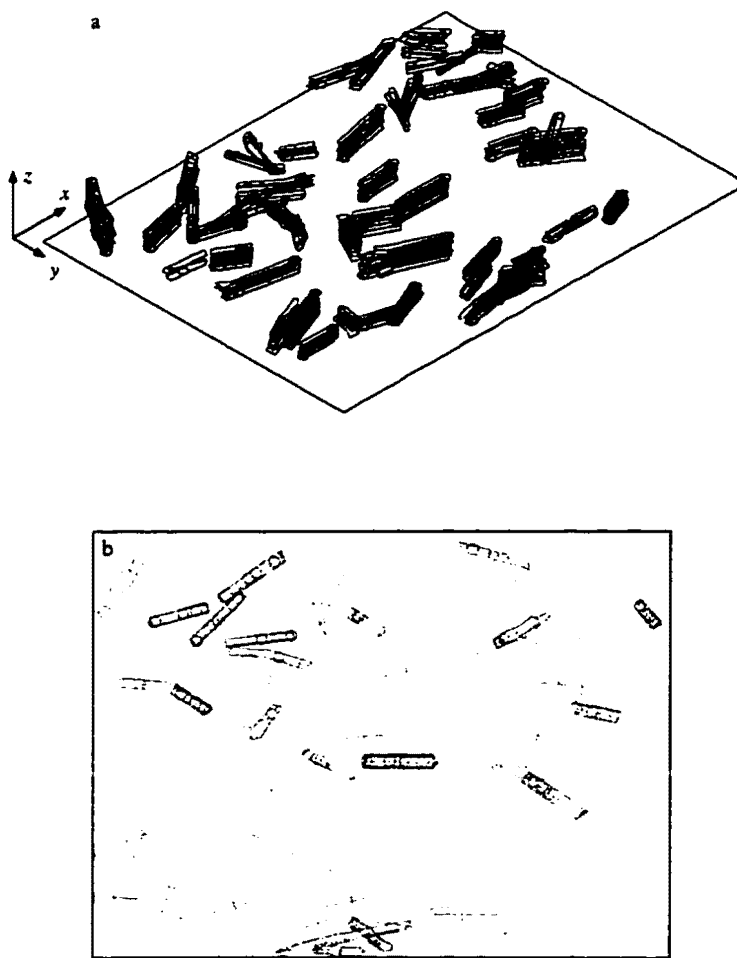


Figure 6. (a) AutoCAD drawing of microlites in obsidian. Sticks represent the lengths of microlites. (b) Plan view of the same sample. Width sticks join opposite prism faces.

glass, pyroxene microlites appear bright relative to the groundmass. Plagioclase has an atomic number similar to the glass and hence exhibits little contrast with the groundmass (Figure 7).

Microlite N_a was determined by dividing the number of crystals in a given image by the groundmass area (the total image area minus area occupied by phenocrysts and vesicles). BSE images (500x) of flow front, dike, and conduit samples were first imported to NIH Image 1.61 where they were thresholded prior to transforming them into binary images. Once images are in binary format, NIH Image 1.61 can be used to count the total number of particles (microlites) per unit area analyzed. Pyroxene and plagioclase counts were done separately, as their gray scale values span a wide range and thresholding one occurs at the expense of resolution of the other. N_a measurements were used as an indication of the relative abundance of pyroxene and feldspar microlites and microphenocrysts in the flow front, dike, and vent samples.

Two dimensional microphenocryst size and N_a were measured in AutoCAD 14, which allows accurate identification of crystal boundaries and a measurement precision of 2-5 pixels ($\sim 0.3 \mu\text{m}$ for 1000X BSE images). The thresholding process invariably results in the loss of resolution, and thus minor errors in crystal size. As with photomicrographs, BSE images were imported into AutoCAD. Images taken at 1000X were used because the scale allowed both the microphenocrysts and microlites to be clearly resolved while maintaining sufficient area coverage for point counts. Area fractions of crystals, vesicles, and glass were determined by manually outlining crystals and bubbles with a polyhedral line tool that was color-coded by phase composition (Figure 8). The number and area of each feature is calculated automatically by the program. The groundmass area was determined by subtracting the cumulative area of vesicles and phenocrysts from the total image area.



Figure 7. Backscattered electron image of conduit sample C-1, showing rod-shaped pyroxene microlites (white) and plagioclase microphenocrysts (dull grey). Scale bar is 25 μm long.



Figure 8. Backscattered electron image of obsidian showing the technique for measuring microphenocrysts. Crystal length and width are determined by drawing lines connecting opposing crystal faces. Scale bar is 20 μm long.

Crystal Size Distributions

Quantitative information on crystal growth rate, nucleation rate, and dominant crystal size can be inferred from three dimensional measurements of crystal length and number density plotted as crystal size distributions (CSD; e.g., Marsh, 1988; 1998). CSD theory (Randolph and Larson, 1971) is based on the assumption that nucleation and growth of crystals occurs continuously while a population balance of crystals is maintained by steady addition and removal of crystals to and from the system. The theory predicts a log-linear distribution of crystal population density (n) with increasing size, where the population density (n) is the number of crystals of a given size class per unit volume. CSD plots showing the natural logarithm of the population density versus crystal length will be a straight line with a slope $-1/Gt$ and intercept n^0 , where G is the crystal growth rate, t is the residence time or crystal growth time, and n^0 is the population density of nucleus-size crystals. The product Gt is equal to the dominant crystal size (L_d). The total number of crystals in the system (N_T) is n^0Gt . Growth rates and growth times can be determined from CSD plots if independent estimates of G or t are known.

Microlite CSDs were constructed from three-dimensional measurements of length and number density. However, 3-D microphenocryst CSDs were not possible to measure because many crystal diameters were larger than the thickness of a standard petrographic thin section (30 μm), and hence 3D AutoCAD techniques were not applicable. Instead, I used apparent length, measured in two dimensions on BSE images.

Because the population distribution (n) function has units of number per size per *volume*, N_a data must be converted to the number of crystals per unit volume (N_v). Conversion of data from N_a to N_v must account for both the interaction between the cut section and the crystal (the so-called cut effect) and the intersection probability (as large crystals are more likely to be intersected than small crystals; Peterson, 1996). Additionally, crystal shape

and size are transformed by sectioning through corners and edges of crystals, and samples with preferred crystal orientations will have apparent number densities that will vary considerably between sections of different orientation (Peterson, 1996).

Microphenocryst measurements made on a per area basis were initially converted to three dimensions using the simple conversion:

$$N_v = N_a/d$$

where N_a is the number per unit area and d is the bin size (Underwood, 1970). Assuming that crystals are uniform in size and randomly oriented, this formulation accounts for the intersection probability by sampling over the range in crystal size, but does not address the cut effect. Problems arising from crystal shape and orientation fabric were addressed by using CSD Corrections (Higgins, 1998), a Windows 95 computer program that converts two dimensional intersection data gathered from thin sections to true three-dimensional crystal size distributions. The program makes corrections for the intersection probability effect and the cut effect if the average three dimensional crystal shape and fabric are known.

The program first builds a solid of the shape indicated by the relative dimensions of the crystal's short, intermediate, and long axes. In two-dimensional sections, these dimensions are inferred by observing the most common cross-sectional shape or aspect ratio. Plagioclase microphenocrysts tend to form stubby to elongate prisms, with typical rectangular cross sections of 2-3:1 aspect ratio. Histograms of aspect ratio may also be used to estimate three-dimensional crystal shape from the modal and highest aspect ratio value (e.g., Higgins, 1994). Aspect ratio histograms will be discussed later. The orientation of the solid is constrained by entering the nature of the fabric (massive, foliated, lineated) and the orientation of the cut section (parallel or normal to fabric). The constructed solid is sectioned by a plane and the length and width of the outline of

intersection are recorded. The distribution of these lengths and widths is the basis for correcting two dimensional size data for the cut section and intersection probability effects, and calculating the CSD. Figure 9 shows a CSD plot for plagioclase microphenocrysts from two flow front samples with (a) and without corrections (b). The corrections result in an overall increase in the total number of crystals in the system ($N_T = n^0 G t$), that is the area under the plot. The slopes and general shapes of distributions remain unchanged.

Results

General Petrographic Characteristics

Microlites

Microlites are typically acicular in habit with aspect ratios (l/w) ranging from 2 to 20. These are true three dimensional aspect ratios as microlites are approximately equant in cross section. In plane polarized light, microlites are colorless to pale green with moderate to high positive relief (Figure 10). Microlites appear most abundant in flow front and conduit samples. Microlites in flow front samples tend to be well oriented except near microphenocrysts, where they are deflected around the larger crystals (Figure 10a, b). Pyroxene microlites are sometimes intergrown with oxide crystals on their ends, giving them a scepter-like appearance (Figure 11). The intergrowth relations shown in Figure 11b suggest that pyroxene crystallized first as a continuous rod and oxide grew later as an overgrowth. Intergrowths of plagioclase and oxide have not been recognized. Crystals have rounded to pyramidal terminations, although swallow tail and jagged ends are common in the dike. While all microlites analyzed share these optical characteristics, reflected light and scanning electron microscopy are required to distinguish the mineral phases present. Pyroxene microlites have both high reflectance and backscatter intensity

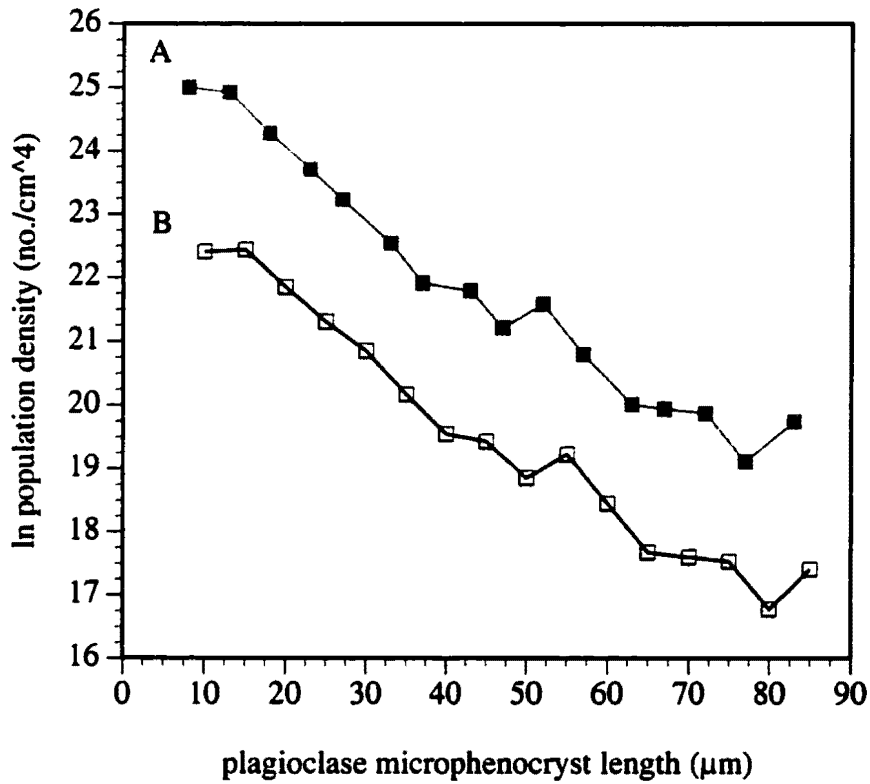


Figure 9. Comparison of crystal size distributions (CSD) for plagioclase microphenocrysts (A) with corrections and (B) without corrections.

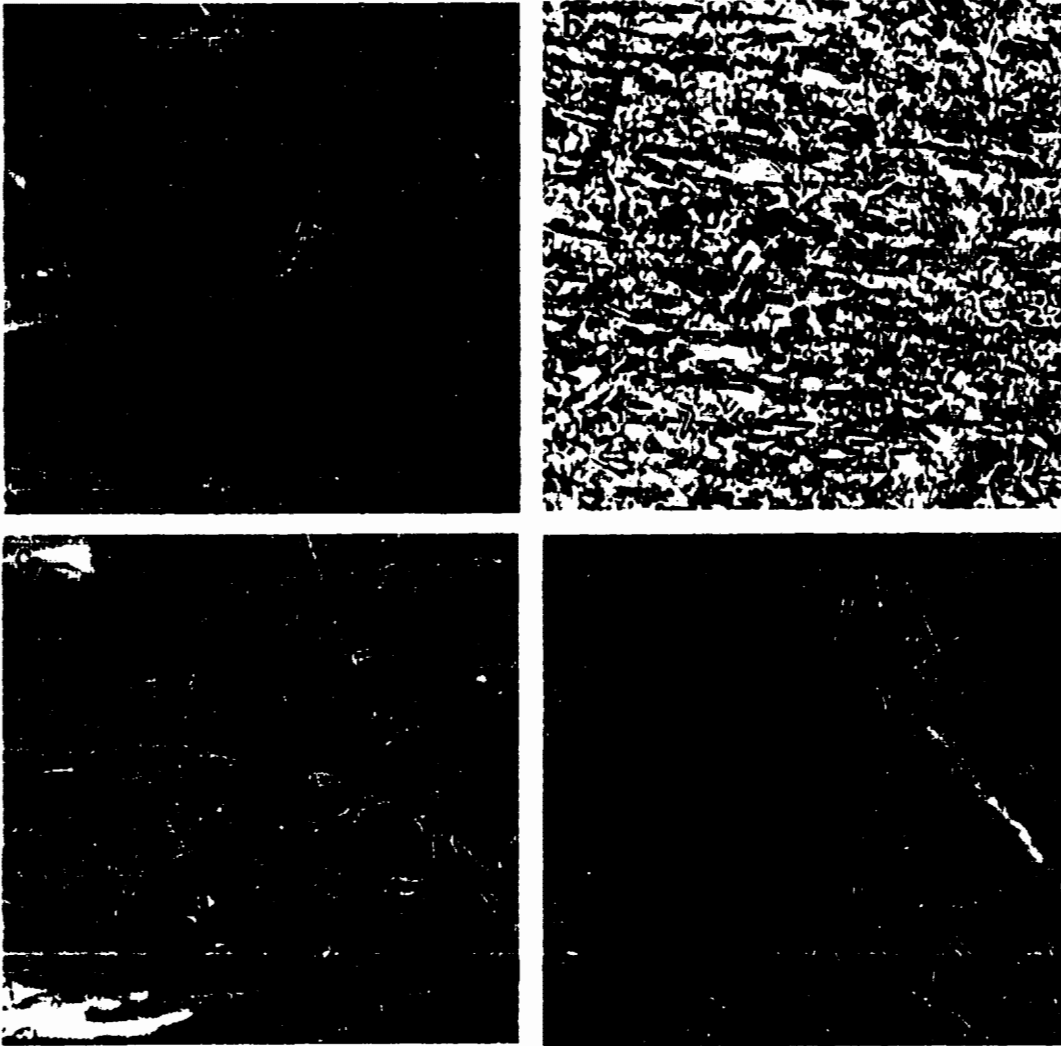


Figure 10. Photomicrographs of obsidian from the (a, b) flow front, (c) dike, and (d) shallow vent. All images are 500X and plane polarized light. Note microlites deflected around microphenocrysts of plagioclase (a).

and have rectangular terminations (Figure 12). In contrast, plagioclase microlites exhibit low to negligible reflectance, have a backscatter intensity similar to groundmass glass, and commonly have swallow tail and jagged terminations (Figure 13). Inferences regarding phase composition based on optical and back scattered electron characteristics were confirmed by EDX analysis of these phases (Figure 14).

Microphenocrysts

Microphenocrysts of plagioclase, pyroxene, and biotite are recognized throughout the Obsidian Dome system (e.g., Vogel et al., 1989). Swanson et al. (1989) define microphenocrysts as "euhedral crystals at least 10 times larger than microlites." An additional constraint that I used to distinguish microphenocrysts from microlites is that microphenocrysts disrupt microlitic flow banding (Figure 15). Plagioclase is the most abundant microphenocryst phase, and typically forms euhedral blocky prisms and fewer tablet-shaped crystals. Hollow-cored crystals and swallow-tailed laths were also recognized. Microphenocrysts probably formed prior to microlites as they are larger and disrupt microlitic flow banding.

Textural Trends

Measurements of microlite and microphenocryst number density, volume fraction, shape, and size were made in order to highlight variations in the conditions of crystallization in the dike, conduit, and flow front of the Obsidian Dome system. Specifically, number density measurements give an estimate of the relative degree of phase supersaturation in the system at the onset of nucleation. Volume fraction yields information about variations in sample crystallinity due to crystal growth or changes in nucleation rate.

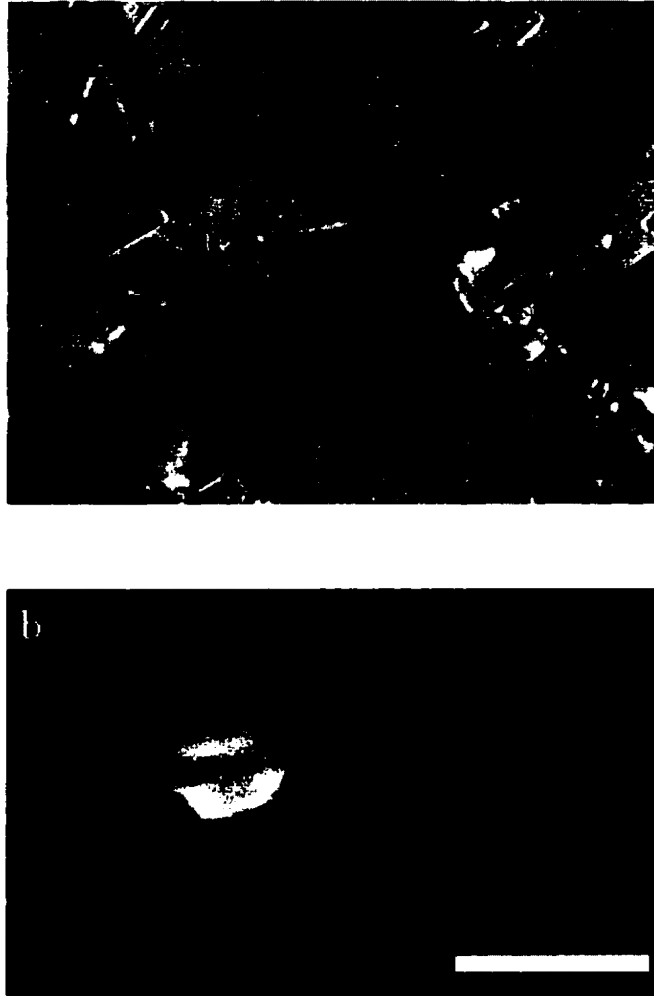


Figure 11. Microlites in (a) plane polarized light and (b) back scattered electron imaging. Black crystal on microlite is an oxide phase. Scale bar in (a) is 10 μm long and 4 μm in (b).



Figure 12. Microlitic obsidian in (A) plane polarized light and (B) reflected light. Both images taken at 500X. Pyroxene microlites show moderate while oxides have high reflectance.

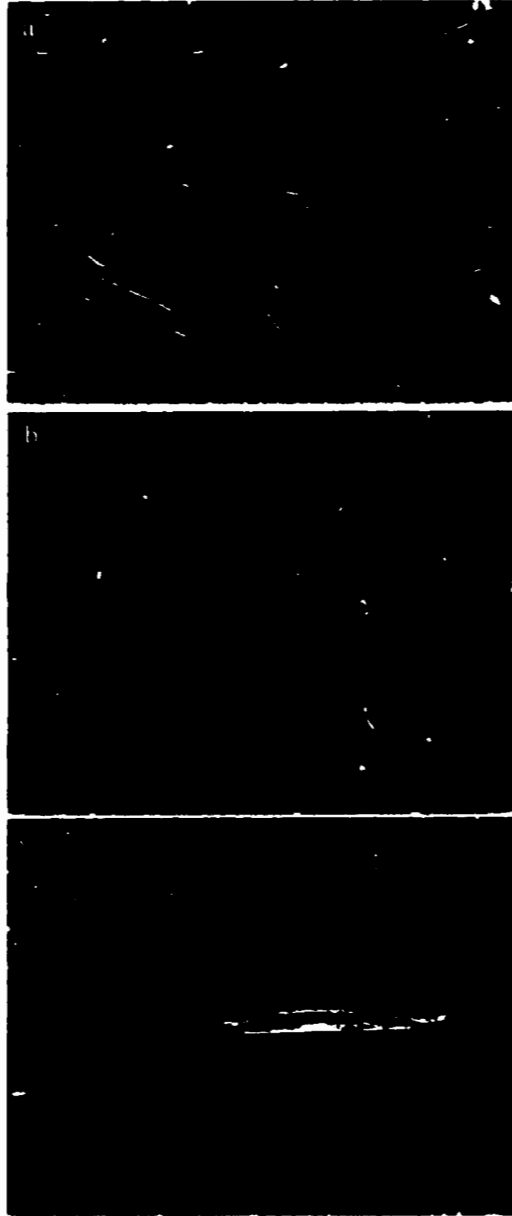


Figure 13. BSE images of obsidian from the (a) flow front, (b) dike, and (c) shallow vent. All images at 1000X magnification. Bright microlites are pyroxene while dull grey microlites are feldspar. Black objects are vesicles.

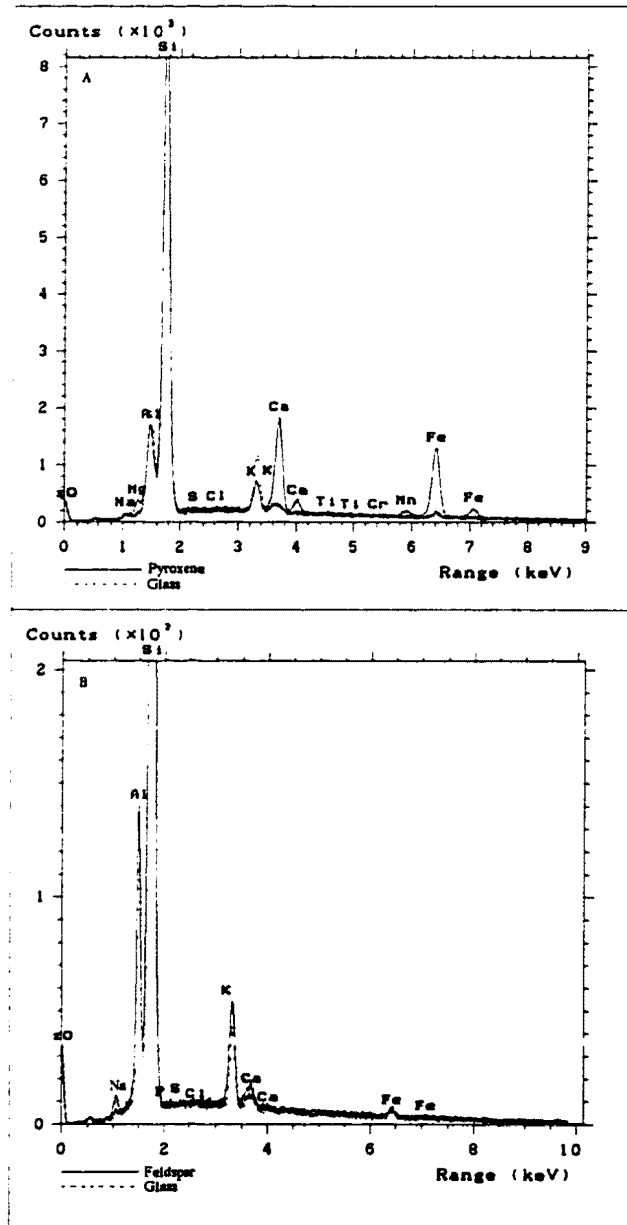


Figure 14. Energy dispersive X-ray spectra for (A) pyroxene and (B) plagioclase microlites from the flow front and dike respectively. Pyroxene analysis indicates an abundance of Fe and Ca relative to glass (dotted line). Plagioclase analysis shows elevated levels of Na, K, Al, and Ca relative to groundmass glass.

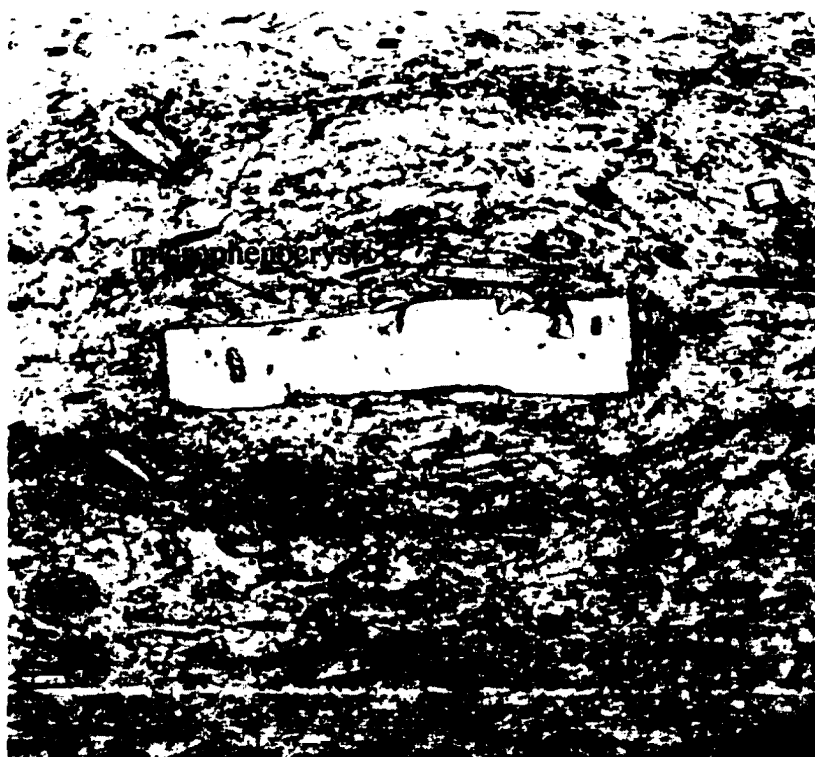


Figure 15. Photomicrograph of obsidian from the dike. Image was taken at 500X in plane polarized light. Note rod-shaped microlites and lath-shaped microphenocrysts. Some microphenocrysts have swallow-tail terminations. Microlites appear to flow around microphenocrysts. Field of view is 0.015 millimeters.

Shape and size variations may reflect the dynamics of crystal growth in the different volcanic regimes within the Obsidian Dome system.

Microlites

Microlite populations in the dike, vent, and flow front show variability in both number density and volume fraction, possibly reflecting changing conditions of crystal nucleation and growth during eruption (Table 1). Two distinct microlite populations are recognized in flow, dike, and conduit samples: a plagioclase-rich assemblage in the dike and a pyroxene-dominant assemblage in the vent and flow front. Analyses of BSE images show that dike samples have comparable numbers of pyroxene and plagioclase microlites while conduit and flow front samples have greater numbers of pyroxene and relatively fewer plagioclase microlites than the dike (Figure 16). Measured pyroxene number densities (N_a) vary from $6.5 \times 10^5 \text{ cm}^{-2}$ in the dike, to $7.9 \times 10^6 \text{ cm}^{-2}$ in the flow front, with an intermediate value of $4.7 \times 10^6 \text{ cm}^{-2}$ in the conduit, thus illustrating a steady increase in pyroxene number during the process of magma ascent and flow away from the vent. In contrast, plagioclase number densities actually decrease with transport, varying from $1.3 \times 10^6 \text{ cm}^{-2}$ in the dike to $1.7 \times 10^4 \text{ cm}^{-2}$ in the flow front, again with intermediate values of $1.5 \times 10^5 \text{ cm}^{-2}$ in the conduit. Microlite N_a in Obsidian Dome samples is comparable to the range of $2 \times 10^5 \text{ cm}^{-2}$ to $9 \times 10^6 \text{ cm}^{-2}$ observed in the rhyolite from Rock Mesa, Oregon (Rogers, 1996).

Total microlite contents from 3-D measurements show approximately constant values of N_v in dike, conduit, and flow front samples, although the conduit sample has the highest overall microlite crystallinity. Figure 17 shows the total number of microlites per volume (N_v) determined from three-dimensional measurements versus the microlite volume fraction (crystallinity). Microlite number density in dike samples ranges from approximately $2\text{-}2.5 \times 10^8 \text{ cm}^{-3}$. Microlite number densities in flow front samples vary

TABLE 1. Measured microlite properties in flow front, dike, and conduit samples.

Sample	No.	Length (μm) ^a	Width (μm)	Aspect Ratio	Number Density (no./cm ³)	Volume Fraction
OD4	127	8.7 (5.1)	2.09	4.2	1.44×10^8	0.020
OD7	402	6.3 (3.4)	1.52	4.1	2.81×10^8	0.014
OD9	486	5.9 (3.7)	1.92	3.1	3.57×10^8	0.028
OD11	381	6.9 (3.6)	1.74	3.9	4.66×10^8	0.032
OD13	182	9.1 (7.2)	1.69	5.4	2.33×10^8	0.028
392-5 ^b	444	7.6 (6.6)	2.2	3.5	2.51×10^8	0.043
392-6 ^b	410	9.1 (7.2)	2.0	4.5	2.08×10^8	0.032
C-1 ^c	389	12.1	2.3	5.4	4.60×10^8	0.090

^a Values in parenthesis are standard deviations of mean length and width.

^b Dike sample

^c Conduit sample

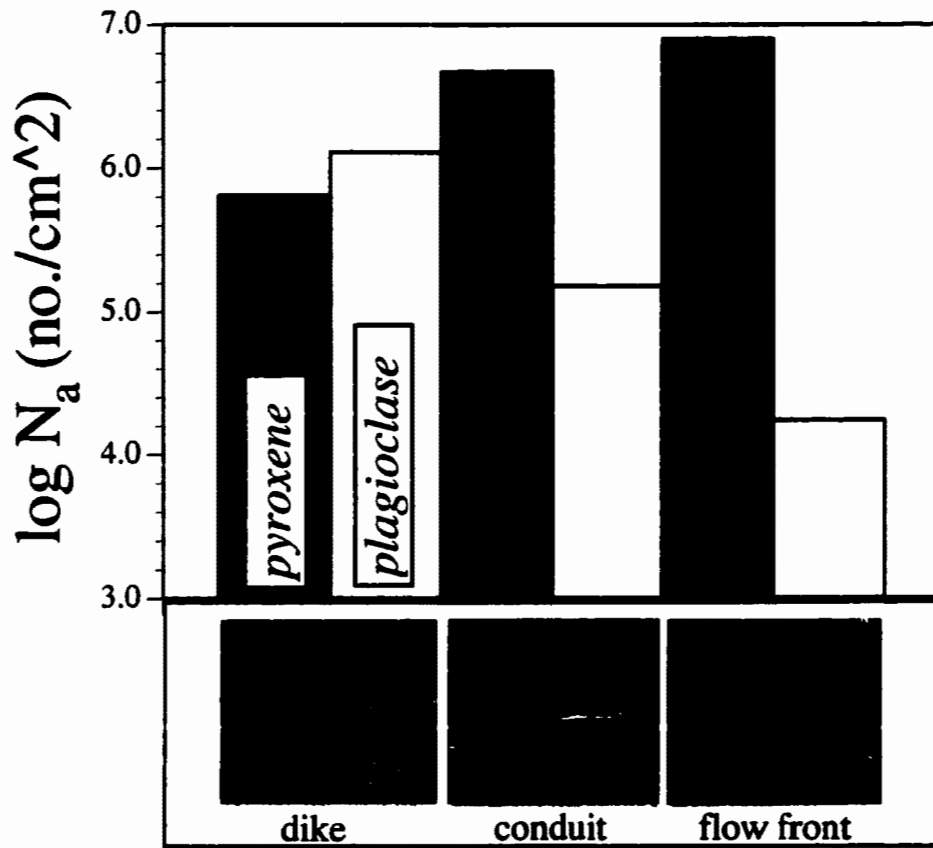


Figure 16. $\log N_a$ for microlites in the dike, conduit, and flow front. BSE images are each at 500X. Note the increase in pyroxene abundance from the dike to the flow front. Plagioclase microlite N_a decreases from the dike to the flow front.

from approximately $1.4 - 4.7 \times 10^8 \text{ cm}^{-3}$. Number density in the conduit sample is comparable to sample OD4 in the flow front ($\sim 4.7 \times 10^8 \text{ cm}^{-3}$). Volume fractions are consistently low in all samples, with average values of 0.038 in the dike, 0.09 in the conduit, and 0.024 in flow front samples. In general, N_V increases as the total number density of microlites increases, indicating that crystallinity increases chiefly by continuous crystal nucleation, rather than nucleation followed by growth.

Microphenocrysts

Measurements of microphenocryst N_a and size were determined for two flow front samples, one dike sample, and one conduit sample in order to quantify textural differences amongst flow front, dike, and conduit microphenocryst populations. In all samples, plagioclase microphenocrysts are larger and more numerous than pyroxene microphenocrysts (Figure 18). Two trends in plagioclase N_a and average length are apparent in Figure 18. First, plagioclase microphenocrysts are larger and more abundant in the flow front than in the dike. Average plagioclase length varies from $21.9 \mu\text{m}$ in the dike to $26.7 \mu\text{m}$ in the flow front, while in a similar manner, N_a increases from $1.1 \times 10^4 \text{ cm}^{-2}$ to $2.4 \times 10^4 \text{ cm}^{-2}$. This trend reflects crystallization characterized by both nucleation and growth on existing crystals (e.g., Hammer et al., 1999). The increase in plagioclase microphenocryst size from $21.9 \mu\text{m}$ in the dike to $27.5 \mu\text{m}$ in the conduit defines a second, growth dominated trend. The slight decrease in plagioclase N_a between the dike and conduit samples may signal a decrease in plagioclase nucleation over time (Table 2). Plagioclase microphenocryst N_a ($2.4 \times 10^4 \text{ cm}^{-2}$) is comparable to plagioclase microlite N_a ($2.0 \times 10^4 \text{ cm}^{-2}$) in flow front samples, however plagioclase microphenocrysts are less abundant than plagioclase microlites in the conduit and dike. Pyroxene microphenocrysts are absent in the dike and are more abundant and larger in the flow front than in the conduit.

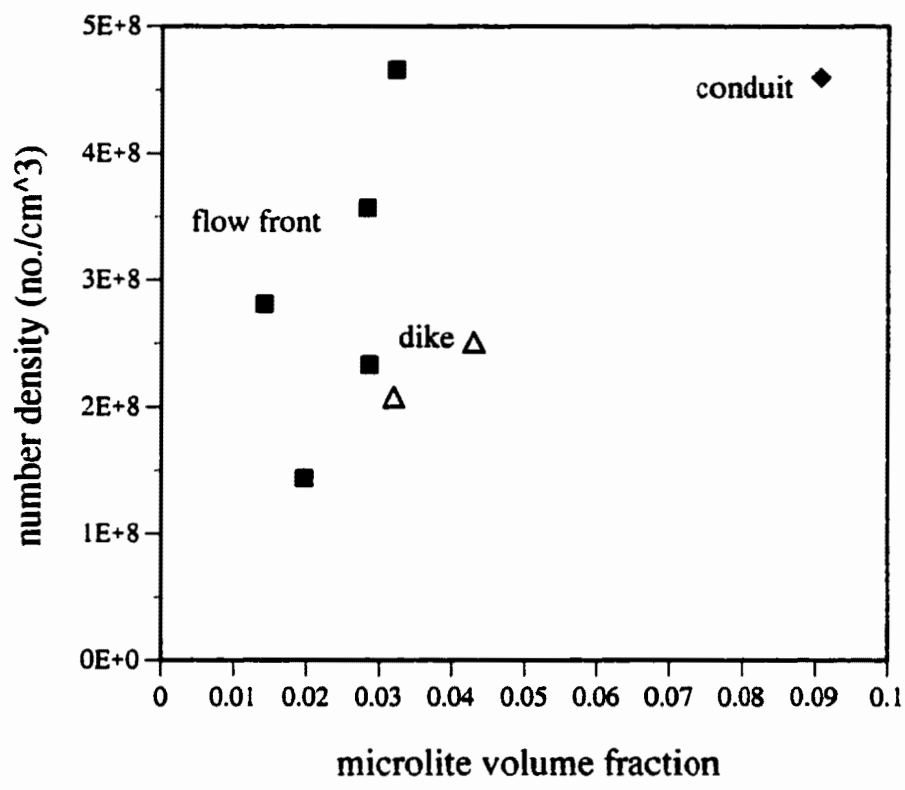


Figure 17. Microlite number density versus volume fraction determined from three-dimensional measurements.

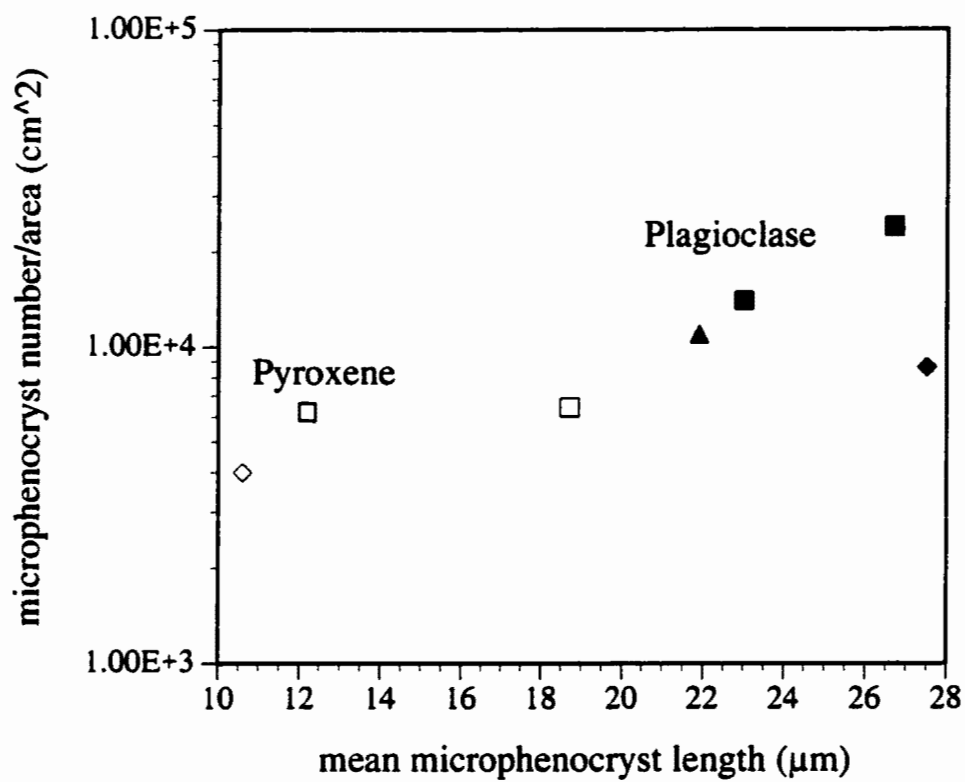


Figure 18. Mean microphenocryst number/area versus length for plagioclase (solid symbols) and pyroxene (open symbols). Flow front (■), dike (▲), and vent (◆).

Crystal Shape and Size

Shape

Crystallization experiments in silicic systems (e.g., Lofgren, 1980) have shown that crystal shape is partly determined by the degree of undercooling, or the difference in temperature between a mineral's liquidus and when it actually begins to crystallize (e.g., Lofgren, 1971; 1974; Swanson, 1977). Undercoolings induced either by rapid quenching of magma by conductive heat transfer or by volatile exsolution will lead to a variety of crystal morphologies, including acicular, tablet, and equant prismatic forms. Microlite and microphenocryst shapes were measured in three and two dimensions respectively, in order to determine patterns of crystal shape change with growth and to better understand how variation of crystal shape between microlites and microphenocrysts might reflect changes in the degree of undercooling. Plagioclase shape differs between microlite and microphenocryst populations. Microlites are typically acicular in three dimensions while microphenocrysts form stubby prismatic and tablet-shaped cross sections. Changes in crystal shape can be quantified by measuring the crystal aspect (l:w) ratios. Figure 19 shows histograms of aspect ratios for plagioclase microlites and microphenocrysts in the dike and flow front. The microlite histogram shows true (three-dimensional) aspect ratios while the microphenocryst distribution represents two dimensional, or apparent aspect ratios. Plagioclase microlites have a mean true aspect ratio (shown by arrows) of 3.85 and a maximum of 16. This distribution shows that most plagioclase microlites are thin rods with some very elongated crystals. Microphenocrysts have an average apparent aspect ratio of 2.2 with a maximum of 6. Both histograms are skewed towards large aspect ratio and have similar modes at approximately 2.

TABLE 2. Measured Microphenocryst Properties

Sample	Phase	No.	Area Analyzed (cm ²)	Number/Area (cm ⁻²)	Length (μm) ^a	Width (μm)
OD4	plagioclase	133	5.6x10 ⁻³	2.4x10 ⁴	26.7(19.3)	12.4(7.8)
	pyroxene	36	5.6x10 ⁻³	6.4x10 ³	18.7(13.1)	6.1(3.3)
OD9	plagioclase	106	7.4x10 ⁻³	1.4x10 ⁴	23.0(15.3)	10.6(5.3)
	pyroxene	46	7.4x10 ⁻³	6.2x10 ³	12.2(9.6)	5.2(5.2)
Dike	plagioclase	38	3.5x10 ⁻³	1.1x10 ⁴	21.9(15.5)	8.0(5.3)
Conduit	plagioclase	30	3.5x10 ⁻³	8.6x10 ³	27.5(16.7)	15.2(10.8)
	pyroxene	14	3.5x10 ⁻³	4.0x10 ³	10.6(7.4)	5.4(2.0)

^a Values in parentheses are standard deviations of mean length and width.

Higgins (1994) showed that the modal aspect ratio for a two dimensional distribution can be used to determine the average ratio of the intermediate to short axes in a crystal population and that the maximum aspect ratio in the histogram represents the true ratio of long to intermediate axes. Using this formulation, plagioclase microphenocrysts have an intermediate to short axis ratio of approximately 2 and a long to intermediate axis ratio of 6, yielding an overall shape of 1:2:6. According to this formulation, the data indicate a mean three dimensional shape that is less elongate than that of plagioclase microlites. Shape assessment of plagioclase microlites and microphenocrysts thus indicates a transition in crystal morphology from long thin prisms to blocky, more equant prisms.

Pyroxene microlites have an average aspect ratio of 4.3, a modal aspect ratio of 3.0, and a maximum elongation of 20:1 (Figure 20). Microphenocrysts have an average apparent aspect ratio of 3.4 and a mode at 2. The largest aspect ratio measured in microphenocryst assemblages is 9, indicating an average shape of 1:2:9. These observations suggest that similar trends in shape change occur in both plagioclase and long thin prismatic crystals. With continued growth, plagioclase microlites become less elongate and less equant, forming blocky prismatic microphenocrysts. Similarly, pyroxene microlites evolve towards less elongate forms with growth.

Shape analysis for both plagioclase and pyroxene indicates a crystal morphologic transition from microlites with elongate prismatic habits to microphenocrysts with blocky prismatic shapes. The shape transition for plagioclase reflects a change in the surface area to volume ratio (SA/vol.) from $4.5 \mu\text{m}^{-1}$ to $3.3 \mu\text{m}^{-1}$, a decrease of approximately 26%. Similarly, the pyroxene transition from elongate to blocky prism represents a SA/vol. decrease from $4.5 \mu\text{m}^{-1}$ to $3.2 \mu\text{m}^{-1}$, or 29%. Hammer et al., (1999) documented that SA/vol. of microlites in the Mt. Pinatubo dacite decreased approximately 70% as shape changed from tablet to prismatic. Such changes in SA/vol were correlated to the a shift from nucleation- to growth dominated crystallization.

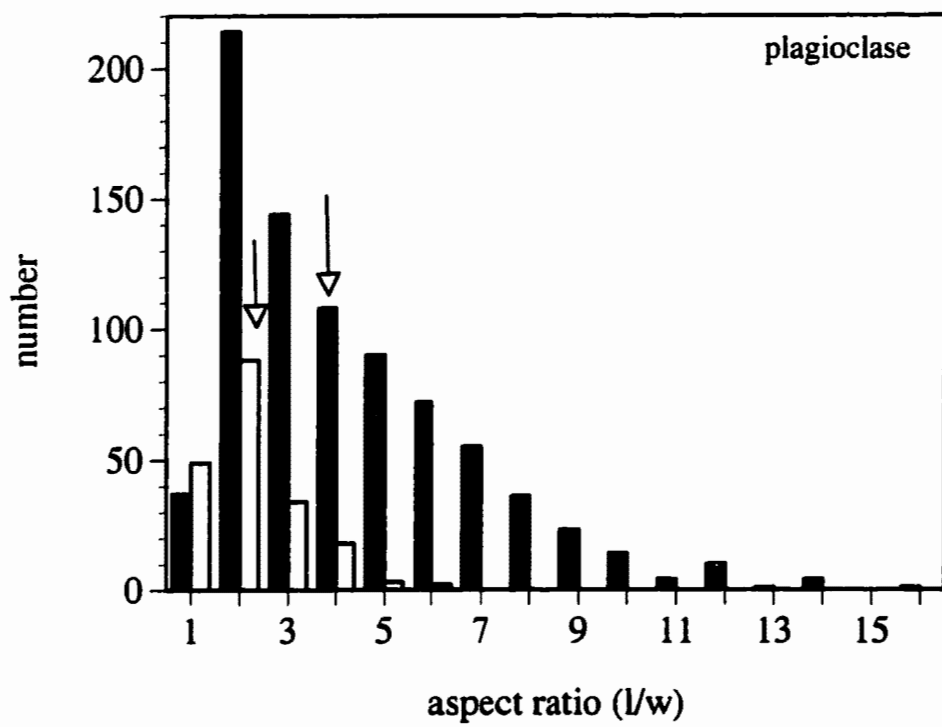


Figure 19. Aspect ratio histogram for plagioclase microphenocrysts in the dike (light shaded bars) and the flow front (dark bars). Arrows shown mean aspect ratio.

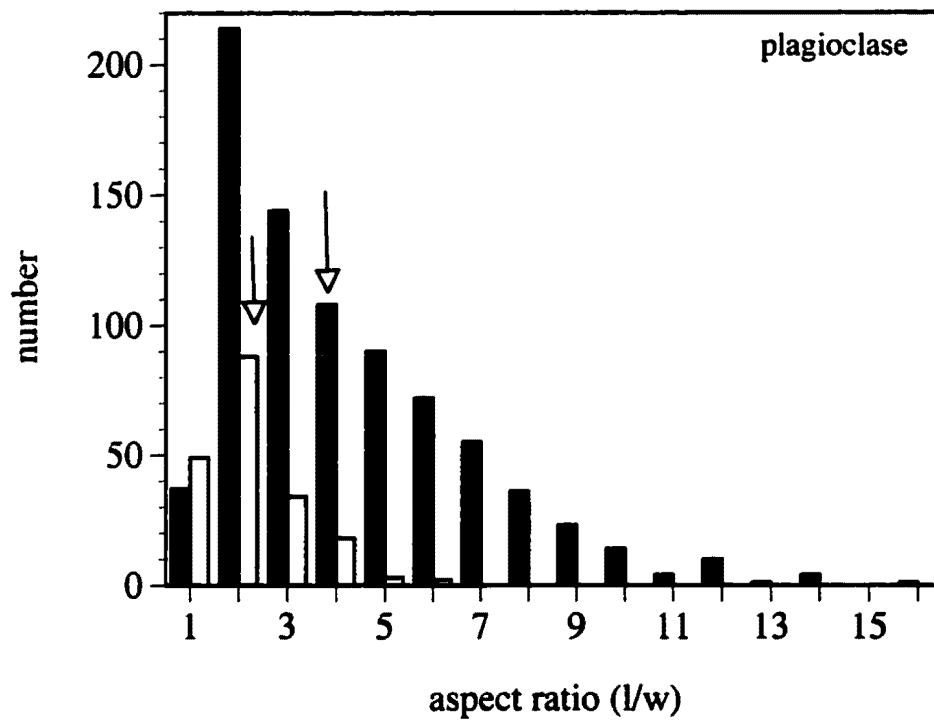


Figure 20. Aspect ratio histogram for pyroxene microphenocrysts in the dike (light shaded bars) and the flow front (dark bars). Arrows show mean aspect ratio.

Microlite Size

Three dimensional measurements of microlite size were determined for all samples from the flow front, dike, and conduit. Systematic changes in microlite size may represent multiple microlite populations or intervals of microlite growth during and after eruption. Sharp et al. (1996) distinguish three microlite size populations in obsidian from the Ben Lomond flow, New Zealand: nanolites ($<0.6 \mu\text{m}$ wide), microlites ($>0.6 \mu\text{m}$ wide), and microphenocrysts ($>1.2 \mu\text{m}$ wide). Here I have measured microlites and microphenocrysts of the size range observable with a petrographic microscope ($>1 \mu\text{m}$ in width), and hence the size distributions are a subset of all crystals in the system. Owing to the limits in resolution, crystals smaller than $\sim 1 \mu\text{m}$ in width are not included in this study.

Histograms of microlite length and width for the flow front, dike margin, and shallow conduit samples are shown in Figure 21. Data for the five flow front samples are combined. Measurements made on two separate dike samples are combined because they are in close proximity to each other and come from a relatively small portion of the 10 cm-thick glassy margin. All microlite histograms are unimodal. Histograms of flow front and dike microlite lengths are skewed towards large sizes, while microlite sizes in the conduit are more normally distributed. Microlite width distributions are symmetrical in all samples (insets Figure 21) and indicate similar modes of approximately $2 \mu\text{m}$. Individual size frequency plots for flow front samples are shown at each sample location in Figure 22. Sample OD13 has the highest mean length of flow front samples. No systematic variations in microlite length are recognized in flow front samples, and 4 of the 5 samples have similar size distributions. In contrast, Sample OD13 has a nearly symmetrical distribution and has the largest mean length of the flow front samples (see Table 1).

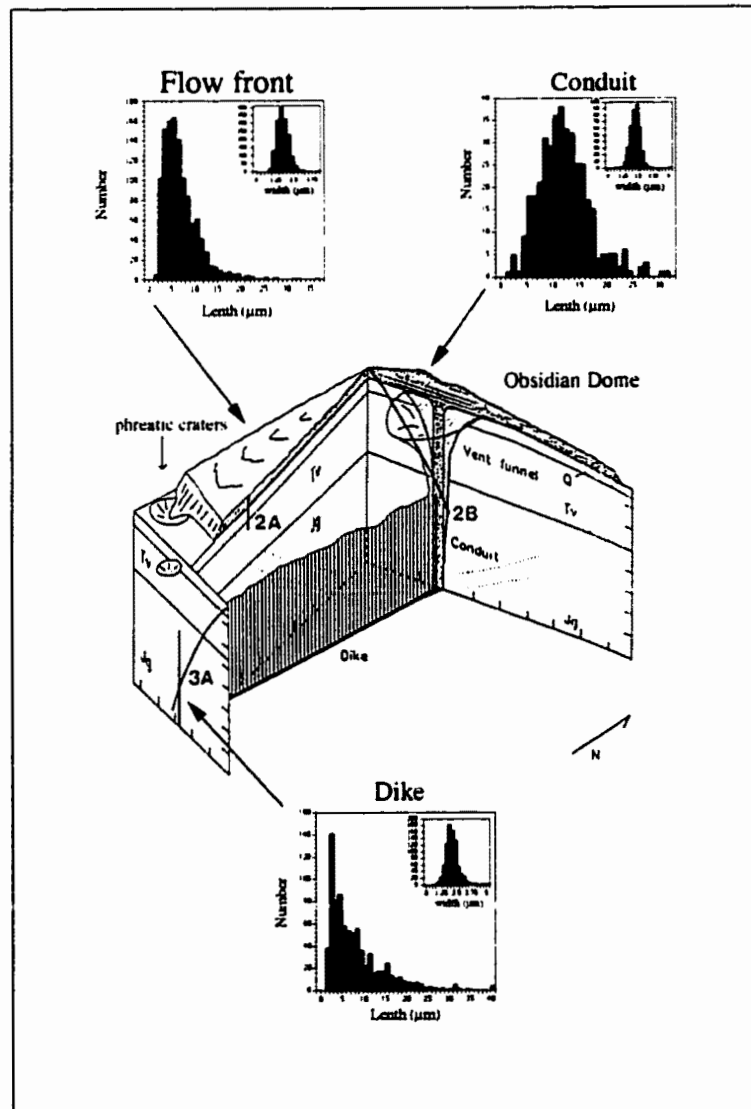


Figure 21. Microlite size histograms for the flow front, dike, and shallow vent samples. Inset are histograms of microlite width. Size in microns.

Plagioclase Microphenocryst Size

Apparent plagioclase microphenocryst length and width histograms are shown for dike, conduit, and flow front samples in Figure 23. The shape of microphenocryst length distributions are similar in dike, conduit, and flow front samples to that of microlites, with a tail extending to large sizes. Modal length for flow front and dike samples falls between 10 and 15 μm while the mode of the conduit sample is 20 μm . The overall abundance of microphenocrysts in the flow front is greater than in the dike and conduit. The mean length of plagioclase varies from 21.9 μm in the dike, to 27.5 μm in the conduit, with an intermediate value of 24.9 μm in the flow front. Width distributions are more symmetrical, although minor skewness to larger widths is apparent. The maximum microphenocryst length measured is 110 μm , with a maximum width of 40 μm . Pyroxene microphenocrysts were not abundant enough for statistical analysis and presentation, however their mean dimensions, along with those of plagioclase, are presented in Table 2. Pyroxene microphenocrysts in both conduit and flow front samples are somewhat smaller than plagioclase (15.4 μm and 10.6 μm in average length respectively) and increase in size from the conduit to the flow front.

Crystal Size Distributions

Crystal size distributions (CSDs) may serve as detailed records of crystal nucleation and growth in various parts of the Obsidian Dome system. CSDs may also yield information on the duration of crystal growth (t) if independent estimates of crystal growth rates are available. In this section I present CSDs for microlites from the dike, conduit, and flow front in addition to plagioclase microphenocryst CSDs for the dike and flow front as a means of (1) better quantifying crystal size, (2) assessing variations in crystal growth amongst dike, conduit, and flow front samples, and (3) estimating timescales of

Obsidian Dome, CA

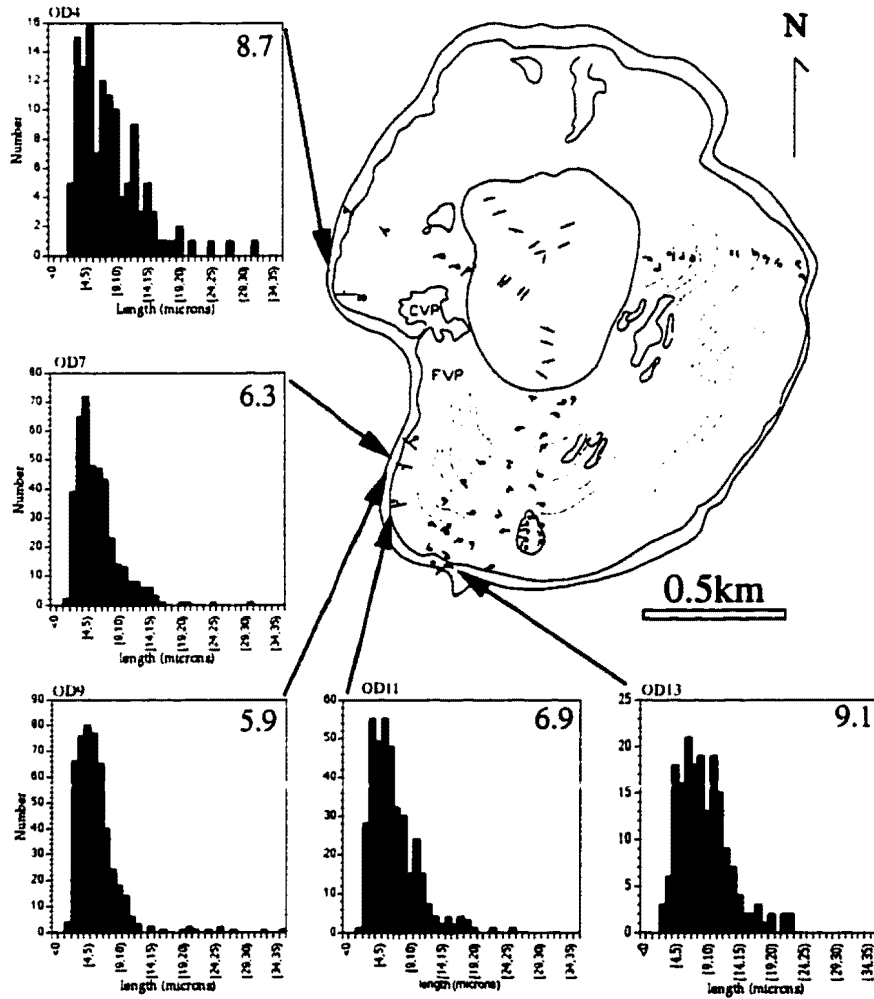


Figure 22. Individual flow front microlite length distributions. Mean length is shown in upper right corner of each histogram.

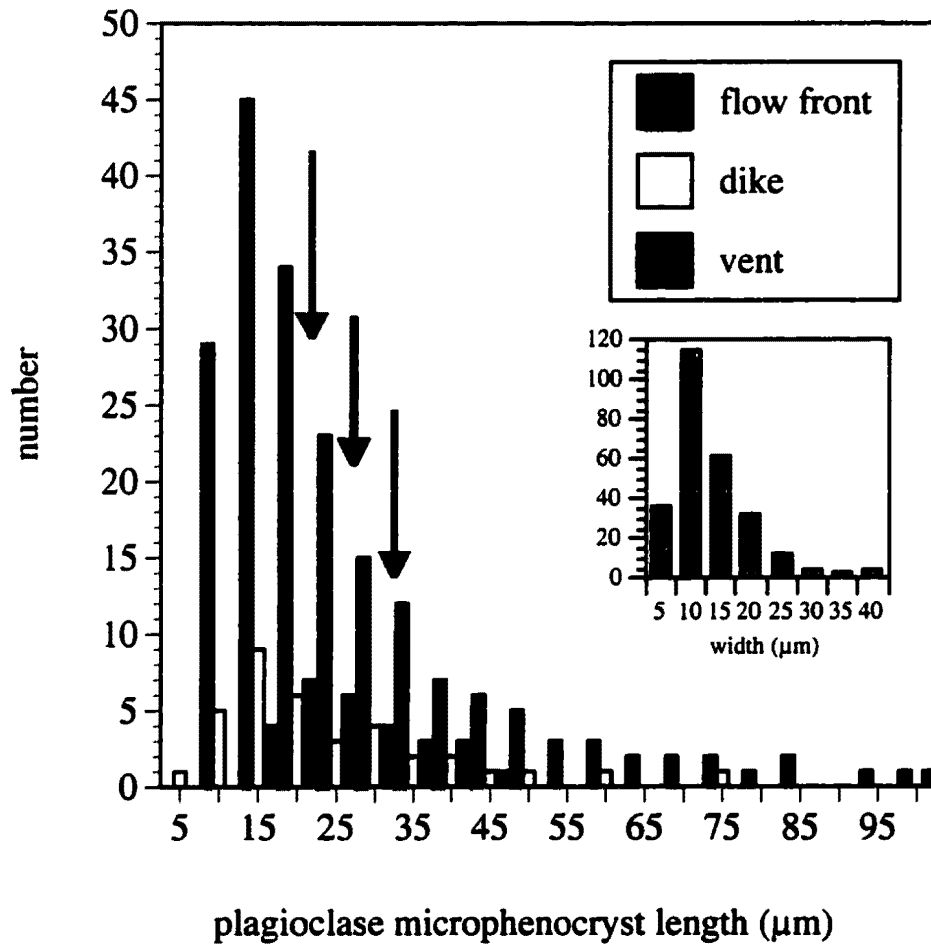


Figure 23. Plagioclase microphenocryst length and width (inset) histograms. Note apparent skewness in length of flow front, dike, and conduit samples. Conduit samples have a larger modal length than flow front and dike samples, which are approximately equal.

crystallization, which may provide a measure of eruption duration. I used true length as a plotting parameter in all microlite CSDs and apparent length for microphenocryst CSDs.

Microlites

The crystal size distribution for microlites in flow front sample (OD9) is shown in Figure 24. The CSD shows a distinct break in slope at approximately 17 μm , a feature that might result from either a lack of data for the larger crystal size classes, or from the presence of two distinct populations of crystals (e.g., Cashman, 1988), for example microphenocryst and microlite populations. Population densities for the smallest measured microlite size classes (2-5 μm) lie below the linear trend defined by the larger size classes. We attribute this downtrend to both limits in the resolving power of the petrographic microscope ($\sim 1 \mu\text{m}$) and to growth of crystals in the smallest size classes. Growth of newly formed microlites will diminish the number of small crystals in the system. Because of these difficulties, the smallest five size classes of crystals were not included in linear least squares fits to the data and in calculating the slopes of plots.

Individual flow front CSDs are shown separately in Figure 25. CSD plots show only the linear segments of data and do not include points falling below the main trend at small sizes. Slopes of lines fit to data in the 3-15 micron size class range from -0.40 to -0.17 cm^{-1} , which corresponds to a range in the dominant microlite size of 2.5 to 5.9 μm . Intercepts of regression lines ($=\ln n^0$) vary from 26.6 to 30.2. The corresponding range in the total number of crystals (N_T), is $2.1 \times 10^8 \text{ cm}^{-3}$ to $3.3 \times 10^9 \text{ cm}^{-3}$. The upper value of L_d of 5.9 μm , is comparable to the modal size as indicated by the length histogram (6-7 μm ; Figure 21). The CSD for sample OD13, fit to a narrow range of linear data from 10-18 μm , may not be entirely meaningful due to the omission of several small ($< 10 \mu\text{m}$) and large ($> 18 \mu\text{m}$) crystals from the CSD.

TABLE 3. CSD parameters for Obsidian dome microlites.

Sample ^a	Slope (cm ⁻¹)	ln n ⁰	Dominant Size (μm)	N _T (no./cm ³)
OD4	-0.17	26.6	5.9	2.1x10 ⁸
OD7	-0.27	27.9	3.7	4.8x10 ⁸
OD9	-0.40	29.1	2.5	1.1x10 ⁹
OD11	-0.32	29.0	3.1	1.2x10 ⁹
OD13	-0.40	30.3	2.5	3.3x10 ⁹
Dike	-0.15	26.7	6.7	2.7x10 ⁸
Conduit	-0.12	28.1	8.3	1.4x10 ⁹

^a OD samples collected from the flow front. Flow front CSDs have a mean slope of -0.31 (s.d.=0.1) and ln n⁰=28.6 (s.d.=1.4).

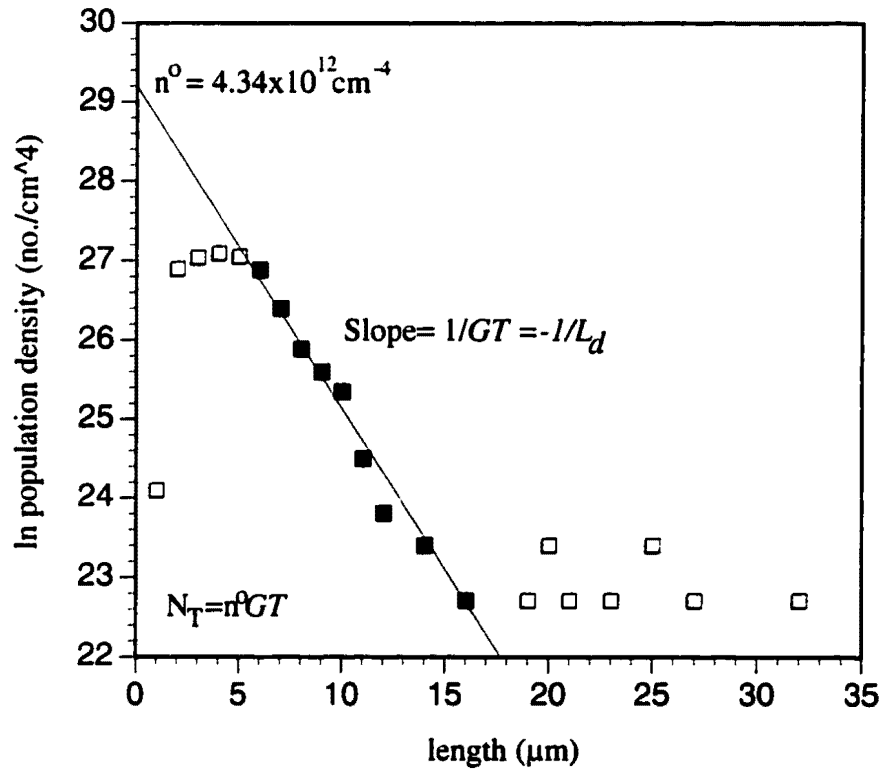


Figure 24. CSD for microlites in flow front sample OD9. Note break in slope at 17 μm may suggest a separate population of crystals. Linear least squares regression is fit to data represented by solid squares.

Sample OD4 has the smallest CSD slope (-0.17 cm^{-1}) and intercept (26.6), while samples OD7, OD9, and OD11 show steadily increasing slopes and intercepts. These flow front CSDs pivot from steep-sloped with high intercept in the southernmost flow samples (OD9 and OD11) to shallow-sloped with low intercept in the northern flow front (OD4). This pattern may reflect growth of microlites on the surface, as the slope of CSDs is inversely proportional to the dominant size.

A combined CSD for all flow front samples is shown in Figure 26. In this plot, the break in slope disappears, suggesting that its appearance in the single flow front sample CSD (cf. Figure 24) is a consequence of limited data in larger crystal size classes. The slope of the best fit regression is 0.26 cm^{-1} , which corresponds to a dominant size of $3.8 \mu\text{m}$. The intercept of the regression line is 27.8. These data indicate a total number density (N_T) of $4.5 \times 10^8 \text{ cm}^{-3}$, which is comparable to the average measured number density ($3.0 \times 10^8 \text{ cm}^{-3}$). The slight discrepancy between dominant size and modal size can be explained by the omission of small size class (lengths $< 5 \mu\text{m}$) from calculations of slope.

The CSD for dike samples is linear with a calculated least-squares slope of -0.16 cm^{-1} and an intercept of 26.9 (Figure 27). The dominant crystal size is $6.25 \mu\text{m}$ and $N_T = 3.0 \times 10^8 \text{ cm}^{-3}$. The dike CSD also shows a downturn at small size classes, again probably due to the lack in spatial resolution of the petrographic microscope. In contrast to the forms of flow front and dike CSDs, the conduit CSD is bell-shaped and indicates maximum population densities at intermediate ($\sim 10\text{-}12 \mu\text{m}$) crystal sizes (Figure 28). A linear least squares regression to the linear segment of this data ($\sim 10\text{-}17 \mu\text{m}$) yields a slope of -0.13 cm^{-1} ($L_d = 7.7 \mu\text{m}$) and an intercept of 28.2. The total number of crystals in the system is $1.4 \times 10^9 \text{ cm}^{-3}$. Table 3 lists slopes and intercepts, dominant crystal size, and N_T evaluated from microlite CSDs.

Microlite CSDs are roughly linear for the dike and flow front samples, and bell-shaped for the conduit sample. Different slope values for linear CSD segments in the dike

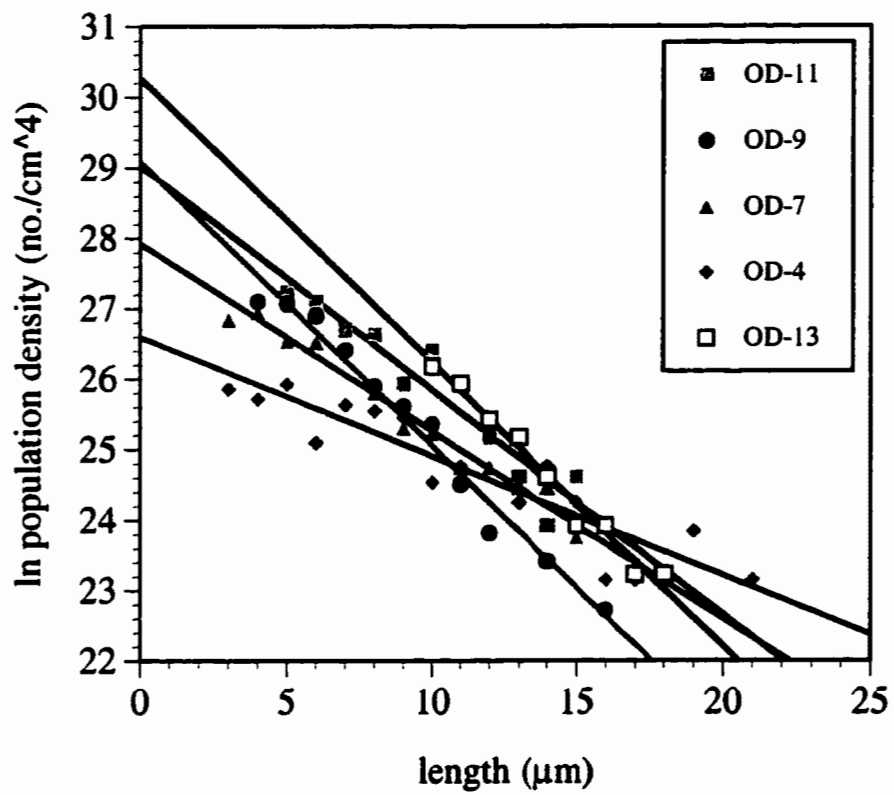


Figure 25. Individual microlite CSDs for flow front samples.

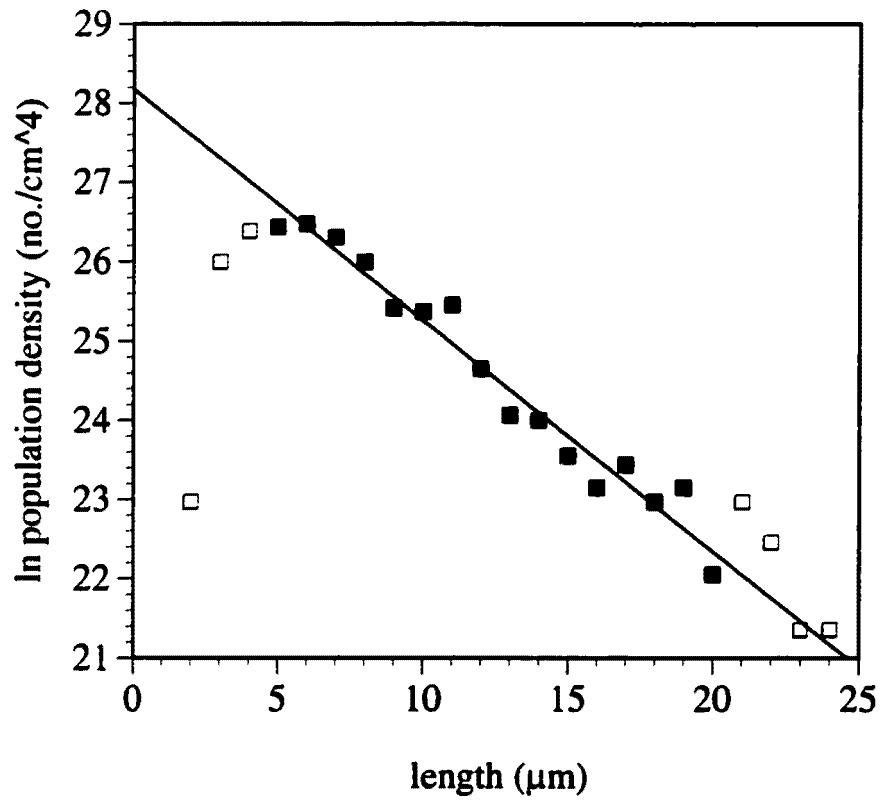


Figure 26. CSD for microlites in all flow front samples.

and flow probably reflect the two distinct populations of crystals recognized in these samples in microscopic analysis. The bell-shaped CSD for the conduit sample signals the loss of crystals in size classes smaller than 10 μm . The downturn of the CSD at small size classes may indicate that some larger crystals grew at the expense of small crystals in the conduit.

Microphenocrysts

Crystal size distributions were also measured for plagioclase microphenocrysts in two flow front samples and two dike samples. I used apparent microphenocryst length, measured as the longest distance between opposing prism faces, as a plotting parameter. CSDs for pyroxene were not determined because of the relatively small number of pyroxene microphenocrysts in all samples.

A CSD of plagioclase microphenocrysts in flow front samples is approximately linear from 15-40 μm , and shows a distinct break in slope at lengths greater than 40 μm (Figure 29). A best-fit line over all sizes yields a slope of -0.079 cm^{-1} and an intercept of 25.8. This geometry corresponds to a dominant crystal size of 11.1 μm and an N_T of $1.8 \times 10^8 \text{ cm}^{-3}$. The dominant crystal size calculated from the CSD slope is comparable to the modal length determined from the histogram ($\sim 12.5 \mu\text{m}$; Figure 23). The segment of the curve from 15 to 40 μm yields a slope of -0.12 cm^{-1} and intercept at 26.4. This geometry corresponds to a dominant crystal size of 8.3 μm and an N_T of $2.4 \times 10^8 \text{ cm}^{-3}$. The segment of data at sizes greater than 40 μm has a slope of -0.062 cm^{-1} and an intercept of 24.3 cm^{-4} , which corresponds to a dominant size of 16.1 μm and an N_T of $5.8 \times 10^7 \text{ cm}^{-3}$ (Figure 30).

The CSD for microphenocrysts in the dike is shown in Figure 31. The plot exhibits the slight downturn in population density at sizes less than 10 μm . Above 10 μm in size,

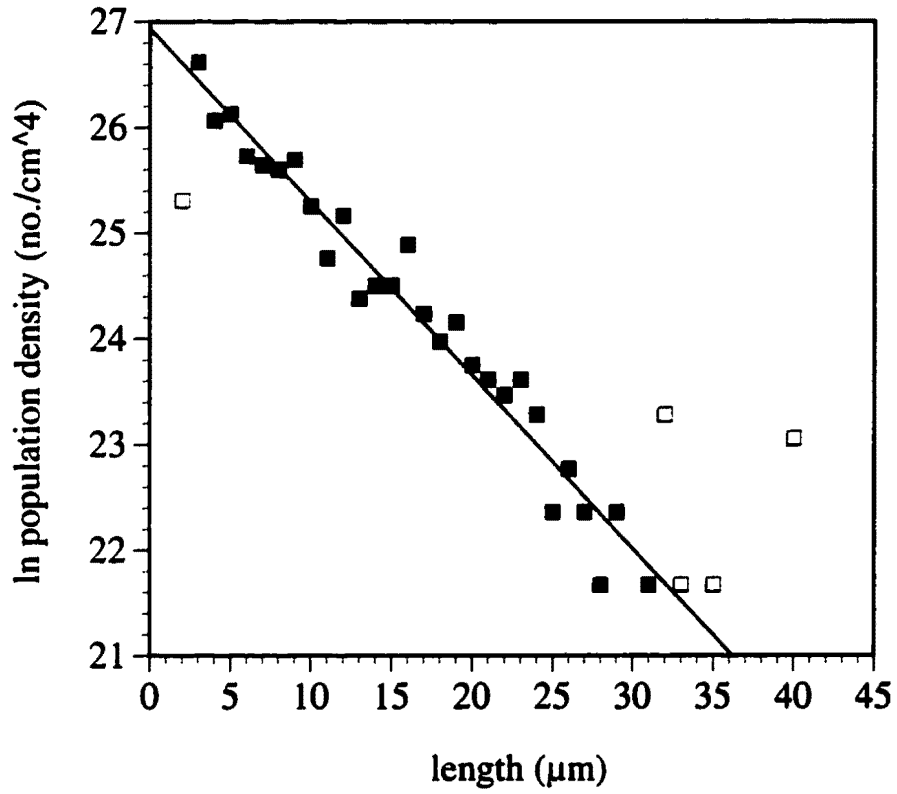


Figure 27. CSD for dike samples. Open points were not included in linear least squares fit.

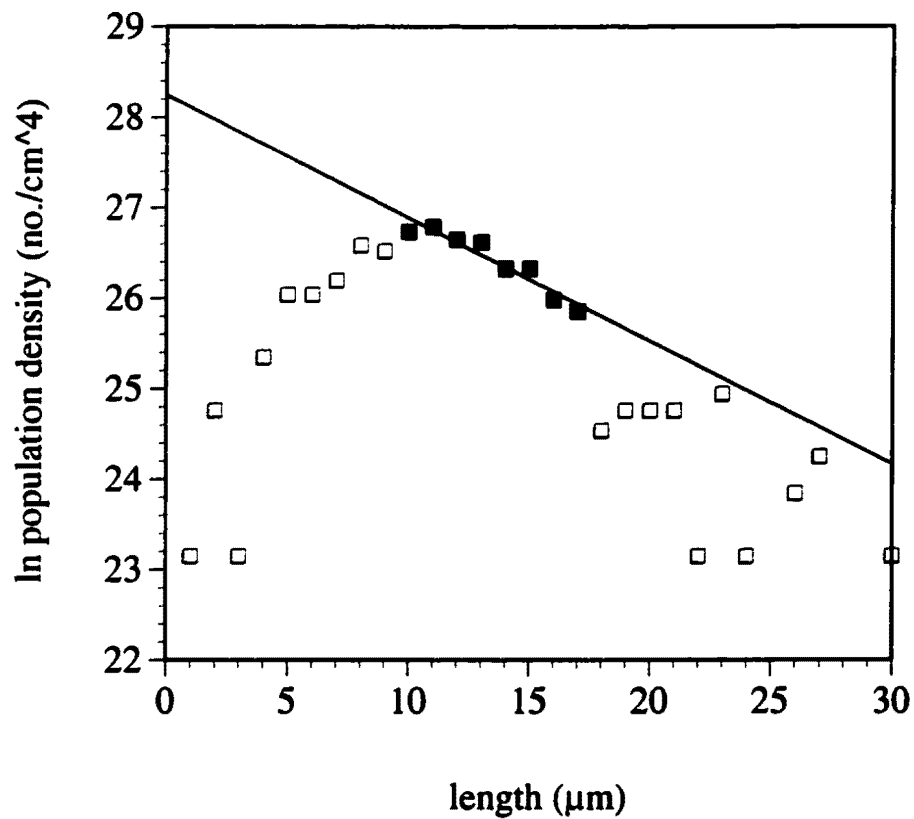


Figure 28. CSD for the shallow vent sample. Open symbols were omitted from CSD fit. Bell shape reflects loss of small crystals.

the trend is approximately linear, with a best-fit linear slope of -0.10 cm^{-1} and intercept of 23.2. CSD parameters yield a dominant crystal size of $10.0 \text{ }\mu\text{m}$ and an N_T of $1.1 \times 10^7 \text{ cm}^{-3}$. CSD data for plagioclase microphenocrysts are summarized in Tables 4 and 5.

Microlite Orientation

Microlite trend and plunge data for five flow front samples are plotted on lower hemisphere stereographic projections in Figure 32. The strike and dip of microlite flow banding measured in the field is plotted as great circles for comparison. In stereographic projections, microlite orientation frequency is shown as a percentage of the total number of microlites measured, and is depicted as a range of colors, with red corresponding to the highest orientation frequency ($>10\%$) and light green the lowest ($0-1\%$). Microlites are well oriented in each of the samples, as shown by red clusters on stereonet diagrams, where microlites in the highest orientation frequency ($>10\%$) class vary by no more than 15 degrees in trend and 10 degrees in plunge. Some scatter in orientation may be due to localized flow of microlites around microphenocrysts.

Microlites trend predominately east-west and typically have shallow plunges. Microlites in samples OD4, OD7, OD9, and OD11 are oriented sub-parallel to flow banding and trend consistently with the flow direction inferred from the geometry of the flow front (Figure 32). In contrast, sample OD13 has microlites that trend approximately normal to flow banding and do not appear to be aligned in the mean flow direction (i.e., they trend NW-SE rather than south).

Although the samples from the dike and conduit cores were not geographically oriented, orientation data may still be depicted on stereographic projections in an arbitrary reference frame. The relative degree of alignment can be surmised from the amount of

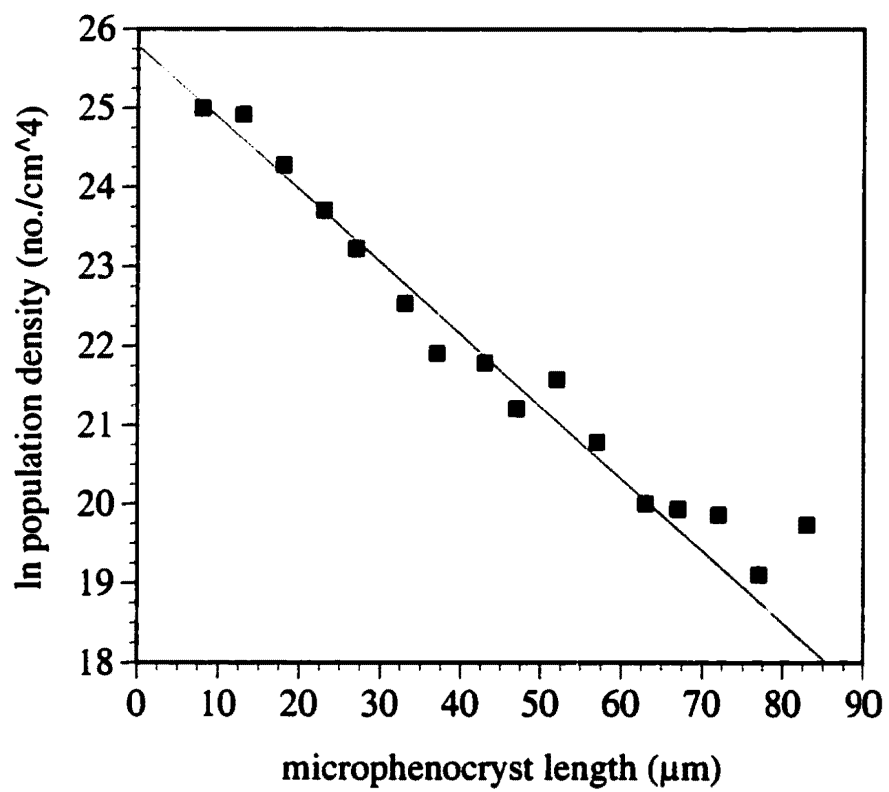


Figure 29. CSD for plagioclase microphenocrysts in flow front samples.

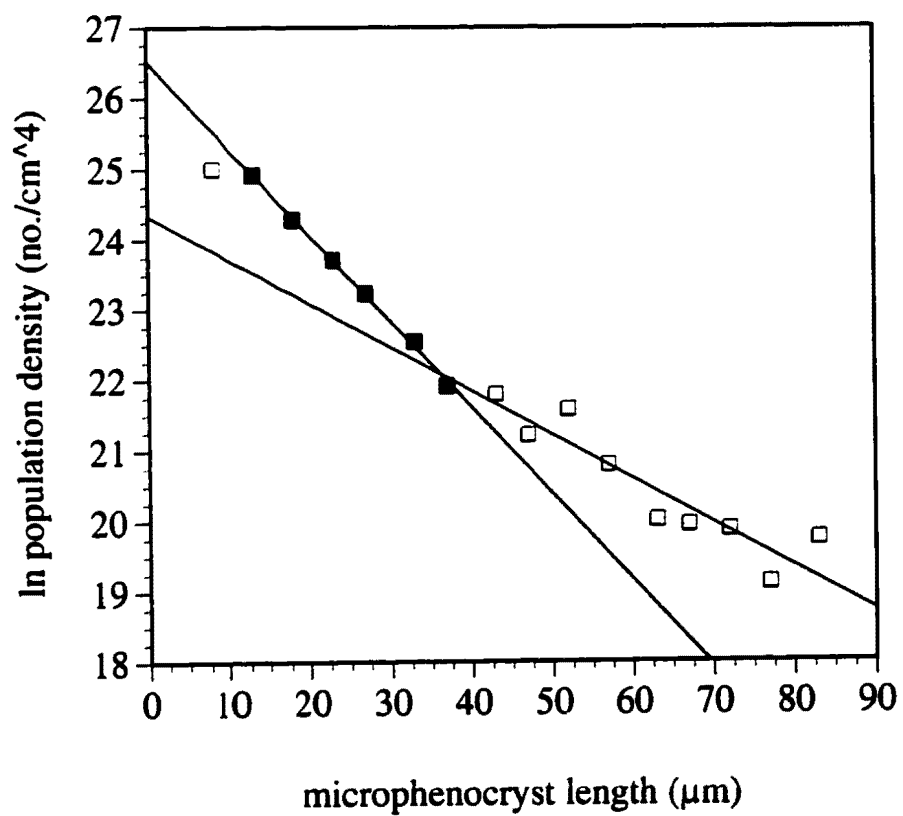


Figure 30. CSD for plagioclase microphenocrysts in flow front samples. Note break in slope at lengths greater than 40 μm . Slope break may represent a separate population of microphenocrysts.

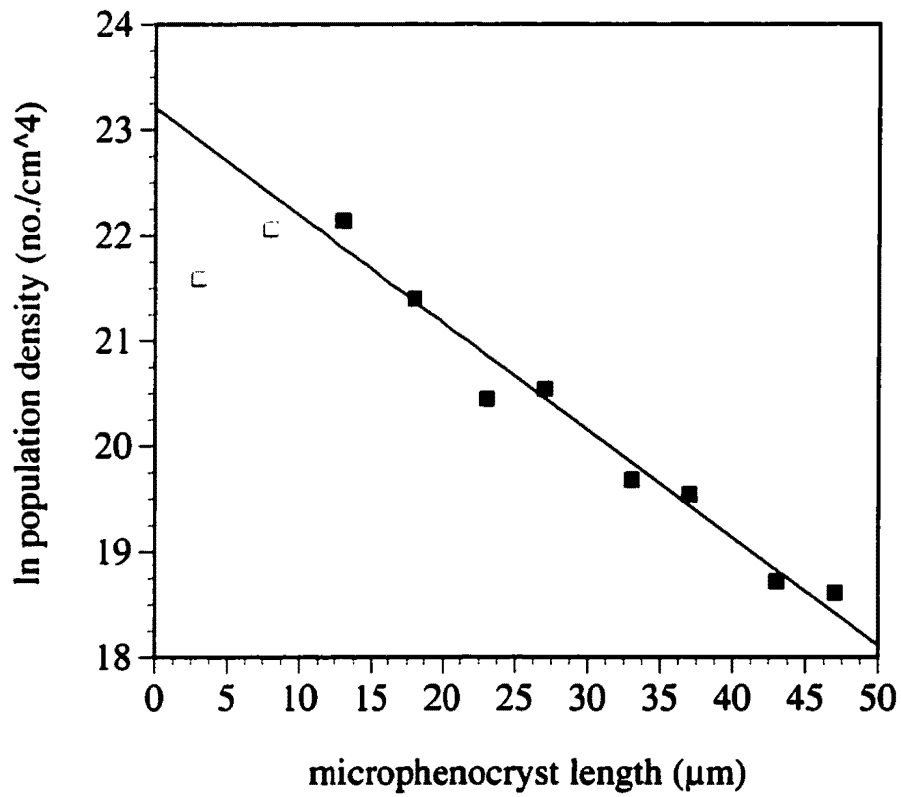


Figure 31. CSD for plagioclase microphenocrysts in the dike. Open symbols were omitted from linear regression analysis.

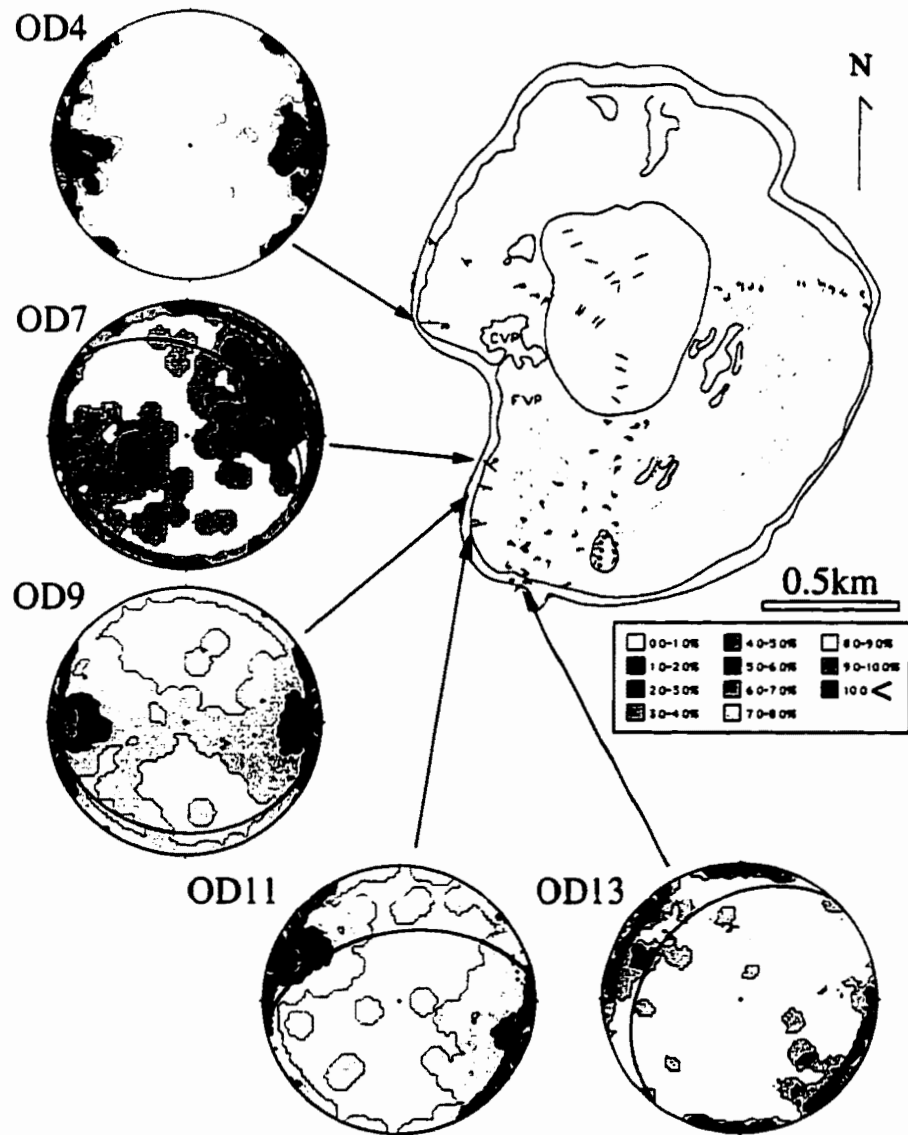


Figure 32. Microlite orientations in flow front samples. Stereonets show trend and plunge of microlites. Red signifies high population density (>10%) while blue is low (1%),

TABLE 4. CSD parameters for plagioclase microphenocrysts

Sample	slope (cm⁻¹)	ln n⁰	Dominant Size (μm)	N_T(no./cm³)
Flow front	-0.09	25.8	11.1	1.8x10⁸
Dike	-0.10	23.2	10.0	1.1x10⁷

TABLE 5. Measured microlite number density and N_T calculated from CSDs

Sample	No./cm ³ measured	No./cm ³ (N_T) computed	CSD equation
<i>Microlites^a</i>			
Flow front	2.9×10^8	4.5×10^8	$y = -0.26x + 27.8$
Dike	2.3×10^8	2.7×10^8	$y = -0.15x + 26.7$
Conduit	4.6×10^8	1.4×10^9	$y = -0.12x + 28.1$
<i>Microphenocrysts^b</i>			
Flow front	n.a.	1.8×10^8	$y = -0.91x + 25.8$
Dike	n.a.	1.2×10^7	$y = -0.10x + 23.2$

^a Flow front and conduit samples contain pyroxene while dike samples contain dominantly plagioclase with lesser pyroxene.

^b Microphenocrysts are plagioclase. Flow front and dike microphenocrysts were measured in BSE images and therefore true number density measurements were not available.

scatter in stereographic projections (Figure 33). In the conduit sample, microlites in the highest orientation frequency class trend over a range of approximately 25 degrees and plunge less than 10 degrees. Microlites in dike sample A are oriented over a narrower range of trend, approximately 10 degrees, while those in sample B are more scattered, with microlites forming three distinct clusters corresponding to three lineations. Orientation variability in dike and conduit samples is partly due to disruption of microlite alignment by vesiculation during flow.

Orientation measurements show that microlites in flow front samples are well-aligned, with most microlites trending east-west, subparallel to the inferred flow direction. Microlites in dike sample A are also well oriented, however microlites in dike sample B and the conduit sample are more scattered.

Discussion

The textural data presented above can be used to better constrain syn-eruptive crystallization and flow dynamics in the Obsidian Dome eruption. Here I show that textural information can be used to reasonably infer (a) that microlite nucleation and growth continued for the duration of the Obsidian Dome eruption, (b) that plagioclase crystallization shifted from nucleation-dominated to growth-dominated behavior during the late stages of eruption, and (c) the timescales of microlite and microphenocryst growth. From microlite orientation analysis, I assess (a) the relative degree of microlite alignment in the dike and on the surface, (b) upper and lower bounds on the amount of strain experienced by the flow, and (c) style extrusion of magma from the Obsidian Dome vent. When integrated, results from microlite size and orientations studies provide insight into crystallization and flow processes important in obsidian flow emplacement.

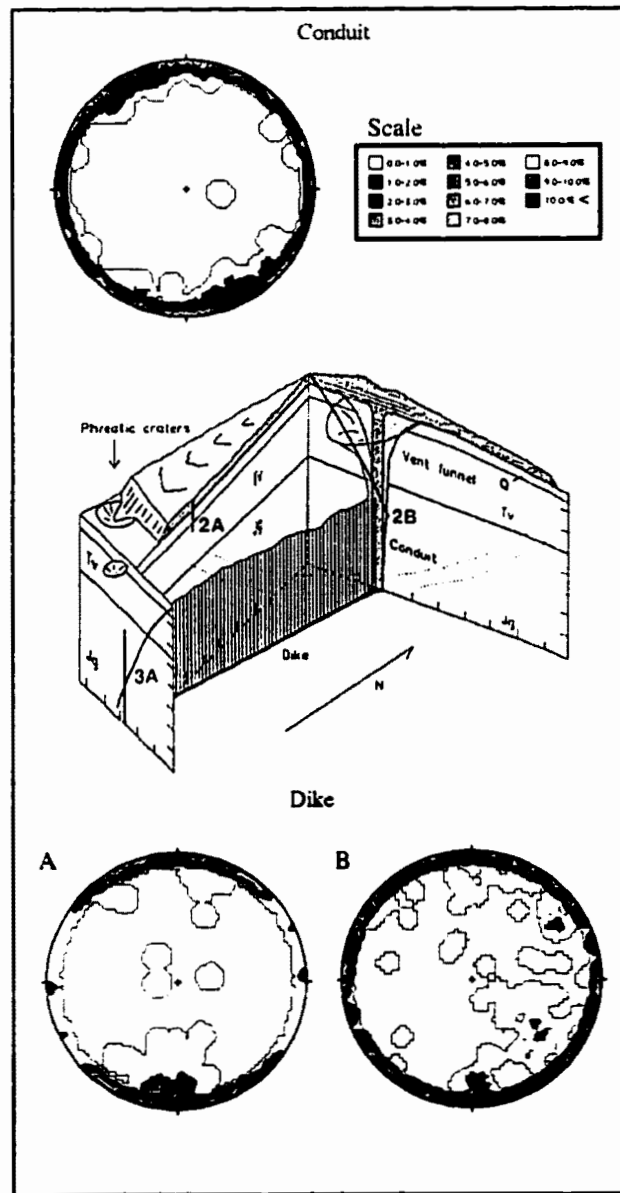


Figure 33. Microlite orientation in the conduit and dike of Obsidian Dome. Stereonets are not geographically meaningful however scatter in plots can be used as a measure of relative alignment. Dike sample A shows the most preferred alignment with >10% microlites trending and plunging within a 10 degree interval.

Syn-eruptive crystallization of Obsidian Dome

Previous work (e.g., Swanson et al., 1989; Taylor, 1991) on the textures and volatile contents of lavas from the flow, conduit, and dike of Obsidian Dome suggests a sequence of crystallization events that begins with pre-eruptive growth of phenocrysts and microphenocrysts, followed by pre- to syn-eruptive degassing-induced microlite nucleation and growth, and terminating in static crystallization and devitrification of the slower cooling interior of the dome and conduit. Microlite and microphenocryst size studies were conducted in order to highlight the interplay of magmatic degassing and crystallization during the intermediate stages of this sequence.

Microlite crystallization in Obsidian Dome probably occurred in response "to loss of a hydrous vapor phase" during decompression (Swanson et al., 1989). Because the liquidus temperature rises as the H₂O content of the melt decreases, microlite crystallinity is expected to increase with progressive degassing. Evidence in support of this hypothesis includes the observation that tephra clasts erupted immediately prior to effusion of the dome have higher H₂O contents and fewer microlites than less hydrous obsidian from the dome (Westrich et al., 1988). Microlite assemblages in samples from the dike, conduit, and flow can thus be interpreted as reflecting the progressive loss of H₂O during magma ascent and flow emplacement.

Microlite CSDs from flow front, dike, and conduit samples are summarized in Figure 34. The conduit regression line, fit to the narrow range of data from 10 to 16 μm , yields the highest number density ($N_T=1.4 \times 10^9 \text{cm}^{-3}$) and dominant size (8.3 μm) of the samples analyzed. This trend suggests a longer period of nucleation and growth relative to flow front and dike samples, and potentially signals lower effusion rates as the eruption waned. Cooling rates were presumably higher in the dike margin and flow front than in the conduit, and as a result their microlite size distributions are less-evolved (not bell-shaped),

with more crystals preserved at smaller size classes. The distinction between CSDs for the flow front and dike, namely the different slopes and intercepts of regression lines (Table 3), are due to differences in the mineral assemblages of dike and flow samples. That is, CSD trends reflect to a pyroxene-rich assemblage in the flow front, and a feldspar-dominant assemblage in the dike. The higher H₂O contents in the dike (~1.5 wt%) may have aided in crystallization of plagioclase and pyroxene by decreasing the viscosity of the melt, and consequently, increasing the diffusion rates of crystal forming constituents in the melt.

It is important to note that all samples contain both plagioclase and pyroxene microlites (cf. Fig 11), and may have undergone simultaneous crystallization of these phases (e.g., along a cotectic). Based on the observed decrease in plagioclase microlite number density from the dike to the flow front (cf. Figure 11), I infer that the plagioclase nucleation rate decreased during dome effusion. Pyroxene microlite number densities increase from the dike to the flow front and show a slight decrease in the last erupted conduit lava relative to the flow front. These trends suggest that pyroxene nucleation increased during transport from the dike to the flow front and may have decreased towards the end of eruption. The predominance of pyroxene microlites in all samples suggests continuous pyroxene nucleation throughout flow emplacement. Formation of pyroxene nuclei may be kinetically favored in rhyolitic melts for two reasons: (1) the presence of Fe and Mg causes breakdown of the Si-O framework structure in the melt (Kushiro, 1975); the change in silicate liquid structure enlarges the stability field of the silica-poor phase, and (2) the structural simplicity of inosilicate minerals promotes a smaller critical nucleus size (Naney, 1983).

CSD interpretations rest on the assumption that the samples analyzed represent a time sequence in which the glassy margin of the dike represents magma emplaced and quenched prior to the obsidian exposed in the flow front. The relatively high H₂O contents

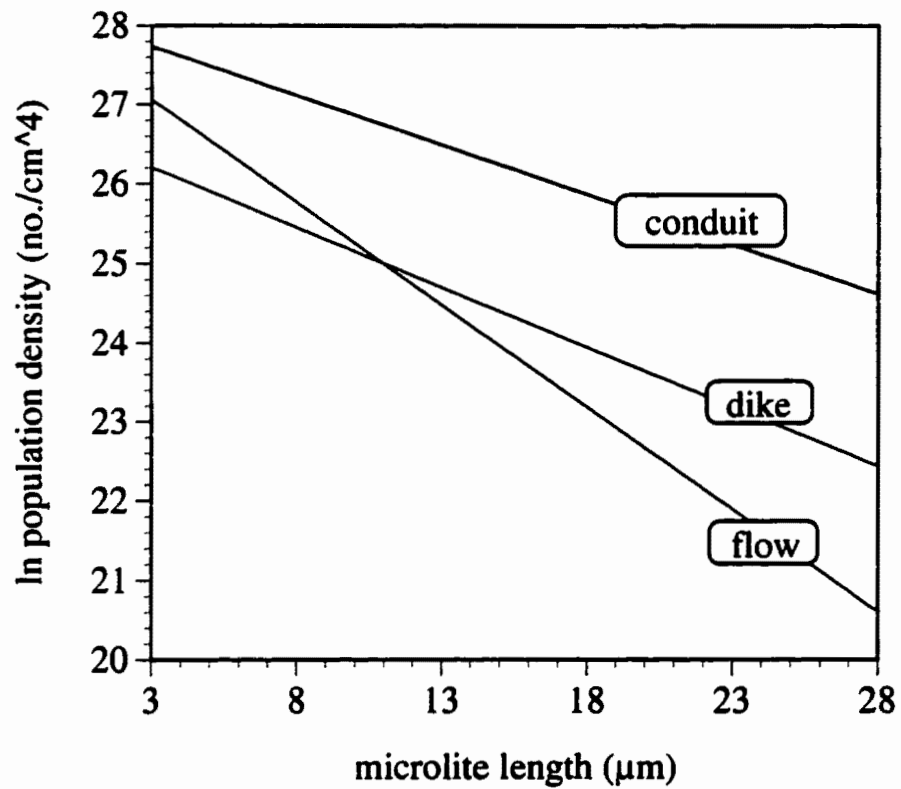


Figure 34. CSDs for flow front, dike, and vent samples. Variation in flow front and dike slopes reflects different mineral assemblages. The conduit CSD shows the effects of extended growth (lower slope) and nucleation (higher intercept).

measured in the dike (~1.5 wt%) compared to the flow (~0.1 wt%; Westrich et al., 1988) supports this assumption in that volatile contents of eruptive products generally decrease during eruption due to progressive degassing accompanying magma ascent, although the mechanism for such degassing remains controversial (e.g., Eichelberger et al., 1986; Fink et al., 1992).

Growth of pyroxene microlites on the flow surface is suggested by variations in the average microlite size in flow front samples. Assuming that mean flow was normal to the approximately north-south trending feeder dike (the validity of this assumption will be tested in the orientation section), sample OD4 traveled the farthest and hence is the oldest flow front sample, while samples OD7, OD9, and OD11 are younger and approximately equidistant from the vent. The average microlite length of 8.7 μm in sample OD4 is more than 2 μm greater than the average of the three southwest flow front samples (~6.4 μm). The difference in average microlite length represents a lower bound on the amount of pyroxene growth on the flow surface, as microlites measured in the latest erupted vent lava (conduit sample) and near vent lava (OD13) have larger mean lengths (12.1, 9.1 μm respectively).

Microlite assemblages in the flow front, dike, and conduit reflect a sequence of multiphase crystallization and growth involving: (1) early nucleation and growth of plagioclase and pyroxene, followed by (2) a decrease in the nucleation rate of plagioclase with continued nucleation of pyroxene, and ending in (3) growth of microlites of plagioclase and pyroxene in the vent and flow front prior to solidification. The shift in nucleation behavior of plagioclase may signal changes in the crystallization kinetics as degree of plagioclase supersaturation in the melt decreased and the melt viscosity increased. Such a shift in plagioclase crystallization behavior may be evident in microphenocrysts CSDs.

Microphenocryst Crystallization

The shift from crystal nucleation to growth-dominated behavior in magmatic systems is controlled largely by the degree of supersaturation, an unstable melt state in which the concentration of a phase(s) is greater than its solubility (Figure 35).

Supersaturation generally occurs in response to undercooling, or the temperature difference between the liquidus of a melt and the point at which it actually begins to crystallize.

Mechanisms to undercool a magma include rapid temperature drops, or loss of a volatile phase (e.g., Swanson et al., 1989). Ideally, systems with high degrees of supersaturation of a specific phase(s) will respond by nucleating numerous small crystals in an attempt to reach chemical equilibrium. As the degree of supersaturation decreases, growth on preexisting crystals and newly formed crystal nuclei takes over. My data indicate how the Obsidian Dome system responded to degassing (and undercooling) of the magma from 1.5 (dike) to 0.1 wt% H₂O (flow front) by both crystal nucleation and growth.

An increase in pyroxene microlite N_a of approximately one order of magnitude from the dike to the flow front suggests that the magma responded to degassing, at least in part, by nucleating more pyroxene crystals (e.g., Figure 11). Several lines of evidence suggest that continued nucleation and growth of plagioclase on preexisting microlites and microphenocrysts occurred as the system progressed to lower degrees of supersaturation. First, there is a general increase in the number density and average size of plagioclase microphenocrysts from the dike to the flow front (cf., Figure 13). These increases are evident in microphenocryst CSDs for the dike and flow front samples as an upward shift in n^0 and a decrease in the CSD slope from the dike to the flow front, respectively (Figure 36). I interpret the upward shift in n^0 to represent the addition of microphenocrysts to the population by growth of microlites in the dike (i.e., an increase in the total number of crystals). This inference is supported by an overlap in the CSDs for plagioclase microlites

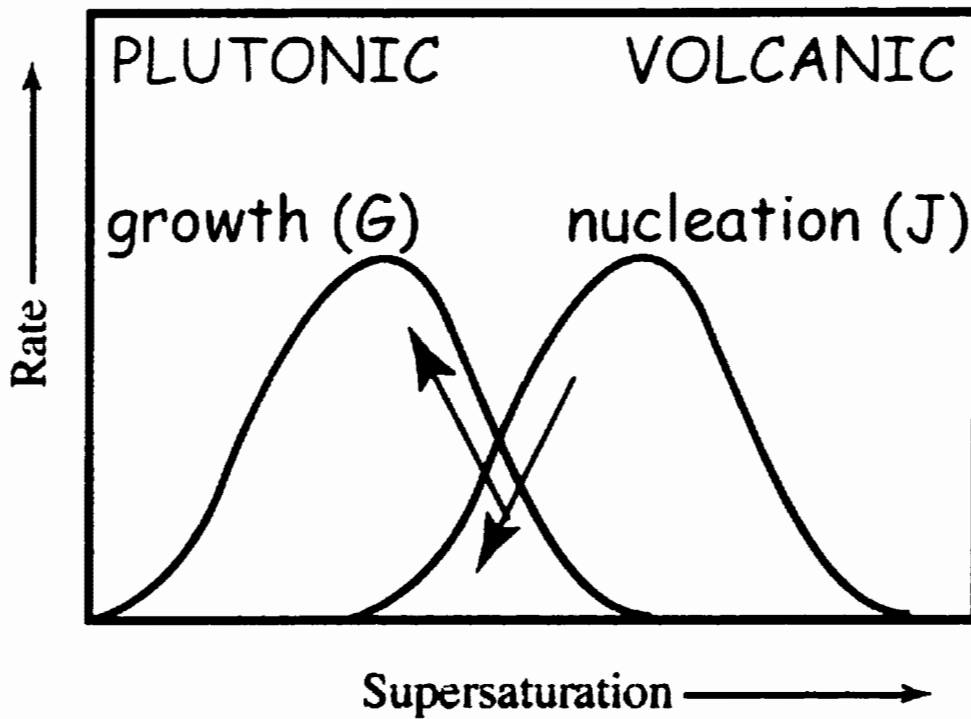


Figure 35. Crystallization kinetics for plutonic and volcanic regimes. At high degrees of supersaturation, crystallization is nucleation dominated whereas at low supersaturations, growth dominated crystallization occurs.

from the dike and microphenocrysts in the flow front, as shown in Figure 37 by the coincidence of plagioclase microlite and microphenocryst CSDs between 15 and 40 μm in length. The similarity between plagioclase microlite and microphenocryst CSDs in the small size range suggests that some microphenocrysts grew from preexisting microlites in the dike and hence are a part of the same microlite population. The distinct break in slope at microphenocryst lengths greater than 40 μm may represent a separate, earlier formed population of microphenocrysts (e.g., Cashman, 1988). If indeed some microphenocrysts represent a mature stage of microlite crystallization, the increased abundance of plagioclase microphenocrysts in the flow front relative to the dike may be due to continuous, growth-dominated, microlite crystallization in the shallow conduit and during flow on the surface. The documented change in the average crystal shape from microlites to microphenocrysts (long thin prisms to thicker, more equant prisms) is further evidence of a shift in crystallization from nucleation- to growth-dominated behavior. Hammer et al. (1999) demonstrated that such a shift in crystallization regime in Mt Pinatubo samples was correlated with changes in microlite shape from tabular to prismatic forms. Such changes in crystal shape are expected if surface energy minimization is a driving force in crystal growth (Hammer et al., 1999). The surface area to volume ratio reduction accompanying the change in shape from plagioclase microlites to microphenocrysts in Obsidian Dome is thus interpreted to be a consequence of a change in the relative importance of crystal nucleation and growth during the crystallization process.

Crystallization Kinetics

The relatively low abundance of plagioclase microlites in the flow front and conduit reflects a change in the kinetics of plagioclase crystallization with time. Crystallization experiments demonstrate that at high supersaturations crystallization is dominated by

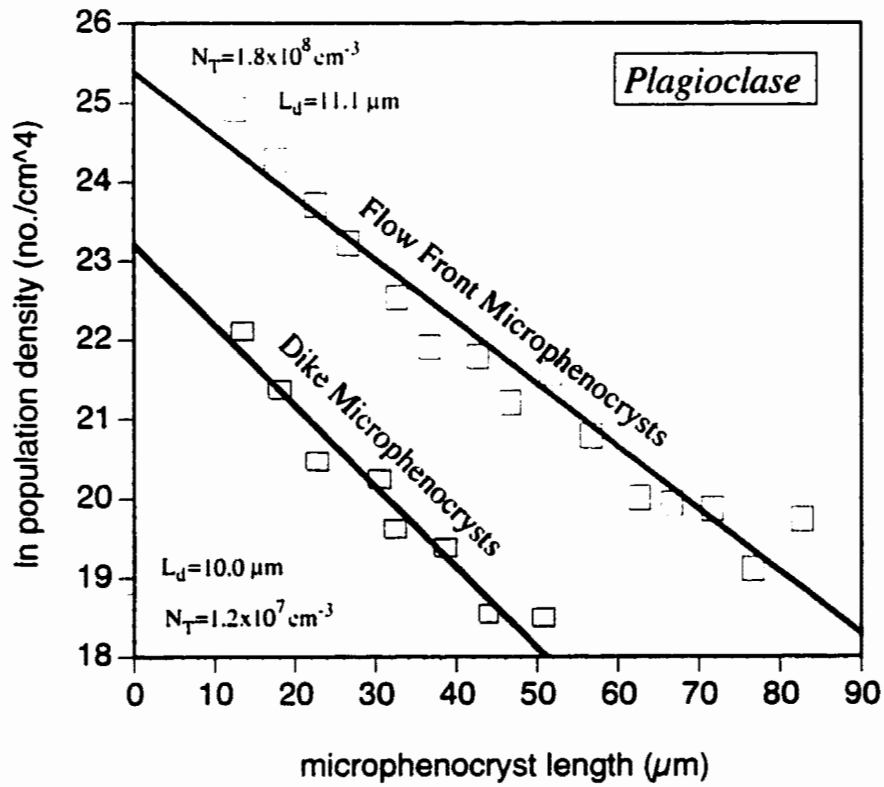


Figure 36. Plagioclase microphenocryst CSDs for (a) the dike and (b) the flow front.

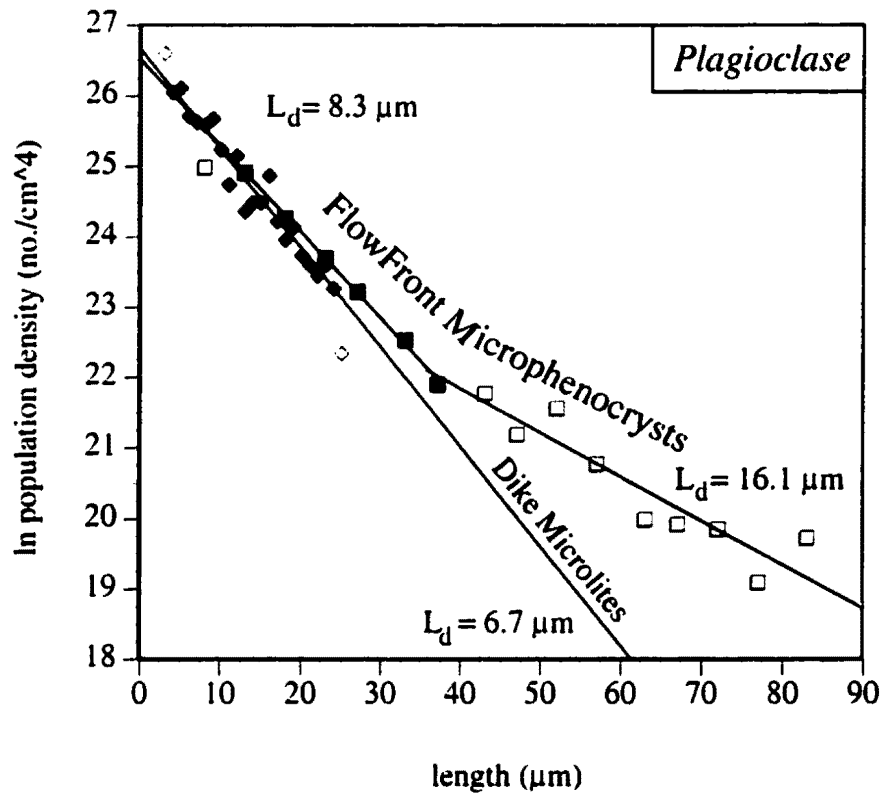


Figure 37. CSDs for (◆) plagioclase microlites in dike samples and (■, □) plagioclase microphenocrysts in the flow front. CSDs for microlites and microphenocrysts coincide between 15 and 35 μm , suggesting they are part of the same population.

nucleation (e.g., Lofgren, 1980; e.g., Figure 35), and as the degree of supersaturation decreases, a shift towards growth-dominated crystallization may occur. Mechanisms for the inferred shift in nucleation behavior of plagioclase are difficult to verify as low pressure experimental constraints on phase equilibria in rhyolitic systems are scarce (e.g., Swanson, 1977; Naney and Swanson, 1980). Naney (1983) reports that at temperatures comparable to those estimated for the Obsidian Dome magma (i.e., 924°C; Vogel et al., 1989), the liquidus phase assemblage in synthetic, Fe,Mg-bearing granitic melts at 2 kbar and 0.5 wt% H₂O includes clinopyroxene and plagioclase. He finds that plagioclase nucleation is sluggish in these experiments, and that often this phase does not crystallize until undercoolings of at least 200°C are achieved. Similar observations have been made in other high pressure (8 kbar) experimental studies (e.g., Swanson, 1977; Lofgren, 1974). Such experimental insights and the common petrographic observation that microlite, microphenocryst, and phenocryst assemblages rarely contain quartz (e.g., Sampson and Cameron, 1987; Vogel et al., 1987; Swanson et al., 1989) illustrates the sluggish nucleation behavior of tectosilicate minerals in high silica melts.

Based on these experiments, I suggest that despite the high degrees of supersaturation attendant with large undercoolings, plagioclase nucleation was suppressed by large viscosity increases expected to occur concomitantly with exsolution of H₂O from the magma. A decrease in melt-H₂O content from 1.5 to 0.1 wt% (i.e., the difference in H₂O between the dike and flow front) would result in an increase in melt viscosity of approximately one order of magnitude (e.g., Hess and Dingwell, 1996). Such an increase would inhibit mobility of atoms and molecules, and hence diffusion rates in the melt. Formation of stable nuclei is highly dependent on both the diffusion rates of crystal-forming species in the melt, and the critical size for spontaneous growth. Alternatively, the lack of abundant plagioclase in flow front and conduit samples may simply reflect low plagioclase supersaturations in later erupted lavas.

Timescales of microlite and microphenocryst growth

The timescales of eruptive processes such as crystallization and flow emplacement in active silicic systems are readily documented from direct observations (e.g., Mt. St. Helens; Swanson and Holcomb, 1990). But, emplacement dynamics of obsidian dome eruptions are enigmatic because rhyolite flows have not been scientifically observed while active. Crystal size distributions can be used to determine crystal growth rates (G) in magmatic systems where crystal growth times (t) are constrained by direct observations of actively forming domes (e.g., Cashman, 1988; Hammer et al., 1999). Alternatively, crystal growth times can be estimated from independently determined growth rates in systems where the amount of crystal growth is known. Here I estimate crystal growth intervals for plagioclase microphenocrysts in flow front samples given two possible scenarios: (1) plagioclase microphenocrysts in the flow front grew continuously from microlites in the dike, and (2) plagioclase microphenocrysts grew from microphenocrysts in the dike. The first scenario is based on the assumption that microphenocrysts in the flow front represent the mature stage of microlites in the dike, and thus are a part of the same population. The overlap in plagioclase microlite and microphenocryst CSDs lends support to this assumption (cf. Figure 32). Similarly, the second case assumes continuous growth of microphenocrysts during transport from the dike to the flow front.

The dominant crystal size, determined from CSD plots, is a function of the growth rate (G) and growth interval (t). Since there are no constraints on the eruption rates of Obsidian Dome, crystal growth rates are inferred from (1) experimental studies on crystallization in rhyolitic systems (e.g., Geschwind and Rutherford, 1995) and (2) estimates from CSD studies of active silicic dome eruptions (Cashman, 1992). Geschwind and Rutherford (1995) determined plagioclase growth rates of $10^{-6} \mu\text{m s}^{-1}$ in dynamic crystallization experiments on residual rhyolitic glass from Mt. St. Helens. In these

experiments, they induced crystallization over a period of several hours by decompressing (and dewatering) samples, thus simulating crystallization in response to degassing during ascent and produced undercoolings estimated to range from 60-200°C. Their measurements are consistent with the lower bound determined by Cashman (1992) from CSD studies of Mt. St. Helens dacite. Using the experimentally determined plagioclase growth rate of $10^{-6} \mu\text{m s}^{-1}$, and assuming plagioclase microphenocrysts grew from the same population of microlites in the dike, a growth time of 4.4×10^6 s, or 51 days would be required to produce the total amount of crystal growth ($4.4 \mu\text{m}$, i.e., the difference in dominant crystal size (L_d) between microphenocrysts and microlites; Table 4). The time interval similarly determined for growth of flow front plagioclase microphenocrysts from microphenocrysts in the dike is 1.1×10^6 s, or 13 days. These estimates represent upper and lower bounds on crystal growth time as magma flowed from the dike to the flow front, and hence, can be used as a measure of the effusive eruption duration.

Microlite growth times may provide quantitative constraints on the duration of eruption of Obsidian Dome. The estimates are also useful in determining the rates of extrusion. Assuming a flow volume of 0.09 km^3 (dimensions measured in the field and from Miller, 1985), and an eruption duration of 51 days, the mass eruption rate is approximately $2 \times 10^6 \text{ m}^3 \text{ day}^{-1}$. This estimate is one order of magnitude greater than the observed average effusion rate of $0.16 \times 10^6 \text{ m}^3 \text{ day}^{-1}$ for the 1991-1992 Mt. Unzen dacite dome (Nakada, 1992), and of the same magnitude as the average extrusion rate for the Mt. St. Helens dome emplaced between Oct. 1980 and Oct., 1981 ($\sim 1 \times 10^6 \text{ m}^3 \text{ day}^{-1}$; Swanson and Holcomb, 1990).

Extrusion rate estimates $11\text{-}3 \text{ m}^3/\text{s}$ for Obsidian Dome were determined by Fink and Griffiths (1998) in laboratory analog models. Their estimates indicate an eruption duration of approximately 200 days. Flow rates based on microlite measurements in this

study are comparable and add further constraint to both the eruption rates and durations of the Obsidian Dome complex.

Microlite Orientation

The orientation distribution of microlites is useful for understanding the style of lava extrusion and the relative amounts of strain experienced in the dike, conduit, and flow. Microlites in four of the five flow front samples are oriented parallel to the flow direction inferred from the geometry of the flow front (we assume that the flow direction is normal to the flow front; see also Manga, 1998). These microlites trend subparallel to flow banding and plunge shallowly, forming a lineation in the plane of flow banding. In contrast, microlites in sample OD13 have an average trend of nw-se, nearly normal to the strike of flow banding, and do not appear to be aligned in the direction of flow inferred from the geometry of the flow front.

Sample OD13 was collected from along the inferred trend of the subsurface feeder dike (~N10E; Fink and Pollard, 1983) and may record strain inherited from local extrusion from a linear vent. Figure 38 is a schematic map of Obsidian Dome showing the mean trend of microlites in the flow front and the projected trace of the subsurface feeder dike (Fink and Pollard, 1983). Microlites in all samples trend at high angles to the dike (minimum of ~70 degrees for sample OD13) and plunge subhorizontally. This geometry suggests that lava extruded from the linear vent (e.g., Sampson, 1987) and that during flow on the surface, microlites rotated to subhorizontal positions. Rotation of microlites during surface flow occurred after extrusion, as evidenced by shallowly plunging microlites in all samples. The correlation between microlite orientation and flow direction in flow front samples may reflect the combined effects of alignment in the dike and reorientation of microlites on the surface. The relative influences of dike and surface flow

in determining final microlite orientation can be estimated by analyzing the variance in microlite orientation distributions.

Assuming microlites align themselves in the direction of flow (Manga, 1998), microlite orientation will vary as a function of strain and flow type (e.g., pure vs. simple shear). Figure 39 shows the standard deviation of microlite trend as a function of strain in simple and pure shear flows as calculated by Manga (1998). These calculations assume dilute suspensions ($N_V \ll 1$) of microlites with aspect ratio of 5, and assume an initially random orientation distribution. According to Figure 39, measured standard deviations of microlite trends in flow front, dike, and conduit samples imply simple shear strains of approximately 3.3, 2.4, and 1.5 respectively or pure shear strains of 1.1, 0.9, and 0.35 respectively. In general, flow front samples exhibit the largest strains, while dike and conduit samples show smaller strains.

The approximate timing of microlite alignment can be assessed by comparing the strain inferred from orientation distributions (e.g., Figure 39), and the total strain experienced during flow on the surface. Flow front samples represent the uppermost 10 meters of lava in the dome and probably experienced a large component of pure shear strain as a result of flow. Indeed, the surface shear stress of the flow is expected to be low, and flow in the vicinity of the surface is well approximated by a pure shear straining flow (Wylie and Lister, 1998). The total pure shear strain, or strain due to axial spreading of the flow on the surface, can be estimated if we assume an average dome radius of 750 meters and thickness of 50 meters. The total volume (assumed constant) of the flow based on these dimensions is 0.09 km^3 . The equivalent radius of a sphere of equal volume is 280 meters. Horizontal spreading of this fluid sphere yields an estimated extensional strain of 1.7 (Figure 40). This pure shear estimate is greater than the strain value of 1.1 inferred from the standard deviation in trend of flow front microlites (see Figure 35), and suggests that flow on the surface was sufficient to produce the preferred alignments in the flow

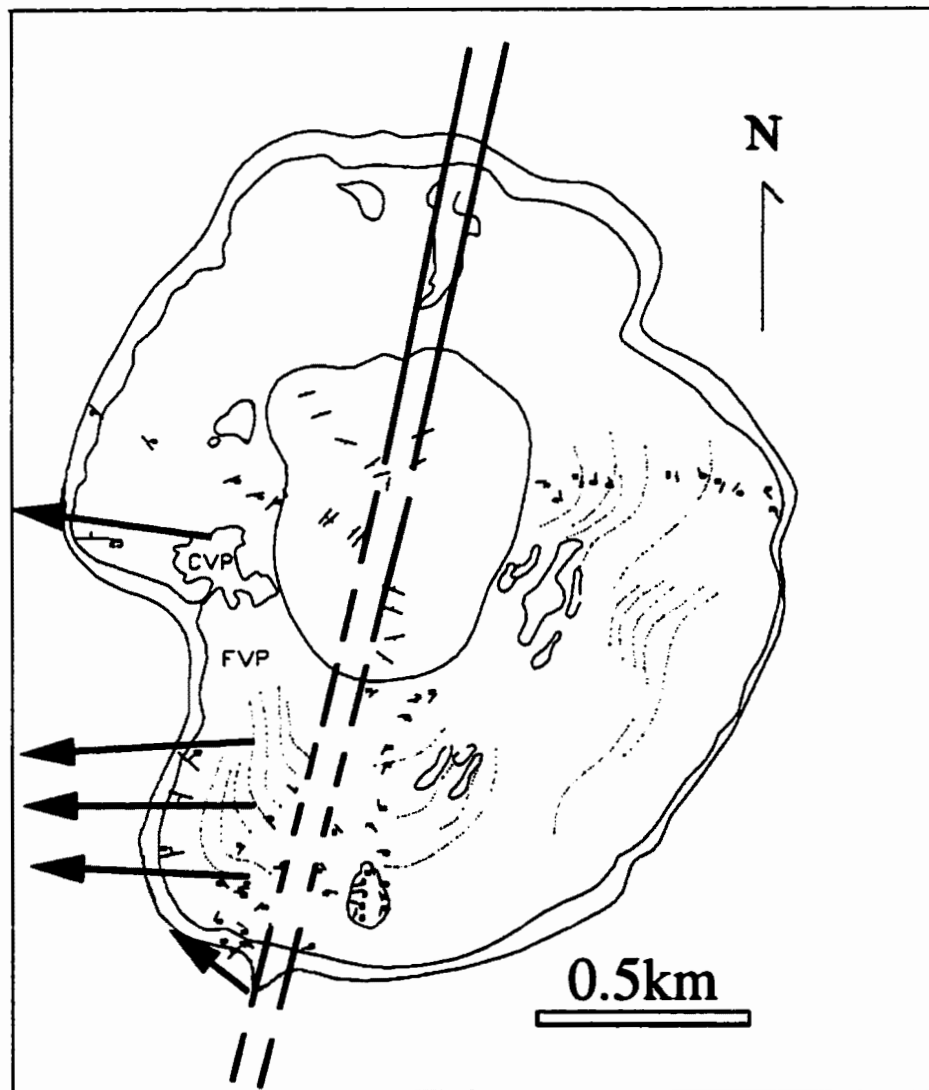


Figure 38. Obsidian dome and the inferred trace of the subsurface feeder dike showing mean microlite lineation directions (large arrows).

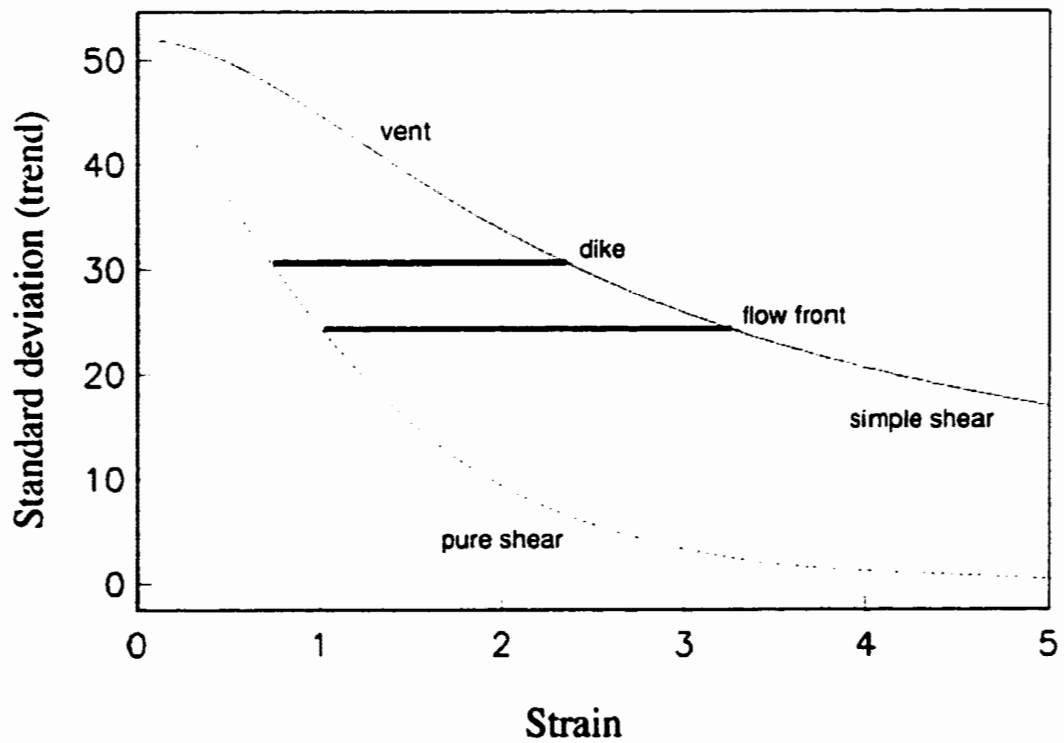


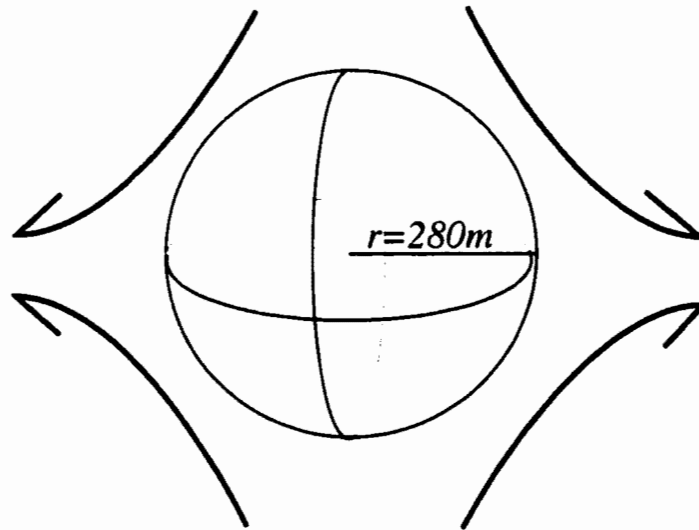
Figure 39. Standard deviation of microlite trend versus strain for rods of aspect ratio 5 for simple and pure shear flows. Intersections of curves with extrapolated standard deviations yields estimates of strain due to flow in the vent, dike, and flow front. Modified from Manga (1998).

front. Microlite orientation in dike and conduit samples imply smaller pure shear strains.

Smith and Houston (1994) analyzed mesoscopic folds and banding to demonstrate that flow above and proximal to the vent of the Minyon Falls obsidian flow, Australia, was characterized by pure shear. They also showed that more distal parts of the flow were governed by simple shear kinematics, as fold patterns indicated lateral shortening due to flow advance. If flow in the distal portions of Obsidian Dome was characterized by simple shear, the simple shear strains of 3.3 inferred from Figure 39 might be more meaningful estimates of the strain experienced during flow on the surface. Simple shear kinematics have also been inferred for flow at dike margins based analyses of stretched vesicles (Coward, 1980) and oriented crystals (Shelley, 1985). In this context, the orientations in the dike imply strains of approximately 2.4. It is likely that flow in Obsidian Dome had components of both pure and simple shear, and therefore the estimates of strain inferred from orientation distributions serve as limits on the possible strains experienced by the lava.

Summary

The dynamics of crystallization and flow in the late Holocene Obsidian Dome eruption were investigated using two different approaches: (1) microlite size distribution analysis, and (2) microlite orientation analysis. These two approaches yielded quantitative results regarding the nature of the kinetics of microlite nucleation and growth, the duration and magnitude of crystallization, the style of magma extrusion, and the relative amount of strain recorded in different volcanic regimes. When integrated, these two approaches may provide constraints on eruption rates.



*Consider Spreading of a rhyolite Sphere
of Volume 0.09 km^3*

Assuming Volume is Conserved

Axial (pure shear) Strain (γ) = $R-r/r=1.7$

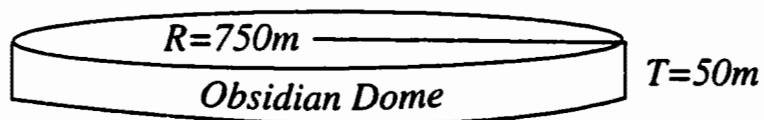


Figure 40. Pure shear strain calculation for surface flow.

Crystallization History

Microlite crystallization in Obsidian Dome was a complex process involving (1) early crystallization of plagioclase and pyroxene microlites, (2) a shift in plagioclase crystallization kinetics from nucleation- to growth-dominated behavior with continued nucleation of pyroxene microlites, and (3) growth of pyroxene microlites and plagioclase microphenocrysts during flow in the conduit and on the surface. These processes highlight the importance of kinetic barriers to crystal nucleation in silicic systems such as viscosity and undercooling. Interpreting crystal size distributions as a means of quantifying eruptive parameters may be complicated by the fact that microlite assemblages are polymineralic. However, the relative shapes of CSDs reflect different crystallization and cooling histories in the flow front, dike, and conduit. Plagioclase growth times of 13-51 days were determined from CSD relations. These growth intervals provide the first quantitative estimates of eruption duration for the Obsidian Dome system.

Flow History

The eruption of Obsidian Dome from a fissure is likely considering that the eruptions of the Inyo domes are believed to be linked to emplacement of a dike near the surface (e.g., Bailey, 1982; Pollard et al., 1984; Miller, 1985). Three dimensional orientation measurements and analyses of variance in these data lends significant support to the hypothesis that Obsidian Dome erupted, at least initially, from an elongate vent. Simple shear strain increases from 2.4 in the dike to 3.3 in the flow front, possibly reflecting the difference in transport distance between the two volcanic regimes. Strain inferred from the degree of microlite alignment in the flow front is smaller than the total strain estimated for

Extrusion Rate

Strain rates (strain/time) and extrusion rates (volume/time) of obsidian dome eruptions are unknown due to the lack of direct observations. Here I estimate the strain rate for the latest extrusive episode using the upper bounds in crystal growth interval (51 days) and simple shear strain (3.3 for flow front). These values yield an estimate of $7.5 \times 10^{-7} \text{s}^{-1}$. Considering the flow volume of 0.09 km^3 , and an eruptive duration of $4.4 \times 10^6 \text{ s}$, extrusion rates of $1.9\text{-}23.1 \text{ m}^3 \text{s}^{-1}$ calculated for Obsidian Dome are within an order of magnitude for measured extrusion rates of Mt. Unzen and Mt St. Helens. These estimates are, of course, highly dependent on the choice of growth rates for plagioclase microlites, as an order of magnitude smaller rate will translate to lower dome extrusion rates. These estimates provide additional quantitative constraints on extrusion rates and strain rates for Holocene rhyolite flows.

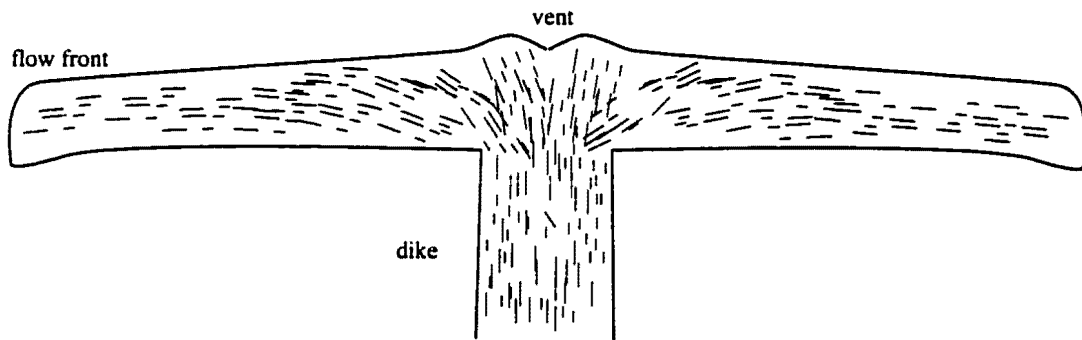


Figure 41. Schematic view of microlite orientation development in Obsidian Dome.

CHAPTER III

CONSTRAINTS ON RHEOLOGY OF OBSIDIAN FLOWS BASED ON MESOSCOPIC FOLDS

Introduction

Silicic lava flows provide an opportunity to examine and interpret the deformation behavior of viscous fluids throughout a wide range of flow conditions. Studies of active lava flows and domes allow direct rheological estimates for andesite and dacite lavas (e.g. Anderson and Fink, 1992; Nakada et al., 1995). However, the dynamics of rhyolitic obsidian eruptions are difficult to constrain because "no geologist has ever witnessed an obsidian in motion" (Nichols, 1941). Yet rhyolitic activity has dominated the late Holocene volcanic record in many parts of Oregon and California (e.g. Newberry Volcano, South Sister Volcano, OR; Medicine Lake Volcano, Mono-Inyo Craters, CA). The textural and structural complexities of these Holocene flows are well preserved, and consequently they serve as nearly pristine records of magmatic flow and deformation. The purpose of this chapter is to describe the deformation style and mechanisms of centimeter- to meter-scale buckle folds in obsidian lavas, and to attempt to constrain the relative rheologic properties of the lavas in which they are formed.

Rheologic Background

While models describing the formation of obsidian flows address the development of pumiceous zones and the distribution of volatiles throughout flows, they do not address rheologic variations expected from heterogeneous distributions of bubbles and crystals in the lava.

The rheology of rhyolitic magma has been described experimentally as a function of crystal content, water content, melt composition, and temperature (e.g. Shaw, 1972; Murase and McBirney, 1973; Spera et al., 1988). Recently, workers have considered the effects of bubbles on shear viscosity. While Stein and Spera (1992) suggested that bubbles will increase the effective viscosity of the melt, other studies indicate that the addition of bubbles to melt may actually cause a decrease in shear viscosity (Bagdassarov and Dingwell, 1992; Manga et al., 1998). Despite contrasting experimental and theoretical results, it is commonly assumed that bubbles will greatly increase viscosity of the melt, a view that has significant implications for models of magma ascent and vesiculation in volcanic conduits (e.g. Jaupart and Allegre, 1991; Dobran, 1992). Here I provide new constraints on the rheology of bubble-bearing rhyolitic melts based on the distribution of fold wavelengths in Big and Little Glass Mountain obsidian flows (Figure 42), using both Newtonian and non-Newtonian buckling theory (e.g. Biot, 1961; Smith, 1979).

Mesoscale Deformation in Obsidian Flows

Deformation of rhyolitic lavas occurs on many scales and is well preserved in Holocene flows. Large-scale (tens of meters) folding forms both recumbent folds and evenly spaced ridges and valleys on flow surfaces (Figure 43). The geometric relations of these folds have been used to infer flow properties such as viscosity and shear mechanisms

(e.g. Fink, 1980, 1984; Smith and Houston, 1994). Microscopic flow dynamics have been investigated by measuring microlite (crystals < 30 μm size) orientation distributions (Manga, 1998). Mesoscopic structures such as buckle folds and boudinage, although very common throughout the flows, have not been studied in detail (Figure 44).

Flow Layering

Mesoscopic folds and boudinage arise as flow layering deforms during flow advance. Flow layering is a pervasive structure in obsidian flows (e.g. Manley and Fink, 1987; Swanson et al., 1989). Three types of flow layers exist (Figure 45). Ubiquitous sub-millimeter scale flow layering is marked by planar variations in microlite concentration. Pumiceous layering consists of planar variations in microlite or vesicle concentration. Textural layering occurs in interlayered obsidian-pumice assemblages and is defined by the alternating arrangement of glassy and pumiceous layers of relatively uniform thickness. Texturally layered lavas are especially well developed at the contacts between obsidian and coarsely vesicular pumice. It is difficult to identify a uniquely primary layering structure because multiple generations of flow layers develop as folds become isoclinal and hinges are transposed.

Folds

Mesoscopic folds are defined by changes in the shape and orientation of textural flow layers. Single and multilayered folds consist of glassy rhyolite embedded in a matrix of pumice (Figure 46). Folded layers are always less vesicular than the pumiceous medium in which they are buckled. Rheological differences must exist between pumice and obsidian for folds to form. Since major-element compositions of the three textural lava types are uniform within individual flows (Fink, 1982), and crystallinities of fold and

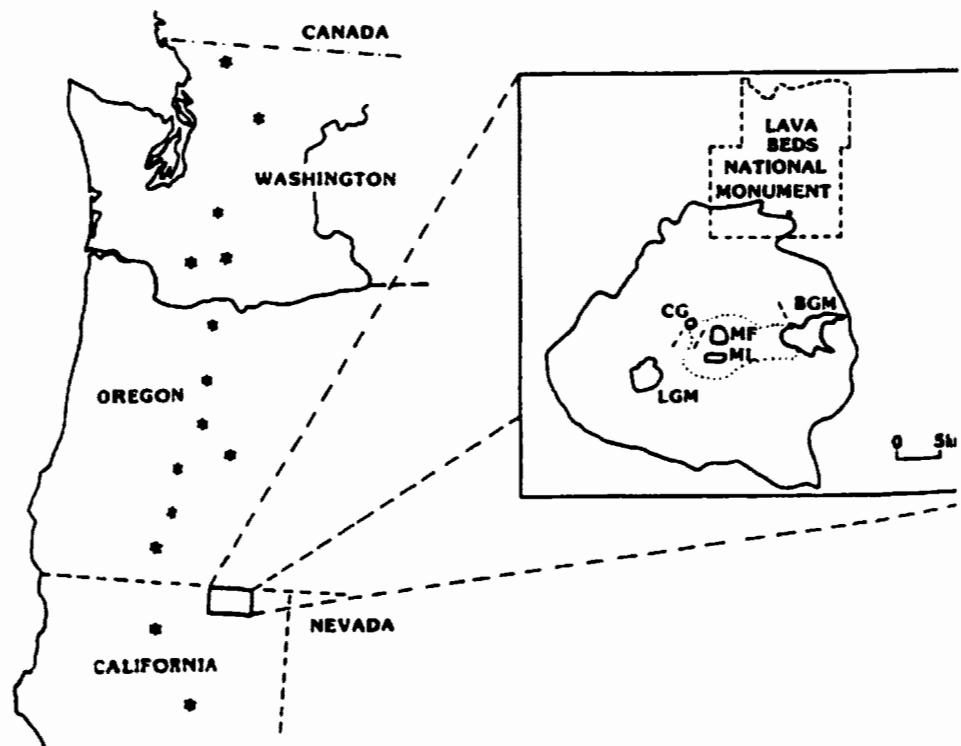


Figure 42. Map showing the location of Little and Big Glass Mountain obsidian flows (LGM and BGM, respectively) on the Medicine Lake Volcano, California.



Figure 43. (a) Upright and (b) recumbent folds in interlayered obsidian and coarsely vesicular pumice at Big Glass Mountain, California.

matrix vary by only a few volume percent, rheological differences must arise because of variations in microlite and/or bubble content. Manga (1998) showed that the small volume fraction of microlites in obsidian (~ 0.01) has a negligible effect on flow viscosity. For this reason, it appears that bubbles exert an important influence on the effective viscosity of silicic lavas and are responsible for rheological variations that lead to the development of folds.

Boudinage

Boudinage and pinch-and-swell structures are common in layered silicic lavas. Boudinage, in contrast to folds, forms in response to layer parallel extension. As is the case for folded layers, boudinaged layers are always less vesicular than the pumiceous medium in which they are deformed. Figure 47 shows an example of boudinage from Panum dome, CA. In this structure, a dense glassy rhyolite layer, enveloped in finely vesicular pumice ($\phi \cong 40\%$), underwent layer-parallel extension, and fractured as a result of extreme stretching. It appears that finely vesicular lava subsequently flowed into the void. Subtle necking of boudinaged layer is recognized as evidence of pinch-and-swell prior to fracture. Given that crystallinities do not vary significantly between the boudinaged and matrix lava, the manner of deformation, and hence, rheologic variations, appear again to be primarily a function of vesicularity differences.

Buckle Folding

In this section I describe two types of small-scale folds in obsidian flows, single-layer and multilayer buckle folds, and I discuss mechanisms for their formation. Next, I analyze single-layer buckle folds using Newtonian and power-law buckling theories (e.g.,



Figure 44. Oblique view of mesoscopic deformation features in poorly vesicular rhyolite (white bands) and finely vesicular pumice (grey lava) at Panum Dome, eastern California. Hat is 20 centimeters long.

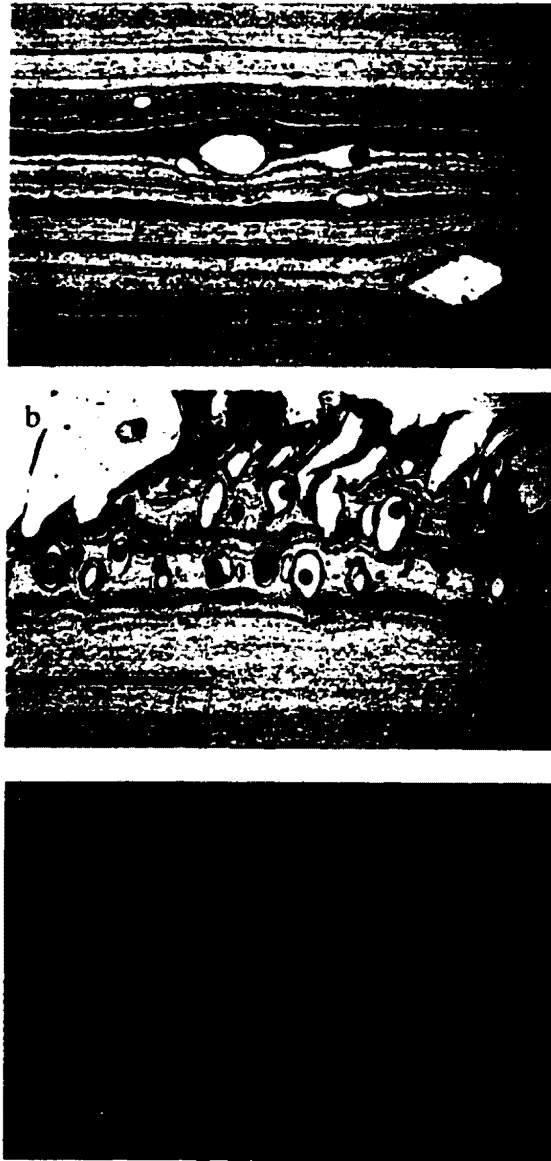


Figure 45. Three types of flow layering in obsidian lavas. (a) Microlite defined flow layers (scale bar=1mm). Microlites are approximately 30 μm in length. Note disruption of microlite flow layering due to formation of large vesicle. (b) Pumiceous layering in coarsely vesicular pumice defined by planar layers of vesicles (scale bar=3mm). (c) Isoclinally-folded textural layering consisting of alternating obsidian (black) and vesicular layers (light grey). Scale bar is 8 centimeters long.

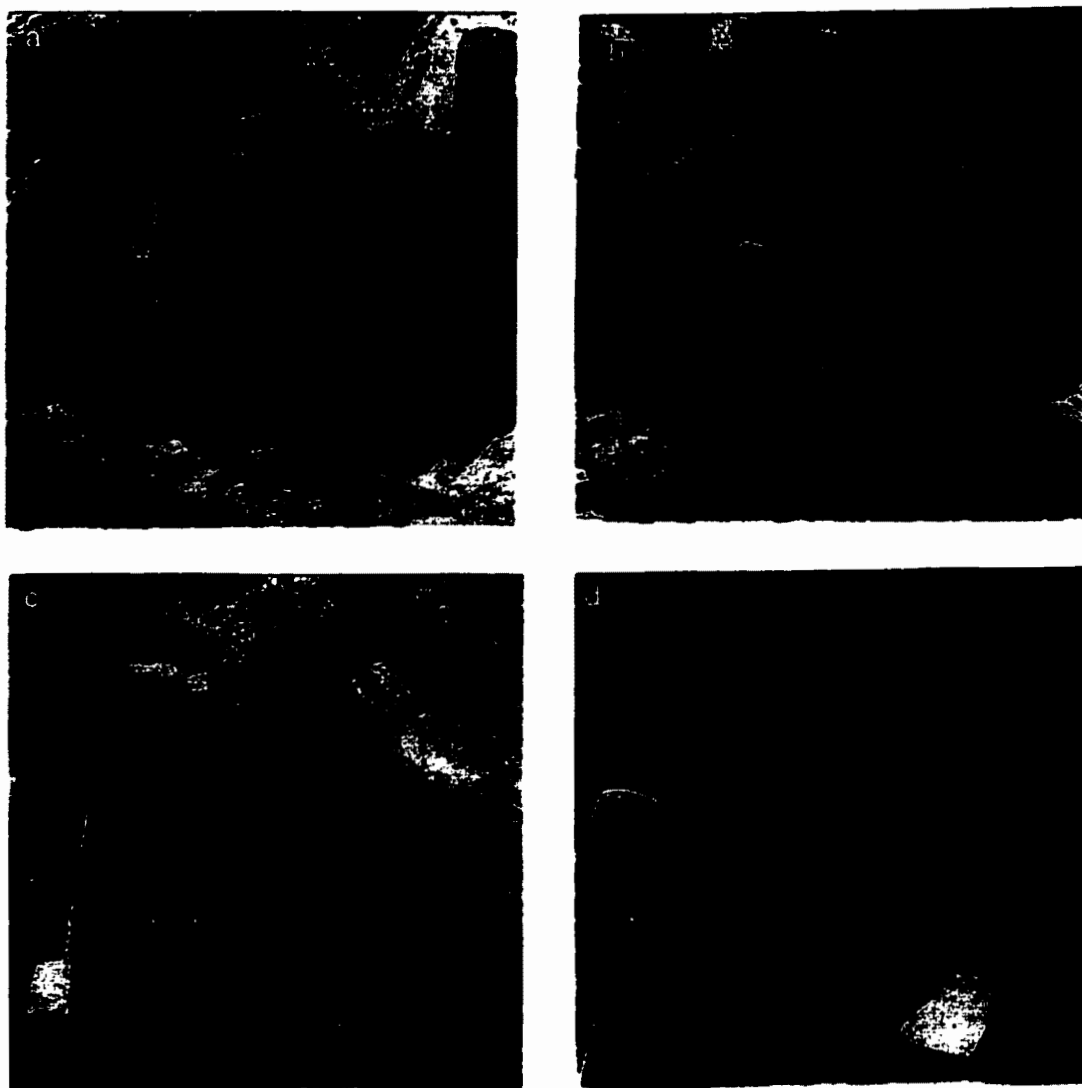


Figure 46. Single and multi-layered glassy folds in coarse pumice: (a) multilayered harmonic, (b) recumbent single-layer isoclinal, (c) intrafolial buckle fold, and (d) polyharmonic folds. Pumice vesicularity is approximately 50%. All exposures are vertical.

Biot, 1961; Smith, 1979) as a means of estimating the shear viscosity ratio of bubble-poor and bubble-rich rhyolite.

Mesoscopic folds commonly form in contact zones between obsidian and coarse pumice, and as parasitic features on larger antiforms (Figure 48). All folds form by deflection of one or more planar obsidian layers due to some component of layer-parallel compression. Orientations of fold axes are highly variable on the scale of the entire lava flow, but commonly trend parallel to larger-scale folds. The folds discussed here are minor folds (wavelengths less than 100 meters) whose geometries are assumed to develop independently of the influence of gravity (e.g. Johnson and Fletcher, 1994).

Such structures can be further classified as buckle folds. In the process of buckle folding, mechanical layering, an alternating arrangement of strong and weak layers, plays an active role in controlling the stress and strain distribution within the layer (e.g. Groshong, 1975). In obsidian flows, mechanical layers are composed of lavas of different vesicularities, for example obsidian and pumice. Evidence that folded obsidian layers are indeed formed by buckling includes: (1) discontinuous deformation across boundaries between pumiceous lava and folded obsidian layers (Figure 49), suggesting significant mechanical differences across layer boundaries, and thus ruling out passive folding; (2) single-layer folds are a part of semi-regular wave trains (Ramberg, 1963); and (3) the repeated nature of buckles, which rules out the possibility that folds developed by a transverse bend mechanism (e.g. Groshong, 1975).

Multilayer folds are composed of obsidian layers separated by coarsely vesicular pumice. The thickness of pumiceous material between glassy layers varies from approximately 0.1 to 10 centimeters. The relative thicknesses of pumice and obsidian (pumice/obsidian= N) governs the style of folding. For small values of N , harmonic folds develop. Harmonically folded layers show a correspondence of wavelength and symmetry in all layers (Figure 50a). With increasing N , and hence sufficiently large separation

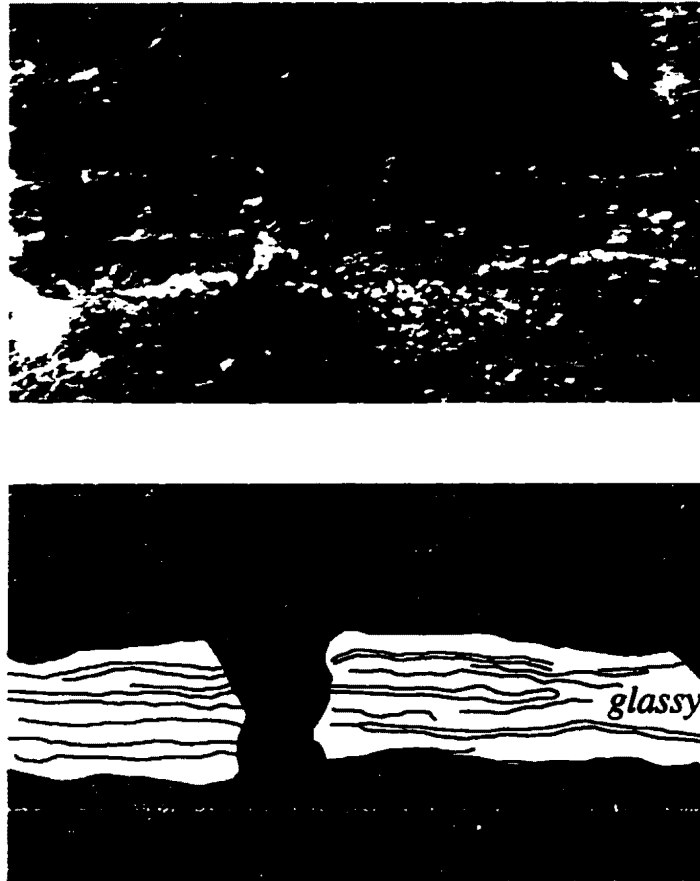


Figure 47. Boudinage of glassy rhyolite within finely vesicular pumice. (a) Field photograph of vertical exposure of boudinage. (b) Tracing of boudinage. Porosity of boudins is <10% while the porosity of the pumice is approximately 40%. Minor necking of boudinaged layer in the far right and left portions of the photograph may indicate pinch-and-swell disturbances.

between layers, the obsidian layers buckle independently of one another and develop their own characteristic wavelength. Under these conditions, disharmonic and single-layer buckle folds develop (Figure 50b, c). Figure 51 shows the average matrix thickness versus average folded-layer thickness for folds from Big Glass Mountain, CA. The style of multilayer folds depends on the amount of interlayer pumice, which in turn, implies that lava viscosity is a strong function of bubble content. To address the influence of bubbles on viscosity, I investigate single-layer buckle folds.

Single-layer buckle folds are less common than multilayered fold assemblages, yet occur in the same parts of the flow. Many folds are sinusoidal, and obsidian layers are surrounded by a zone of contact strain in which bubbles are flattened in the fold cores and stretched in the outer arcs of folds (Figure 52). These folds are typically composed of glassy and poorly vesicular rhyolite 0.1-3 centimeters thick, buckled within a pumiceous matrix. The vesicularity of the pumice varies from approximately 40 to 85%, with much of the variation attributable to local flattening and extension in and around fold hinges. The overall pygmatic geometry of these folds suggests large viscosity contrasts between the folded-layer and surrounding matrix (e.g. Ramberg, 1960).

Fold Analysis

Buckling instabilities arise as a result of contrasts in the strengths of the materials under applied stress (e.g. Smith, 1977). The folds analyzed here are formed during magmatic flow, and hence the rheologic contrasts governing their formation may be viewed as viscosity contrasts. Since structures in obsidian lavas are defined by layered variations in vesicularity, the viscosity contrasts that accompany fold development are most plausibly explained by variations in the bubble content of the melt. Unfortunately there are no direct

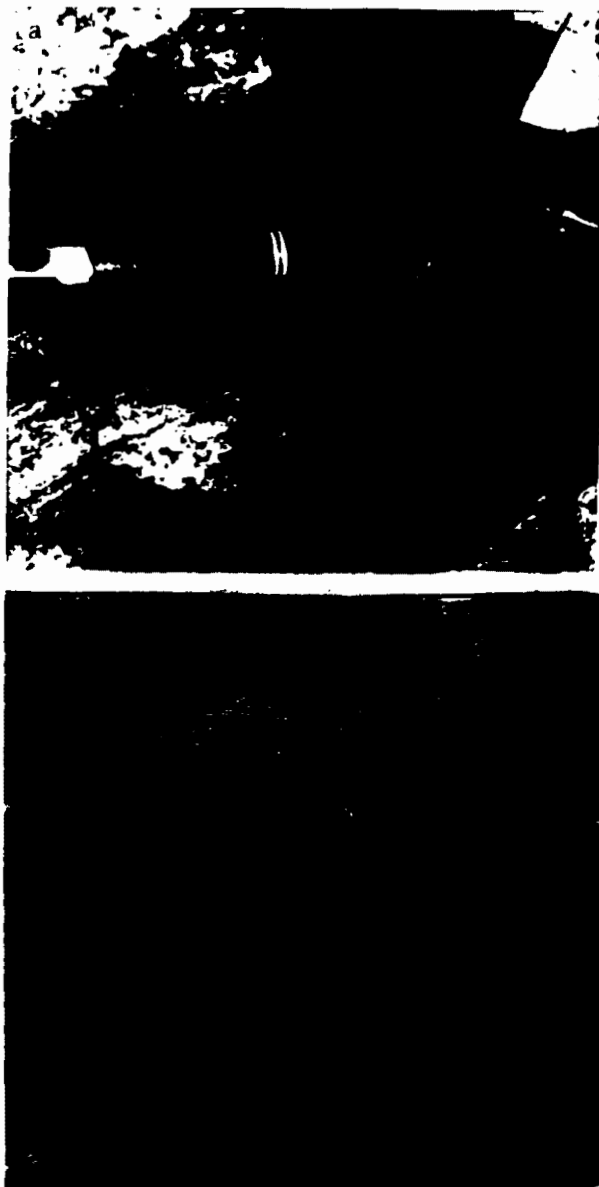


Figure 48. Parastic glassy folds in coarse pumice. (a) Vertical exposure of flexural-slip folds on the limb of larger antiform (larger than field of view). (b) Inclined view of an intrafolial buckle fold.



2 mm

Figure 49. Photomicrograph of pumice (left) in contact with a folded obsidian layer (right). Strain is localized in the pumiceous lava. Note the deformed vesicles. Scale bar is approximately 3 millimeters long.

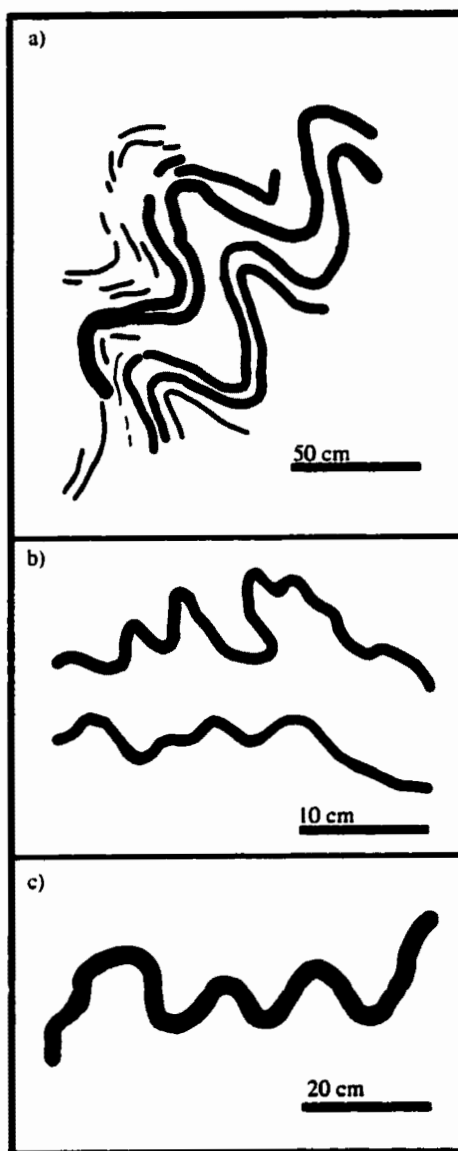


Figure 50. Tracings of glassy folds ranging from (a) multilayered harmonic, (b) disharmonic, to (c) single-layer ptygmatic. The folding style varies with amount of interlayer pumice and competent layer thickness.

rheological measurements of vesicular rhyolitic lavas. However, geometric relations of folds in texturally layered obsidian lavas preserve information regarding the magnitude of the viscosity differences between obsidian and pumice. Below I investigate how wavelength-to-thickness ratios of buckle folds vary, and how such variations may reflect the relative rheologic properties of obsidian and pumice when compared to theoretically predicted wavelength-to-thickness ratios.

Methods of Measurement

In this analysis I seek to relate fold geometry to the relative rheologic and textural characteristics of the fold and matrix. I begin by presenting measurements of four parameters that define the geometry and texture of fold assemblages: arc wavelength (w), layer thickness (T), shortening strain (ϵ), and matrix density (ρ). The arc wavelength is the distance measured perpendicular to fold hinge lines along the center of the folded layer between two successive crests or troughs (Figure 53). The layer thickness is measured normal to both the folded-layer/matrix interface and the inferred fold axis. Fold wavelength and thickness measurements are used to compute the normalized wavelength (= arc wavelength/thickness) which, in turn, is used to calculate the shear viscosity ratio. Percent shortening was computed by comparing the original length of the folded layer, measured along the centerline of a wave or wavetrain, and the final length of the fold assemblage, measured as the straight-line distance between the ends of fold trains.

The density of the pumiceous matrix is used to calculate porosity (ϕ). Dry bulk density of matrix pumice was determined using Archimedes principle (e.g. Houghton et al., 1988) on samples sawn from fold assemblages. Since pumiceous specimens contain large and irregular vesicles, samples were wrapped in wax film of known volume to prevent infilling of voids with water. Density was determined by weighing wax-coated

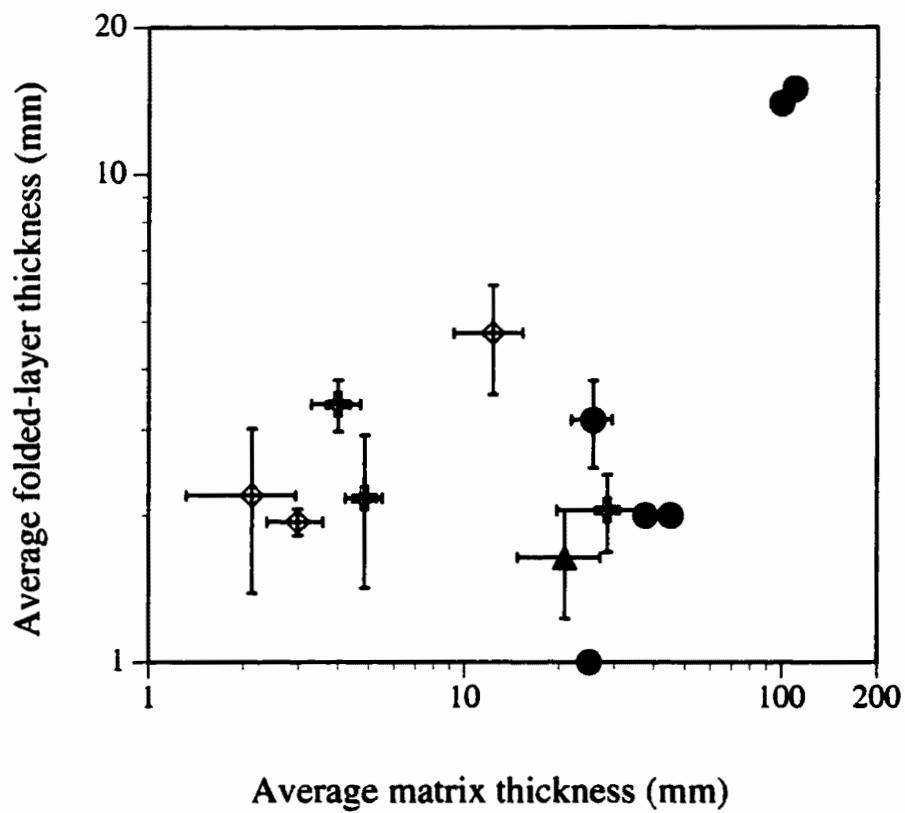


Figure 51. Phase diagram of multilayered and single layer folds from Big Glass Mountain. Open symbols represent multilayer harmonic (\diamond) and polyharmonic folds (\square). Solid symbols represent disharmonic (\blacktriangle) and single-layer folds (\bullet).

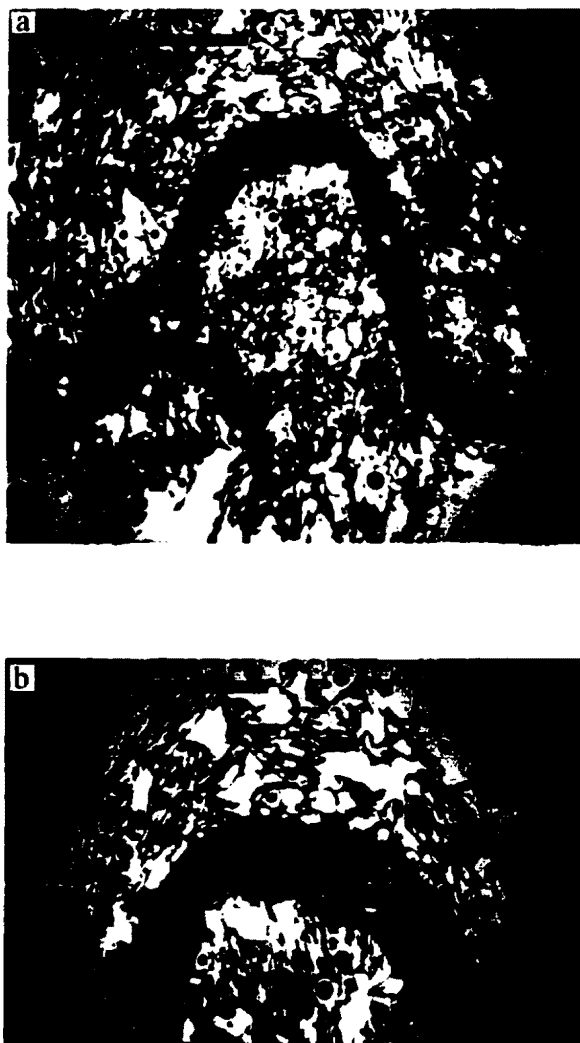


Figure 52. (a) Photomicrograph of a single-layer obsidian buckle fold and its pumiceous matrix showing contact strain within the pumice. Scale bar represents 1.5 centimeters. (b) Close up of deformation in the inner and outer arc regions of the fold. Scale bar represents 0.5 centimeters.

pumice samples and using the formula:

$$\text{density } (\rho) = \frac{\text{dry wt.}}{\text{dry wt.} - \text{wax wt.} + \text{wet wt.}}$$

where wax wt. is the wet weight of the wax sheet used to wrap pumice. Matrix densities were determined for 30 samples, each collected from within a 1-5 cm thick envelope around measured fold perimeters. Porosity was determined from the bulk density, assuming a glass density of 2.19 g/cm³.

Criteria for fold selection included: (1) assemblages consist of one glassy fold embedded in 2-halfspaces of pumice (i.e., no free surfaces); (2) folds exhibit plane strain, as deformation parallel to fold axes appeared to be negligible; (3) folds are not vesicular; (4) folds are symmetrical.

Folding of Newtonian fluids

Folding theories (e.g. Biot, 1961; Ramberg, 1960) can be used to predict the most stable fold wavelength that will grow under conditions of layer-parallel compression and plane strain for specific shear viscosity differences and layer thicknesses. Buckling theory developed by Biot (1961) states that for every fixed layer-matrix shear viscosity ratio, a dominant initial wavelength develops in response to layer-parallel compression. For a Newtonian fluid of shear viscosity μ_l embedded in a medium of shear viscosity μ_m , the wavelength of folding (Wd), layer thickness (T), and shear viscosity ratio (μ_l/μ_m) are related by:

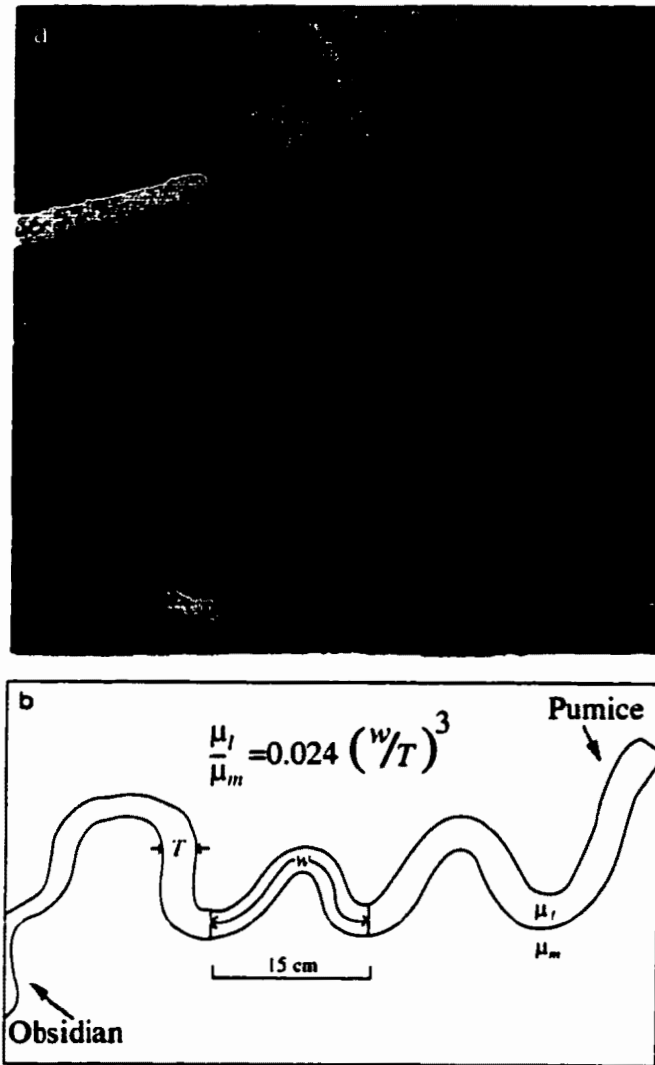


Figure 53. (a) Vertical exposure of a folded obsidian-layer in coarsely vesicular pumice from Big Glass Mountain, California. (b) Trace of the fold showing thickness, T , and arc wavelength, w , of the folded layer. μ_l and μ_m are viscosity coefficients of the folded obsidian layer and the pumiceous matrix, respectively. Measurements of wavelength and thickness from this sample indicate that the shear viscosity ratio (μ_l/μ_m) is $\cong 3$.

$$W_d = 2\pi T \left(\frac{\mu_l}{6\mu_m} \right)^{1/3} \quad (1)$$

(e.g. Biot, 1961; Ramberg, 1960). Note that the dominant wavelength is an increasing function of layer thickness and shear viscosity ratio (μ_l/μ_m). By rearranging Eq. 1, I obtain an expression for the shear viscosity ratio:

$$\frac{\mu_l}{\mu_m} = 0.024 \left(\frac{w}{T} \right)^3. \quad (2)$$

According to Biot's theory, the arc wavelength (w), as measured through the center of the fold, is assumed to be the dominant initial wavelength that formed at the onset of deformation. However, pre-buckling shortening may lead to modifications of the initial wavelength and therefore introduce error. To address these effects I analyzed the interfaces between folded-layer and matrix and inspected flow bands internal to the folded layers. Most of the folds analyzed have smoothly curving microlitic flow bands and have non-undulating contacts with the matrix. By contrast, folds that have undergone a finite amount of pre-buckling shortening could be identified by cusped-lobate interfaces between the matrix and the fold. Only folds not affected by pre-buckling shortening are included in this analysis.

Results

Table 6 contains measured and computed parameters for dense glassy folds from Big and Little Glass Mountains, Medicine Lake Volcano, CA. Most folds underwent

approximately 50% shortening. Because many folds are parts of wavetrains consisting of several fold arc segments, the values of arc wavelength and layer thickness for each segment are averaged. Although wavelengths and thicknesses vary considerably, average normalized wavelengths vary between 8.0 and 26.4. Matrix vesicularity is also variable (~35-80%), as localized zones of extension and flattening develop in close proximity to a fold (e.g. Figure 52).

Arc wavelengths and thicknesses of 73 glassy folds from Big and Little Glass Mountains, and Obsidian Dome, California are presented in Figure 54. Folds show a general increase in arc wavelength with increasing layer thickness. Wavelength and thickness vary by more than two orders of magnitude. The higher-frequency variation in wavelength observed for folds of constant layer thickness (1-5 cm) is interpreted to be a consequence of changes in the shear viscosity ratio. While this trend is consistent with their formation by a buckling mechanism (e.g. Ramsay and Huber, 1987), the power law relationship (Eq. 2) reflects an added influence of the shear viscosity ratio on the dominant wavelength.

Figure 55 shows the frequency distribution of normalized wavelengths (w/T) for glassy folds from Medicine Lake and Obsidian Dome, CA. The preferred normalized wavelength (mode) is approximately 9.5. Folds exhibiting large normalized wavelengths ($w/T > 9.5$) are interpreted to have buckled under large shear viscosity ratios compared to fold assemblages with smaller normalized wavelengths ($w/T < 9.5$). Very few folds have wavelengths of less than 6. The preferred normalized wavelength suggests approximately uniform shear viscosity ratios for most of the fold assemblages. Table 7 shows obsidian-pumiceous rhyolite shear viscosity ratios calculated using Eq. (1). Values are based on the arc wavelength and folded-layer thickness data presented in Table 6. The estimates indicate that the obsidian shear viscosity (μ_l) may be up to two orders of magnitude greater than pumice shear viscosity (μ_m). These calculations include two critical assumptions of

Newtonian buckling theory: that both media are Newtonian fluids, and the materials maintain constant volume throughout deformation. As these constraints are largely not met in bubble-bearing lava flows, absolute magnitudes of the shear viscosity ratio inferred from normalized wavelengths are not entirely accurate. However, these results indicate that, in contrast to the conventional view of the effect of bubbles on lava viscosity (e.g. Sibree, 1933; Jaupart and Allegre, 1991), bubbly rhyolitic lava can be less viscous than bubble-poor lava.

Discussion

Rheological information is recorded in mesoscopic folds in both their geometries and in the textural differences between folded layers and matrix materials. Newtonian buckling theory (e.g. Biot, 1961) assumes that both materials behave as linear viscous fluids. At low strain rates ($<10^{-3}\text{s}^{-1}$) bubble-free rhyolitic melt may be Newtonian (Webb and Dingwell, 1990). However, bubble-bearing lavas are non-Newtonian (e.g. Stein and Spera, 1992), and suspensions of bubbles may be shear-thinning when bubble deformation is large (Manga et al., 1998). Indeed, the presence of pinch-and-swell structures in obsidian flows may be additional evidence that flow was non-Newtonian (e.g. Smith, 1975, 1977; Emerman and Turcotte, 1984). An obsidian layer buckled in pumice may represent an assemblage in which the folded layer (obsidian) behaves as a Newtonian fluid while the matrix (pumice) behaves as a non-Newtonian fluid. A theoretical framework concerning such a rheologic configuration is presented by Smith (1979).

Figure 56 shows curves of normalized wavelength versus shear viscosity ratio predicted for fluids with both Newtonian and power law rheologies (Smith, 1979; 1977). The average normalized wavelengths of 17 glassy buckle folds from Big Glass Mountain are shown for: (A) Newtonian folds embedded in a shear-thinning medium, (B) Newtonian fold-matrix pairs, and (C) shear-thinning folds in a shear-thinning matrix.

TABLE 6. Measured and computed parameters on obsidian folds from Big and Little Glass Mountains, CA.

Sample^a	Thickness(cm)^b	Wavelength(cm)	Normalized Wavelength	% Shortening(ϵ_x)	Matrix Porosity
SBG-1	0.46	4.8	10.4	42.2	47.4
SBG-3	1.1	22.1	20.1	55.0	50.0
SBG-55	0.78	7.6	9.7	51.4	67.0
SBG-41a	0.44	5.1	11.6	41.0	74.2
SBG-41b	0.11	2.9	26.4	47.0	74.2
SBG-69	1.3	16.3	12.5	54.0	N.A.^c

TABLE 6. Continued.

Sample ^a	Thickness(cm) ^b	Wavelength(cm)	Normalized Wavelength	% Shortening(ϵ_x)	Matrix Porosity
SBG-59	0.37	4.0	10.8	37.0	N.A. ^c
SBG-40	0.32	5.3	14.3	NA	80.6
BGM-1	0.3	6.1	20.3	8.0	66.0
LGM-9a	1.52	20.0	13.2	60.5	35.5
LGM-9b	4.5	49.0	10.9	32.5	52.2
LGM-11	3.0	39.0	13.0	46.7	65.6
LGM-13	20.0	160	8.0	17.6	51.4

^a SBG samples are from distal locations of the southern lobe of Big Glass Mountain while the LGM samples are from the northern perimeter of the north east lobe of Little Glass Mountain.

^b Average layer thickness based on approximately 10 measurements

^c Folding analysis based on photographs

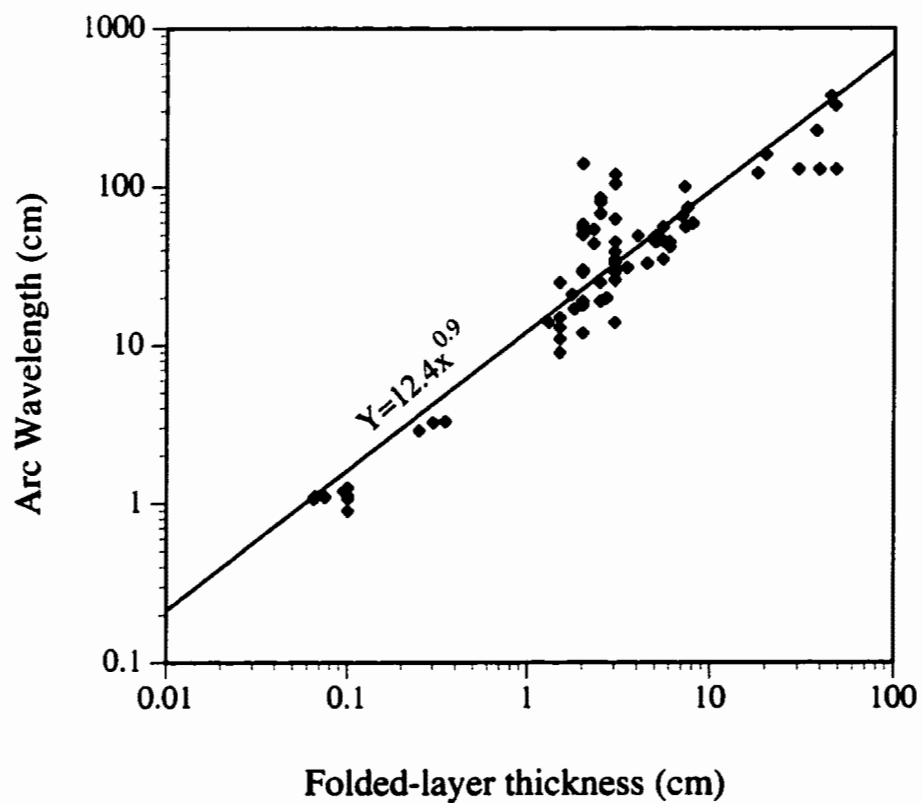


Figure 54. Plot of dominant wavelength versus competent layer thickness for 73 folds from Big and Little Glass Mountains, CA. Curve-fit was determined using the linear least-squares method.

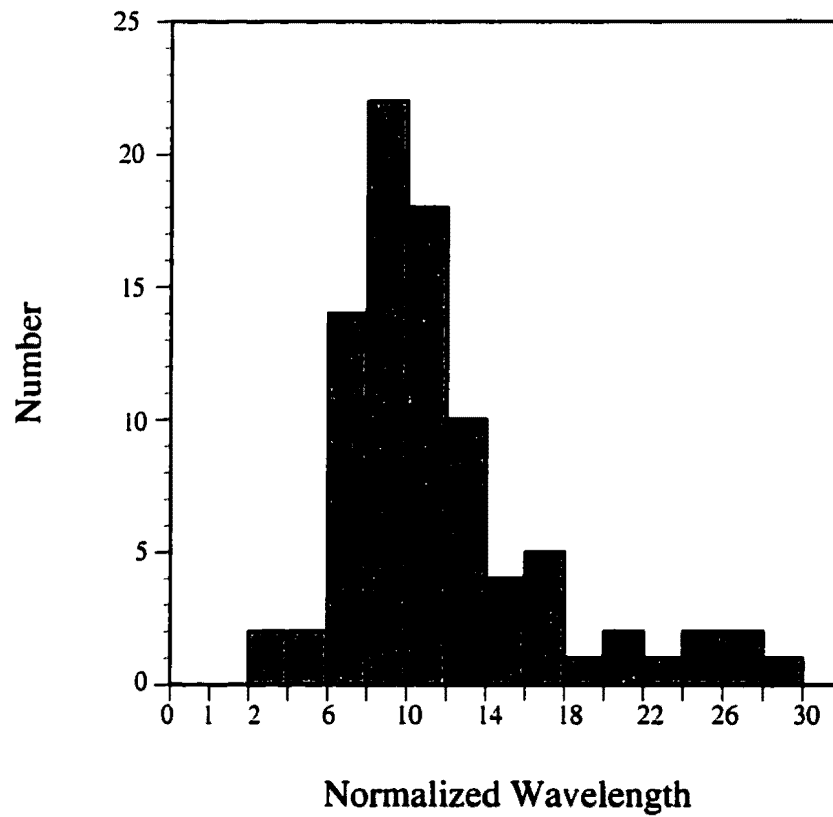


Figure 55. Distribution of normalized wavelength (w/T) of folds from Big and Little Glass Mountains, and Obsidian Dome, CA.

These folds were chosen because they are completely devoid of vesicles (end-member obsidian) and formed under plane strain conditions. Error bars provide the standard deviations of the normalized wavelengths, which, in turn, provide a range in shear viscosity ratio according to the various model curves. In the context of Newtonian theory, the variance in normalized wavelength corresponds to a range in shear viscosity ratio of ~7 to 55. Comparable Newtonian folds of the observed average normalized wavelength buckled in a shear-thinning matrix would be produced over a range in shear viscosity ratio of ~1.5 to 11. A shear-thinning fold buckled in a shear-thinning matrix would correspond to a range in shear viscosity ratio of ~45-300 (e.g., curve C, Figure 56). At least qualitatively, then, shear-thinning behavior accentuates the viscosity contrast between obsidian and pumice, and leads to the formation of a larger wavelength than would be produced in Newtonian media. If the rheology of pumiceous rhyolite is characterized by power law behavior, estimates of shear viscosity ratio based on Biot's buckling theory may be high by up to a factor of 10.

Figure 57 shows the shear viscosity ratio of glassy fold assemblages from Big and Little Glass Mountains (curve A; Figure 56) plotted versus matrix vesicularity. The highly variable nature of matrix vesicularity renders a diffuse correlation between shear viscosity ratio and bubble content. However, the general increase in shear viscosity ratio with increasing matrix porosity is consistent with experimental results (solid line; Figure 57) from Bagdassarov and Dingwell (1992). While estimates of viscosity ratio based on non-Newtonian rheology do not correspond directly with those found experimentally by Bagdassarov and Dingwell (1992), most of the samples plot within one order of magnitude of their shear viscosity estimates.

Given that no direct measurements of the viscosity of rhyolitic lavas are available, and experimentally determined viscosities of bubbly rhyolitic melts are scarce (Bagdassarov and Dingwell, 1992), testing rheological inferences based on comparisons of measured and

TABLE 7. Shear viscosity ratios of folded obsidian layers and pumiceous matrices from Big and Little Glass Mountains, CA. Viscosity ratio estimates are based on measured wavelength to thickness ratios and theory described by Biot (1961).

Sample ^a	Shear Viscosity Ratio (μ/μ_m)	Matrix Porosity
SBG-1	28	47.4
SBG-3	200	50.0
SBG-55	22	67.0
SBG-41a	33	74.2
SBG-41b	500	74.2
SBG-69	50	N.A. ^b
SBG-59	33	N.A. ^b
SBG-40	100	80.6
BGM-1	200	66.0
LGM-9a	50	35.5
LGM-9b	33	52.2
LGM-11	50	65.6
LGM-13	12.5	51.4

^a SBG and BGM samples are from distal locations of the southern lobe of Big Glass Mountain while the LGM samples are from the northern perimeter of the north east lobe of Little Glass Mountain.

^b Folding analysis based on photographs.

theoretically predicted fold wavelengths is difficult to impossible. While I would be overly optimistic to assume that precise values of shear viscosity ratio may be obtained by the applications of Biot (1961) and Smith (1979) folding theories, bubbly rhyolite appears at least qualitatively to be less viscous than bubble-free rhyolite. This result may explain the common occurrences of boudinage and pinch-and-swell structures in layered silicic lavas (Figure 47).

Conclusions

Analysis of intermediate-scale buckle folds yields insights into both the deformation mechanisms and the relative rheologic properties of texturally diverse rhyolitic lavas. Buckle fold style is determined by the relative spacing of obsidian layers and intervening pumice. This follows from the fact that obsidian layers can translate past one another along planes of less viscous pumiceous lava. Hence, flexural-slip folding appears to be the dominant mode of deformation in shortened, texturally layered lavas. Single-layer buckle folds and boudinage may be used as qualitative indicators of the relative shear viscosities of bubble-poor and bubbly silicic lavas. However, accurately quantifying shear viscosity ratios from the geometries of these structures is not straightforward.

The rheological evidence offered by mesoscopic structures, while qualitative, is relevant to placing better constraints on the formation and structural evolution of obsidian flows. Folded and boudinaged layers in obsidian flows are always less vesicular than the surrounding pumiceous matrix, an observation that indicates that bubble-poor lava behaves less viscously than bubbly lava. If obsidian flows are indeed stratified with respect to vesicularity (see Figure 1), the rheologic properties of the flow must also vary in a compatible manner and therefore, the structural evolution of the flow should be strongly dependent on the location and timing of formation of zones of bubble-rich lava. Such large scale differences in rheology may be an important influence in the development of

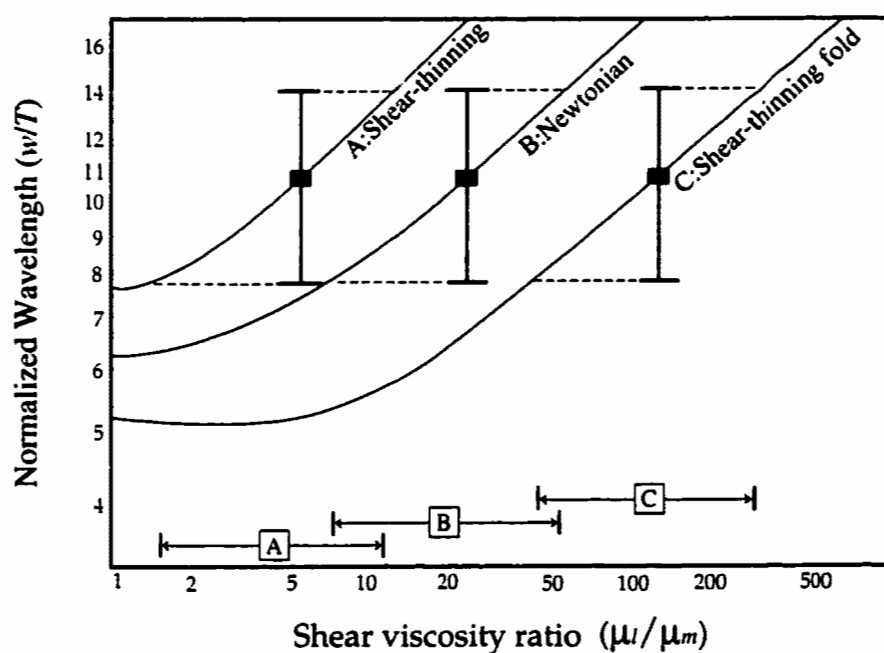


Figure 56. Normalized wavelength (w/T) plotted against the shear viscosity ratio (μ_l/μ_m) for Newtonian folds buckled in: (A) strongly shear-thinning matrix with power law exponent of 20 and (B) Newtonian matrix. Curve (C) is based on folding of a shear-thinning layer in a shear-thinning matrix whose power law exponents are both 5. For large viscosity ratios the normalized wavelength of folds increase as $(\mu_l/\mu_m)^{1/3}$ in agreement with classical buckling theory (e.g. Biot, 1961). Error bars represent the standard deviation of average normalized wavelengths of folds from Big Glass Mountain. The upper and lower bounds in normalized wavelength define a range (shown by arrows) in predicted viscosity ratio for the different rheological models. Plot is adapted from Smith (1979).

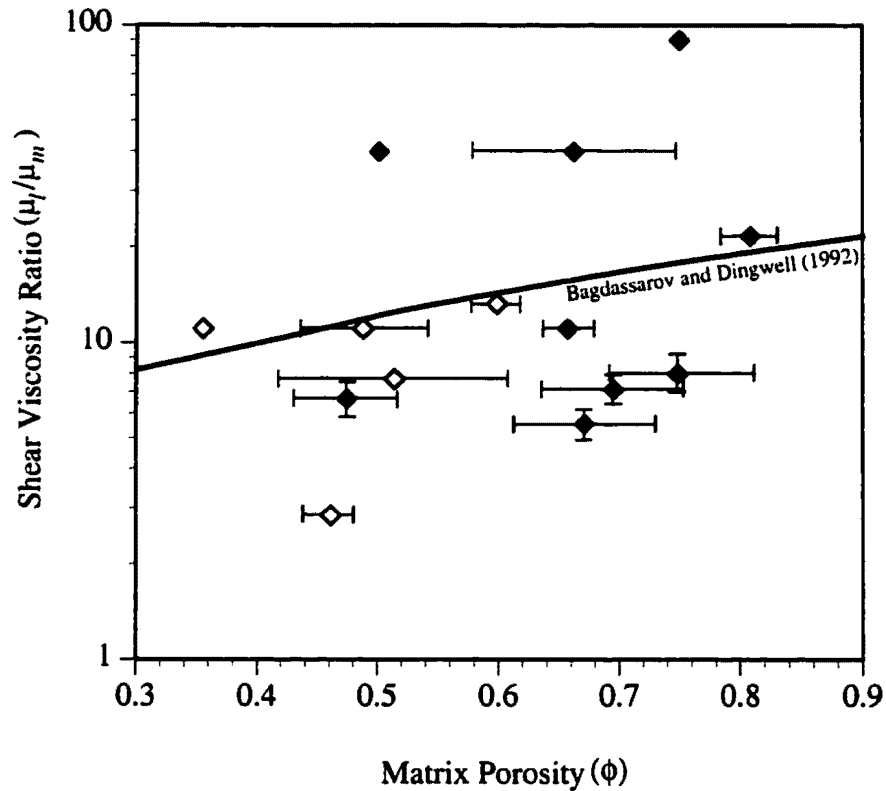


Figure 57. Relative viscosity versus matrix porosity (vesicularity) for glassy folds from Big Glass Mountain (solid symbols) and Little Glass Mountain (open symbols), CA. Error bars represent the standard deviation in average porosity and relative viscosity. Points without error bars represent single wavelength and porosity measurements. Relative viscosities were determined graphically using curve (A) from Figure 56 and therefore represent estimates based on folding of a Newtonian layer within a strongly shear-thinning matrix. Solid curve represents the best-fit to experimental data of Bagdassarov and Dingwell (1992).

structures such as flow ridges (e.g. Figure 43; chapter IV) and cavity structures (Jensen, 1993).

CHAPTER IV

STRUCTURAL RELATIONS OF LARGE CAVITY STRUCTURES IN THE BIG OBSIDIAN FLOW, NEWBERRY VOLCANO, OR

Introduction

In this chapter I present measurements of structures found in "giant gas bubbles" in the Big Obsidian Flow at Newberry Volcano, Oregon. The primary goal of this study was to place structural constraints on the formation of large gas cavities and relate their occurrence to the formation of ubiquitous explosion pits in the Big Obsidian Flow at Newberry Volcano and the Big Glass Mountain obsidian flow, on Medicine Lake Volcano, CA. This objective was motivated in part, by the need for a better understanding of the hazards associated with silicic dome emplacement, specifically, the formation of late stage explosion pits and the potential for endogenous explosive activity from advancing silicic lava flows (e.g., Fink and Manley, 1989; Fink et al., 1992). A second objective was to integrate structural data gathered from cavities with information offered by larger-scale flow features in order to define links between large scale flow behavior and mesoscopic scale deformation. With such insights, we are able to better describe the physical emplacement mechanisms for obsidian flows.

The lack of directly observed obsidian dome eruptions greatly limits what is known about the formation of gas cavities and explosion pits. Here I present evidence from four well-developed cavities that supports the hypotheses: (1) that deformation related to flow advance plays a key role in their formation and (2) the timing and location of cavity

development is linked to large scale structural features and explosion pit formation. These hypotheses present an alternative explanation to that of Jensen (1993), who suggested that explosion craters on the Big Obsidian Flow formed from explosive venting of "giant gas bubbles" that ascended from the depths of the flow. Jensen (1993) noted that "spherical cavities" located in the bottom of four explosion craters were the remnants of gas bubbles formed as large bodies of coarsely vesicular lava rose and expanded in the shallow levels of the flow. This model is an extension of a model proposed by Fink (1980) and Fink and Manley (1989) stating that diapiric rise of coarsely vesicular pumice generates explosions that form craters. If true, this process would represent a hazard associated with silicic dome emplacement that has not previously been described in recently active dacite domes (e.g., Nakada et al., 1995).

Below I present structural measurements of layering, folding, stretching lineation, and striation exposed on the insides of cavities that do not appear consistent with a simple bubble rise origin for the large cavities. I then provide a kinematic analysis of fold and layering data obtained from the cavities and conclude with a purely structural interpretation of the origin of these features. The implications of this process will then be discussed in the summary.

Geologic Background

Geology of the Big Obsidian Flow

The Big Obsidian Flow erupted approximately 1,300 years ago from the summit caldera of Newberry Volcano (Figure 58; e.g., Jensen, 1993). The eruption began with a phase of explosive activity that deposited pumice and dense lava blocks as large as 1 m within the caldera (MacLeod and Sherrod, 1988). Approximately 0.32 km³ of tephra was erupted and deposited as far east as Idaho (MacLeod et al., 1982). Eruptions of pyroclastic

flows into Paulina Lake preceded a final stage of effusive activity in which the 0.13 km³ Big Obsidian Flow was emplaced (MacLeod and Sherrod, 1988). The Big Obsidian Flow is about 1.8 km long and locally thicker than 20 m (Figure 59; MacLeod and Sherrod, 1988).

Like many Holocene obsidian flows throughout the western U. S., the Big Obsidian Flow consists of four end-member lava types: finely vesicular pumice (FVP), coarsely vesicular pumice (CVP), obsidian (OBS), and vent-facies rhyolite (RHY). Fink (1983) suggested that these textural lava types are arranged in a crude flow-wide stratigraphy that is common to all extensively developed flows (e.g., Figure 4). Based on flow front exposures and textural analyses of drill core samples (e.g., Fink and Manley, 1987), he deduced that obsidian flow stratigraphy consists of a basal breccia, overlain by dense obsidian, then coarsely vesicular pumice, followed by an uppermost obsidian layer which is capped by brecciated finely vesicular pumice flow top. Vent facies rhyolite is restricted to the southernmost extent of the Big Obsidian Flow, where it forms an elevated domal protrusion that marks the vent. The upper 30 meters of the Big Obsidian flow correlates well with this sequence of layers, however basal sections of the flow are obscured by talus.

The surface of the Big Obsidian Flow has numerous regularly spaced arcuate ridges and intervening cusped valleys that were interpreted by Fink (1980) to be folds formed while the lava was in motion (Figure 60). Surface folds indicate that compression was parallel to the flow direction and the viscosity of the surface was greater than the interior viscosity (Fink and Fletcher, 1978). Such viscosity contrasts develop as the surface of the lava cools. Distal flow ridges are composed dominantly of CVP while medial and proximal ridges are composed mostly of FVP.

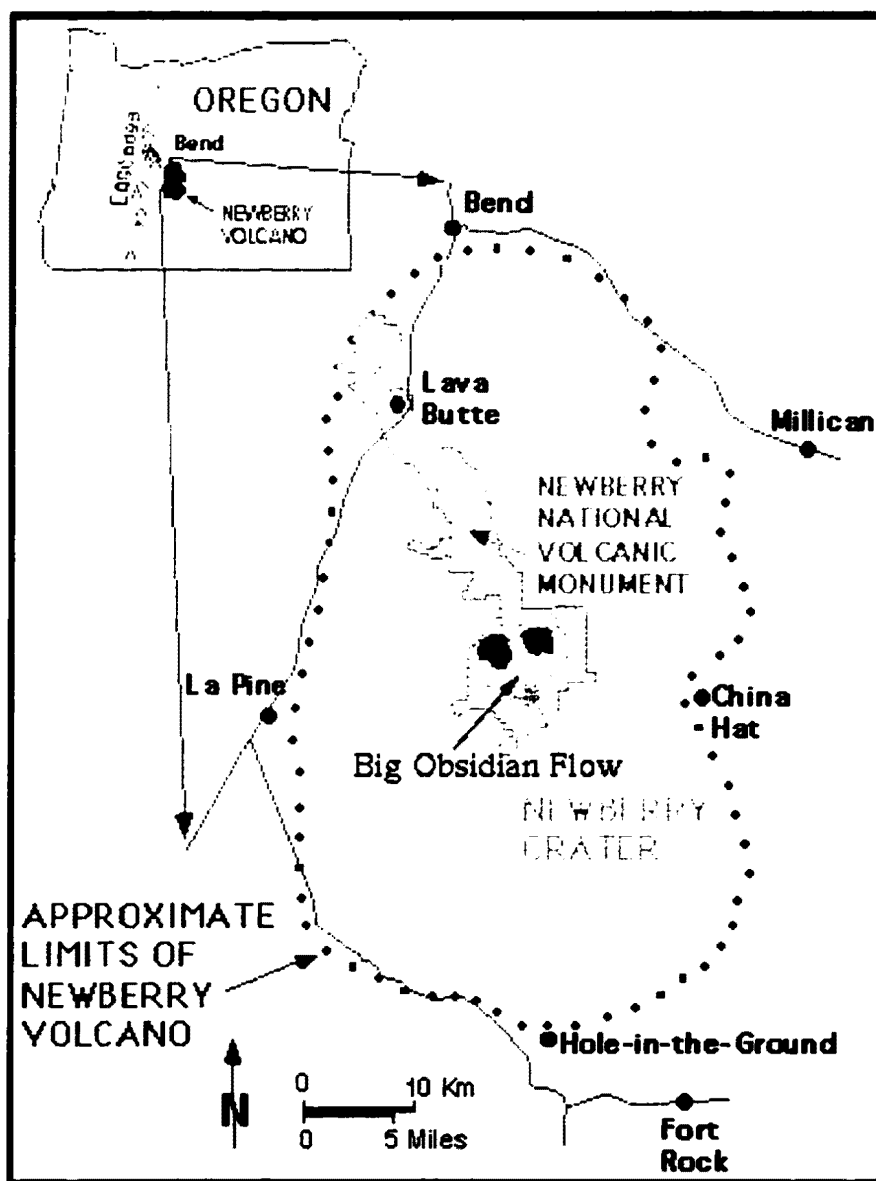


Figure 58. Location of Newberry Volcano and the Big Obsidian Flow. Reproduced from Jensen (1993).

Explosion Pits and Cavity Structures

Explosion craters are conical depressions in the flow surface, 10-25 meters in diameter, extending to depths of 15 meters (Figure 61). Russell (1905) first described these craters as "depressions where the explosions occurred". Cavity structures are large void spaces that typically occur in the bottom of explosion pits (Figure 62). These so-called "giant gas bubbles", hereafter referred to as cavity structures, have not been recognized in other obsidian flows (e.g., Jensen, 1993). Figure 63 shows the locations of explosion pits mapped by Jensen (1993) along with the locations of cavity structures examined in this study. Cavity structures are found in near vent, medial, and distal locations on relatively shallow slopes of the flow. Cavities X, G, and A are located in the bottoms of explosion pits of the same label, while cavity SNJ does not coincide with an explosive crater; rather it is exposed by a large fracture trending approximately east-west. The cavities vary in diameter from 5-15 meters. The morphology of the exposed portions of cavities varies from that of a cylindrical fold to dome-shaped. All cavities are antiformal in cross section (Figure 64). Cavity walls are composed of dense flow banded obsidian ranging in thickness from 0.1-3 meters. Cavities A and SNJ are overlain by coarsely vesicular pumice, while cavities X and G occur in close association with spines and outcrops of obsidian with no coarse pumice preserved over or within their walls.

Methods

We measured structural features exposed in four cavities and electronically surveyed one well developed cavity structure to constrain its three dimensional shape and size. Structural measurements include strike and dip of flow layering, trend and plunge of lineations and striations in the plane of layering, and trend and plunge of fold axes.

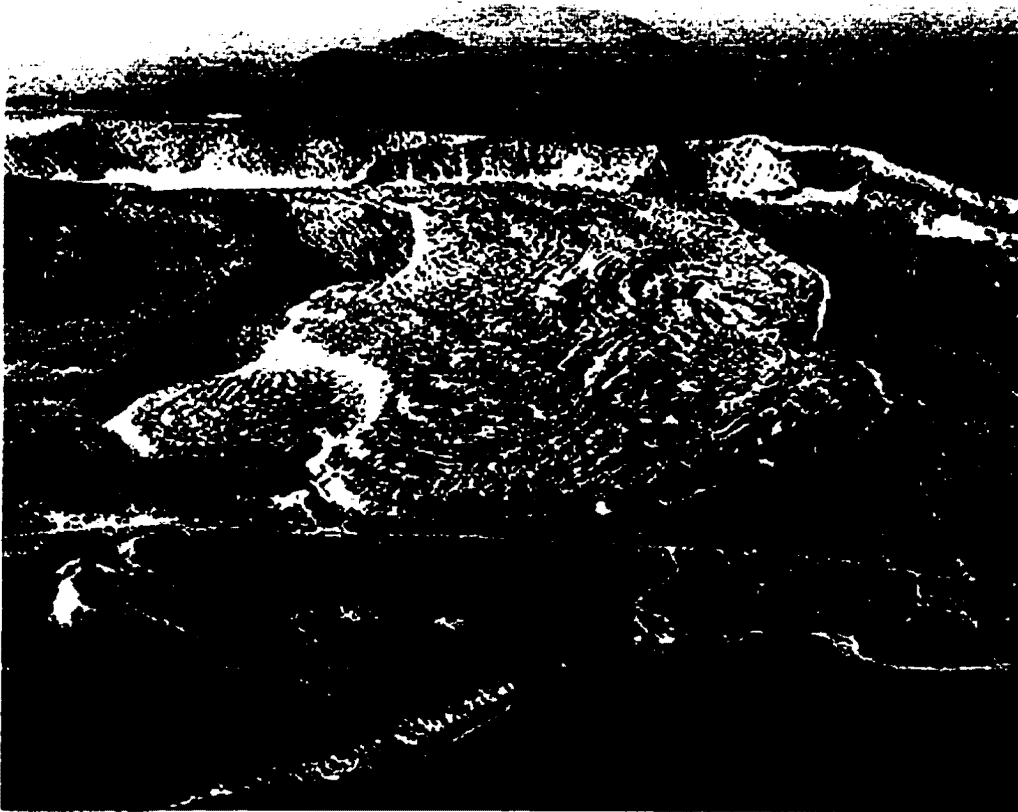


Figure 59. Oblique aerial view of the Big Obsidian Flow, Newberry Volcano, Oregon. View is to the south. (Photograph courtesy of the Oregon Department of Transportation.)

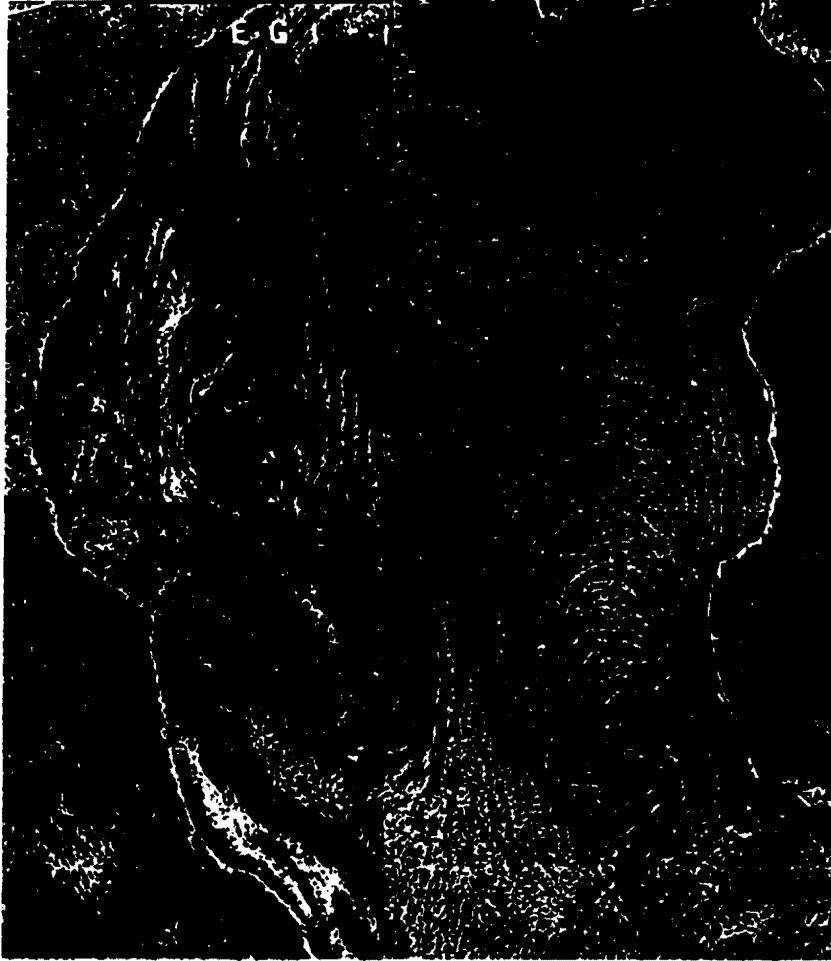


Figure 60. Aerial photograph mosaic of the Big Obsidian Flow showing arcuate flow ridges concave toward the vent. Dark lava is coarsely vesicular pumice while light grey lava is finely vesicular pumice. Flow ridges form perpendicular to the flow direction in response to compression. (Fink and Fletcher, 1978).

Surveying was conducted with a Wild Electronic Distance Measurer (EDM) model TS-1600. The instrument was set up in the center of cavity A at a height of 1.5 meters. Three dimensional coordinates of the cavity walls were measured relative to the instrument in terms of latitude, longitude, and elevation. Data points were collected by first aiming the instrument at a reflector positioned on the wall of the cavity and then activating the laser range finding system. Measurement precision is +/- 1 centimeter.

Results

Structures Preserved in Cavities

Every cavity examined contains preserved in its walls, a combination of the following suite of structures: flow layering, stretched vesicle lineations, mesoscopic folds, chatter marks, and striations (Table 8). These structural elements formed both by dynamic processes in the magmatic state and as a result of plastic deformation. Mesoscopic folds, stretched bubble lineation, and flow layering are interpreted to form during viscous flow while striations and chatter marks form under in plastic and brittle deformation respectively. In this section I describe these mesoscopic structures and discuss the overall morphology of the cavity structures. The orientations of the mesoscopic structures are then discussed.

Flow Layering and Mesoscopic Folds

The inner walls of cavity structures are invariably composed of flow layered obsidian (Figure 65). Flow layering in rhyolitic lavas is defined by subplanar to planar variations in microlite and vesicle abundance. The obsidian is commonly lithophysal and spherulitic, with spherical to ellipsoidal spherulites 1-3 cm in size. In many instances, discrete, finely laminated, glassy plates, 1-20 centimeters thick part from overlying bands (Figure 66) along parting surfaces corresponding to flow layering.



Figure 61. Explosion pit on the surface of the Big Obsidian Flow. Pit is approximately 15 meters in diameter. Cavity Structure A (not visible) is located in the bottom of the crater. Note rim of ejecta shown in the lower right corner of photograph.



Figure 62. Cavity structures (A) G and (B) A. Both features exhibit flow layered obsidian walls. Lineations and striations in cavity G (evident in left center part of the photograph) are subparallel to the main fold axis.

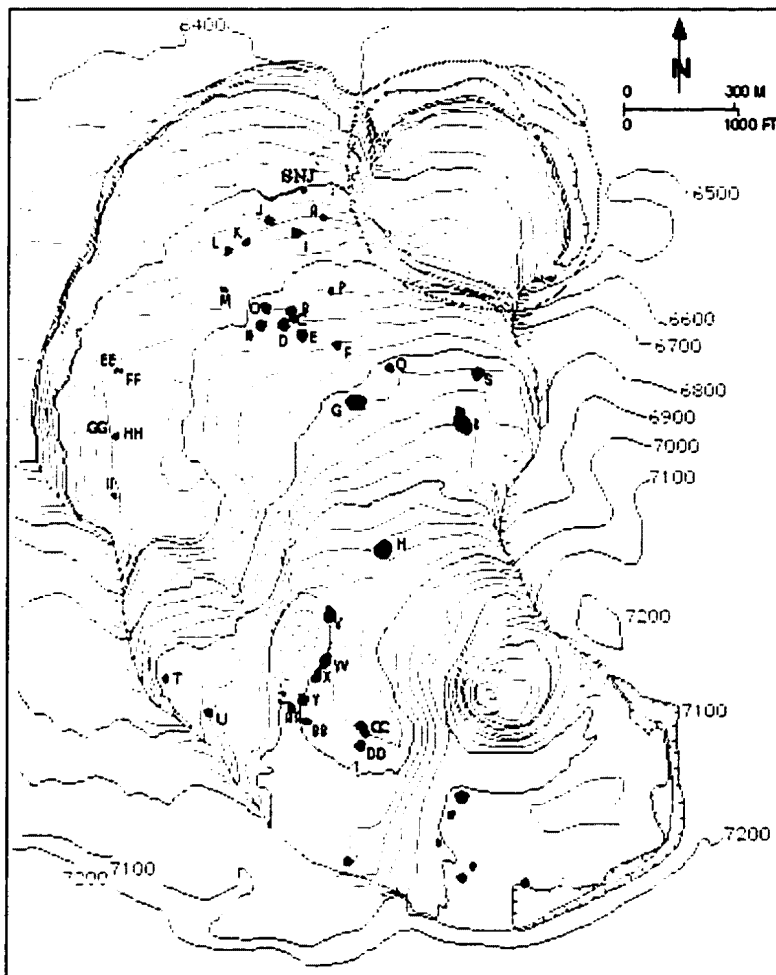


Figure 63. Topographic map of the Big Obsidian Flow showing the locations of several explosion pits mapped by Jensen (1993). Cavity structures X,G, and A occur in explosion pits of the same designation. Cavity structure SNJ is not associated with an explosion pit.

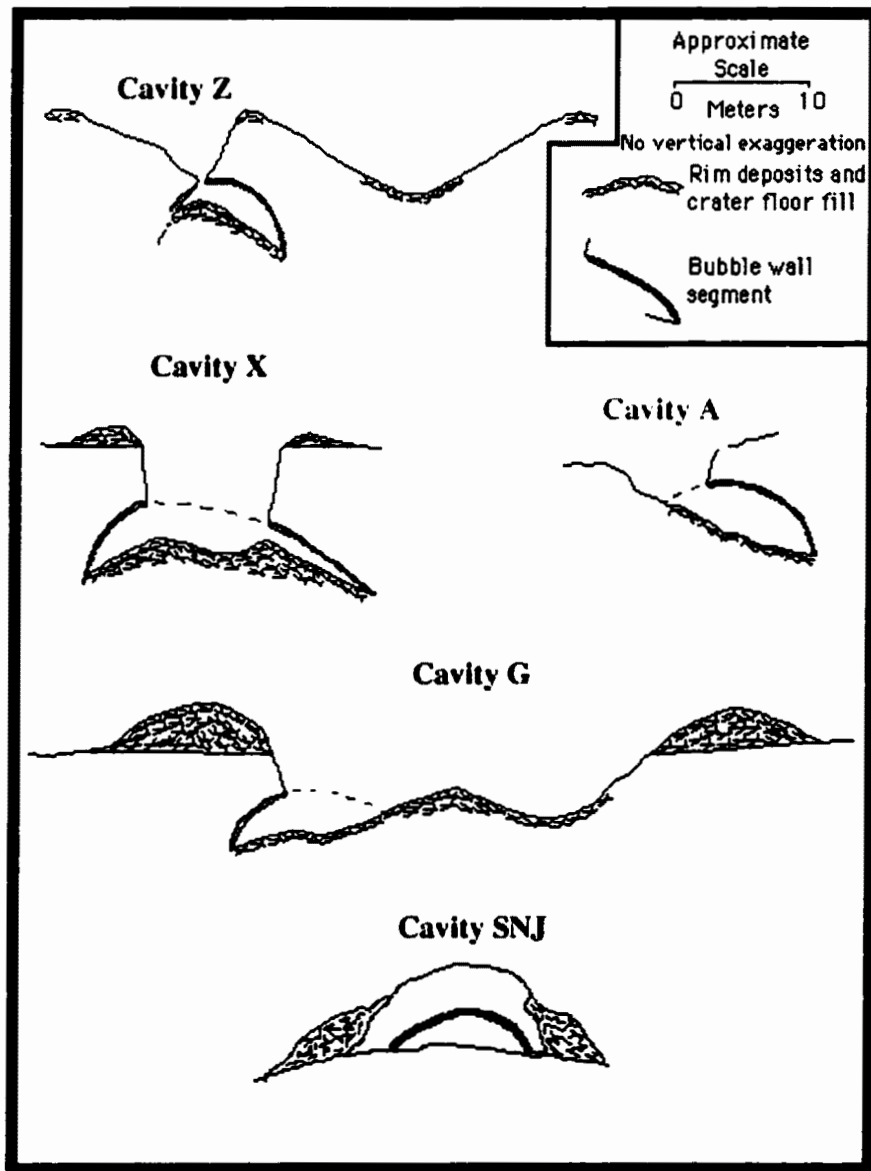


Figure 64. Cavity structure cross sections. Cavities A, G, X, and Z were mapped by Jensen (1993). Cavity SNJ was mapped in this study. All cavities are antiformal in cross section. Adapted from Jensen (1993).

Mesoscopic pull-apart folds (5-20 centimeters in wavelength) are another common structure occurring on the inner walls of cavity structures (Figure 67). These structures typically involve one or more flow layers 1-3 centimeters thick, deformed into an open fold shape where translation appears to have occurred along small "detachments" between flow layers. Displacement along detachment planes is the primary mechanism for the formation of these folds. Translational strain appears to be accommodated by weaknesses between layers. Such weaknesses are occasionally marked by localized vesicular zones between layers (Chapter III).

Linear Structures

Two types of linear structure are present within all cavities: vesicle lineations, consisting of stretched and ruptured vesicles within the plane of flow layering, and striations, or grooves in layering surfaces that range from 2-20 centimeters in length and 1-3 millimeters in width (Figure 68). Vesicle lineations are typically 1-5 centimeters in length and are on average 2-5 millimeters wide. Vesicle long axes are interpreted to form in the stretching direction or the axis of maximum extension (e.g., Manga et al., 1998). Striations are typically only 1-2 millimeters deep and commonly form on layering surfaces parallel to vesicle lineations. Striations are best developed on the innermost surface of cavity A, where they are continuous for lengths of approximately 10-50 centimeters. These structures are interpreted to form by abrasion between flow layers as asperities create grooves on lava surfaces that slide past one another.

Chattermarks

Chattermarks are small cracks preserved in three of the four cavities surveyed. These structures are characterized by subparallel tension cracks, 0.2-1 millimeters wide and

TABLE 8. Mesoscopic structures found in cavities.

Cavity	Flow Layering	Lineation	Folds	Chatter Marks	Striations
A	✓	✓	✓	✓	✓
G	✓		✓	✓	✓
SNJ	✓	✓	✓		
X	✓	✓	✓	✓	✓



Figure 65. Flow layering in obsidian over cavity SNJ.

approximately 0.1-2 millimeters deep. Chattermarks are typically oriented at high angles to striations (Figure 69). While mostly exposed on the inner surfaces of the cavity walls, well developed chatter marks were noted in cavity A beneath spalled off wall material. The consistent orientation of chatter marks with respect to striations suggests that the two structures may have formed under similar stress regimes.

Structural Analysis

Structural features were mapped in four cavity structures on the Big Obsidian Flow to better understand possible kinematic relations between the cavity morphology and mesoscopic deformation features. Figure 70 shows structural data collected from each cavity plotted on lower hemisphere stereographic projections. Stereonets show poles to layering, trend and plunge of mesoscopic fold axes, and trend and plunge of lineations and striations. Lineations and striations are labeled with the same symbol (\diamond) because their directions were parallel to each other in all the cavities examined.

In all exposed cavity segments, poles to layering plot on or near a common great circle known as a π circle. A π circle represents the strike and dip of a plane that is exactly perpendicular to the hingeline of a fold (e.g., Davis, 1989), and thus the pole to a π circle is the expression of the fold axis. Layering in cavities X, G, and SNJ forms a single π circle, each with a single pole. The π circle in cavity X is oriented N67W 78SW and the stereographically deduced fold axis is oriented N23E 12. Flow layers in cavity G form a π circle oriented N32W 46SW and have a fold axis oriented N58E 44. In cavity SNJ, the π -circle strikes N15W and dips 65NE and indicates a fold axis oriented S75W 25.

Poles to flow layering in cavity A plot within three distinct domains that are fit with three unique π circles (Figure 70). Domain 1 contains most of the points, and poles define a π circle that strikes N64E and dips 53NW. Domain 2 contains poles that define a π circle



Figure 66. Platy flow layered obsidian from the roof of cavity G. Note lineations in the plane of flow layering.



Figure 67. Mesoscopic pull-apart fold on the roof of cavity SNJ.

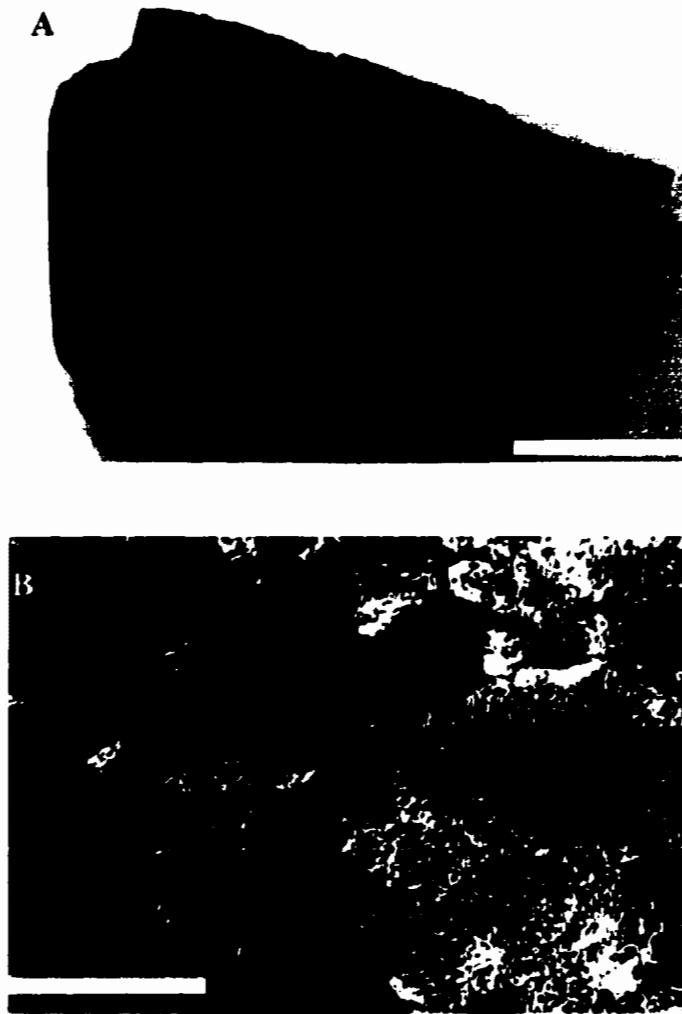


Figure 68. Linear structures on cavity walls. (A) Vesicle lineations. Scale bar is 3 cm. (B) Striations. Scale bar is 5 cm.

oriented N06W 33 NE. The third domain is characterized by a π circle oriented N14W 48SW. Thus no unique fold axis can be deduced from the highly variable layering data in Cavity A; instead, the poles to the π circles indicate multiple fold axes.

Lineations and striations in cavities G and SNJ trend approximately ninety degrees from π circles and correlate well with stereographically deduced fold axes. A preponderance of lineations in cavity A also plot nearly perpendicular to the π circle in domain 1, while lineations in cavity X appear more scattered. The correlation between lineations and fold axes in cavities G, SNJ, and A suggests that lineations and folds formed during the same deformation event. Similarly, mesoscopic fold hinge line orientations in cavities G and SNJ are consistent with poles to π circles and hence are coaxial with large scale folds, again suggesting contemporaneous deformation. In cavities X and A, mesoscopic fold axes do not correlate with either poles to π circles or lineations.

Morphology of Cavity A

Structural analysis of cavities X, G, and SNJ indicate that they have simple geometric fold shapes. Measurements of Cavity A indicate a more complex shape, defined by multiple fold axes. A Digital Elevation Model (DEM) was constructed from detailed topographic measurements to illustrate the three dimensional shape of cavity A (Figure 71), and to gain a better understanding of its deformation history. The cavity has an asymmetrical dome shape with gently sloping southeast walls that become gradually steeper to the southwest and west. The cavity is approximately 11 meters long by 8.5 meters wide. The roof of the structure varies in height from a few centimeters in the southeast corner to approximately 2.5 meters in the northwest portion. The gently sloping southeast walls dip approximately 20 degrees in the up-flow direction while the steeper southwest and west walls dip nearly 90 degrees in the down-flow direction. Lineations and striations are oriented approximately parallel to the long axis of the cavity. Scatter in both layering

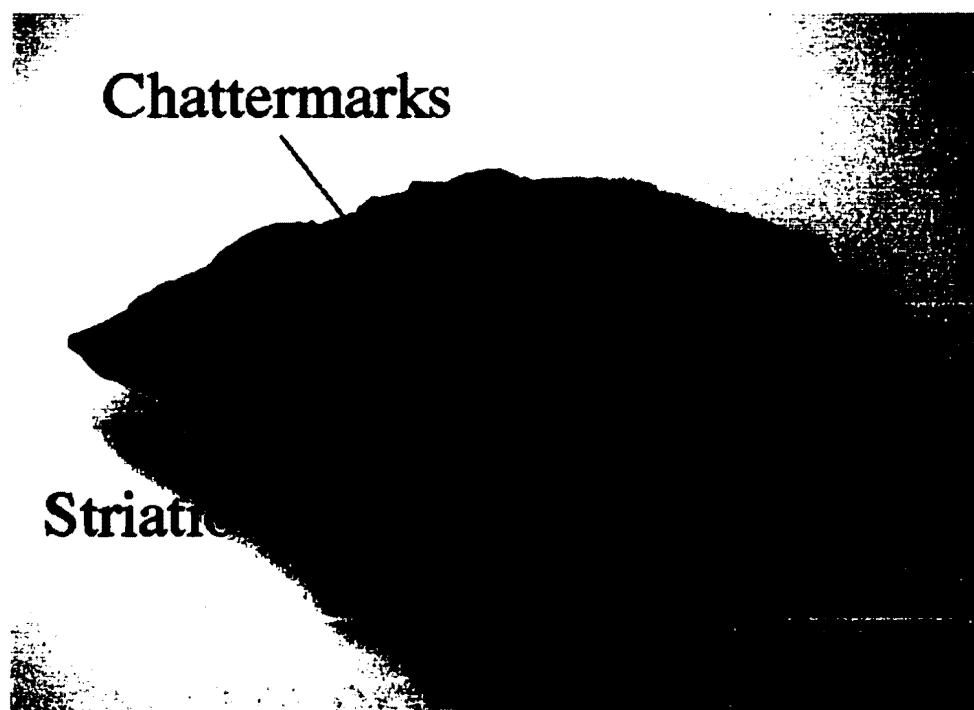


Figure 69. Sample of obsidian from cavity A showing both chattermarks and striations. Chattermarks are oriented approximately normal to striations.

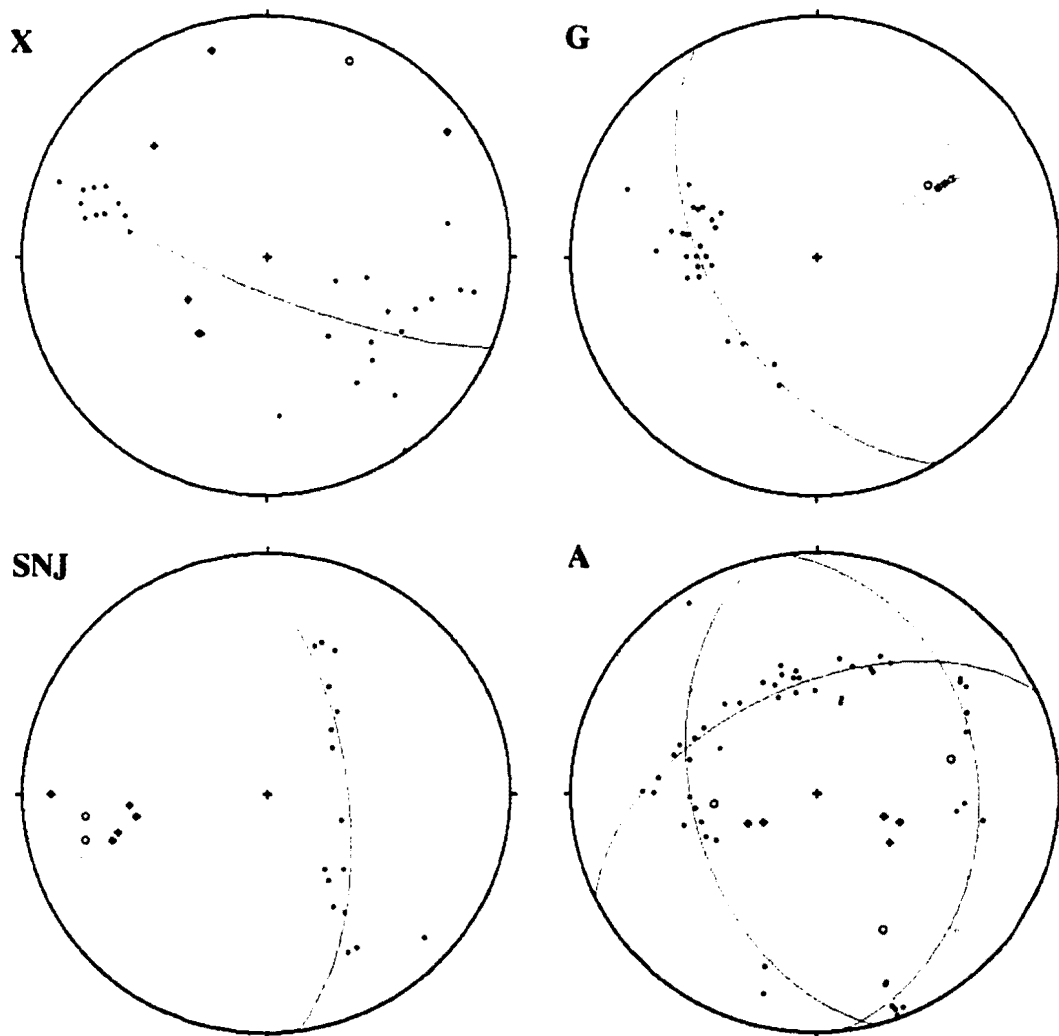


Figure 70. Lower hemisphere stereographic projections of (•) poles to flow layering, (◇) lineations and striations, and (◆) mesoscopic fold axes. Great circles are best fit representations of π circles. Open circles are poles to π circles and represent near cylindrical fold axes.

and lineation and may reflect the asymmetrical domal shape of this cavity, and suggest that it may have formed from multiple folding events.

Discussion

Structural Interpretation of Stereonet Data

The distribution of poles to flow layering in cavities X, G, and SNJ plot consistently on or near great circles, forming π circles. This type of layering distribution indicates that these cavities are near-cylindrical fold structures (Davis, 1989). Flow layering in cavity A is more variable, with poles plotting within three distinct domains, each forming a unique π circle. Poles to these π circles represent three unique fold axes. Thus the macroscopic structure of cavity A is that of a noncylindrical fold or dome (cf. Figure 71). Lineations and striations in cavities G, SNJ, and A plot approximately ninety degrees away from their respective π circles and are therefore coincident with fold axes. Mesoscopic fold orientations in cavities G and SNJ are also parallel to the inferred fold axes. This correspondence in orientation of lineation, striation, and mesoscopic folds with cavity fold axes suggests that the formation of these structural elements occurred contemporaneously under the same stress regimes. This correspondence suggests a possible genetic link between large and small scale structures that will be discussed in the next section.

Cavity A is a complex structure in which poles to flow layering form three distinct domains. The overall morphology of this cavity may be described as a refolded fold, with each domain representing a unique fold axis. At least two folding events are inferred from the orientations of these fold axes. An initial phase of shortening produced the single, near cylindrical fold (F₁) represented by data in stereographic domain 1. A second buckling event superposed at high angles with F₁ produced two later fold axes (F₂) oriented nearly

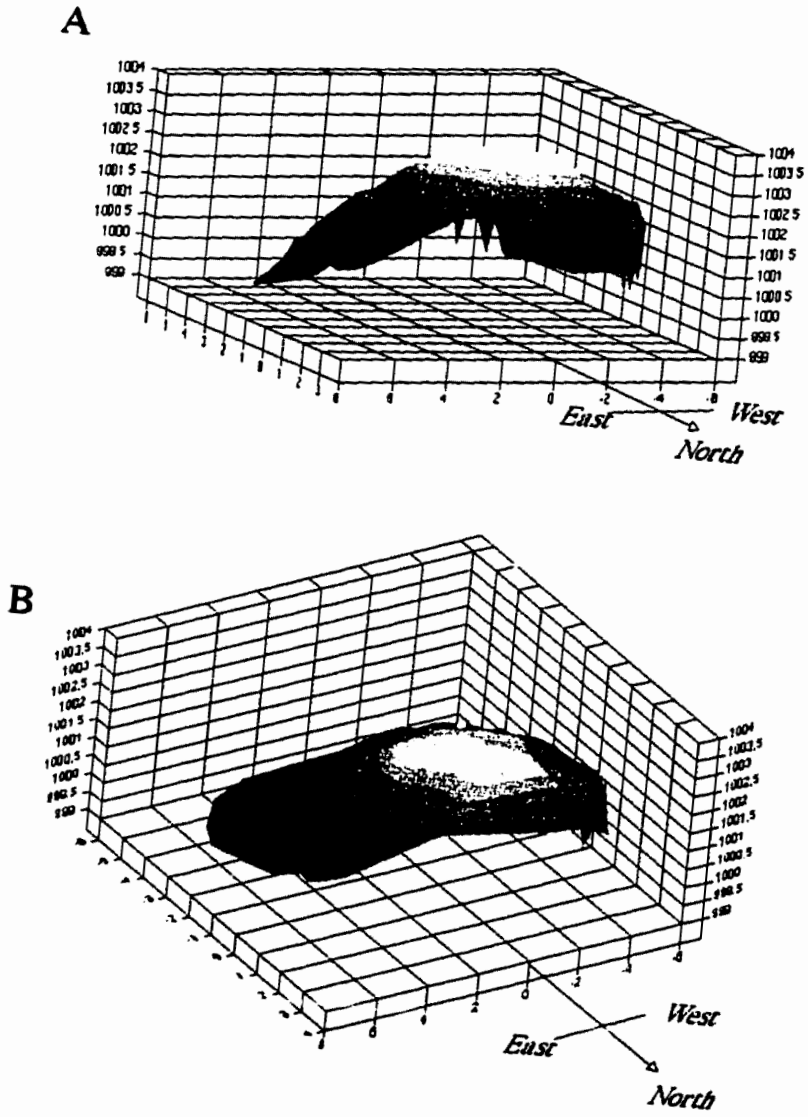


Figure 71. Digital elevation model of cavity A. form is based on 350 topographic measurements. (A) Northeast perspective. (B) Aerial perspective.

ninety degrees to the earlier formed fold (represented by domains 2 and 3; Figure 70). These F₂ folds trend nearly 180 degrees from one another and plunge in opposite directions. Single-layer buckling experiments by Ghosh et al. (1993) show that this sequence of deformation will form relatively open folds and result in structures with domal shapes (Figure 72). Figure 72 shows the resultant deformation of a single layer that experienced two folding events oriented at high angles to one another. The shape of folds produced in this series of deformation is very similar to the measured shape of cavity A.

The early phase of folding (F₁), indicated by domain 1 π circle, was responsible for producing the near cylindrical fold axis oriented S35E. As flow proceeded the fold hinge rotated clockwise to its present position. The other two folds indicated by domain 2 and 3 π circles are nearly 90 degrees to the F₁ fold and may have formed as the cavity structure was translated down flow. The steep down flow wall in cavity A suggests that after initial formation of F₁, the flow continued, rotating the fold into its present position.

Fold Mechanics

Structural relations suggest that cavities form in the upper portions of the flow by a buckle folding mechanism (i.e., shortening of a layer to produce a sinusoidal fold shape). Development of lineations, striations, and mesoscopic folds may be coeval with fold growth as these features are oriented subparallel to the inferred fold axes in cavities A, G, and SNJ. In order to create the void space represented by the cavity, a surface must exist along which considerable slip and layer separation (pull-apart) can occur. Evidence for such a detachment plane is obscured by talus on the floors of all cavities. However, there is abundant evidence in macroscopic and mesoscopic folds to suggest that pull-apart folding is an integral part of cavity formation. Figure 73 shows two examples of pull-apart folds in which a void space was created in their hinge zones. In the first example a deformed series of alternating glassy and pumiceous layers shows a well-developed

mesoscopic cavity structure in the hinge zone of an approximately 2 centimeter wavelength fold. The fold, composed of obsidian, penetrated the upper pumiceous medium as it translated along a basal layer. The basal layer is effectively a detachment surface along which sliding of the overriding layer(s) occurs. The overlying pumiceous medium is both less dense and less viscous than the folded obsidian layer (Chapter III) and thus it provided little resistance to growth of the fold. A larger, structurally similar cavity on the south lobe of Big Glass Mountain, California is shown in Figure 73. This cavity formed in the core of a large upright surface fold that grew as the surface of the flow buckled during flow advance. A basal detachment is inferred based on extrapolation of the fold limbs to the neighboring fold through the adjacent synform.

In the case of both mesoscopic and macroscopic folds, cavities were formed under the following conditions: (1) the upper surface of the fold is unconfined, and (2) folding and layer separation takes place along a basal detachment plane.

Relations to Large Scale Surface Ridges

The hypothesis that cavity structures form by dynamic flow advance processes and not by buoyancy driven deformation (e.g., Jensen, 1993) is supported by the observed alignment of cavity fold axes and lineations with the orientation of compressional flow ridges on surface of the Big Obsidian Flow. Figure 74 shows fold axis vectors for each cavity structure plotted on a topographic map and on an aerial photograph of the Big Obsidian Flow. F₁ and F₂ fold axes in cavity A are shown. The mean flow direction is assumed to be dictated by topography and shown by the orientation of compressional surface ridges. Structure X is located between the vent and a prominent topographic high in a zone where several flow ridges trend approximately N05E. These ridges probably formed as lava flowing from the vent was buttressed to the northwest by a topographically-high lava mound downslope from the vent (e.g., Williams, 1935). Cavity G is located in

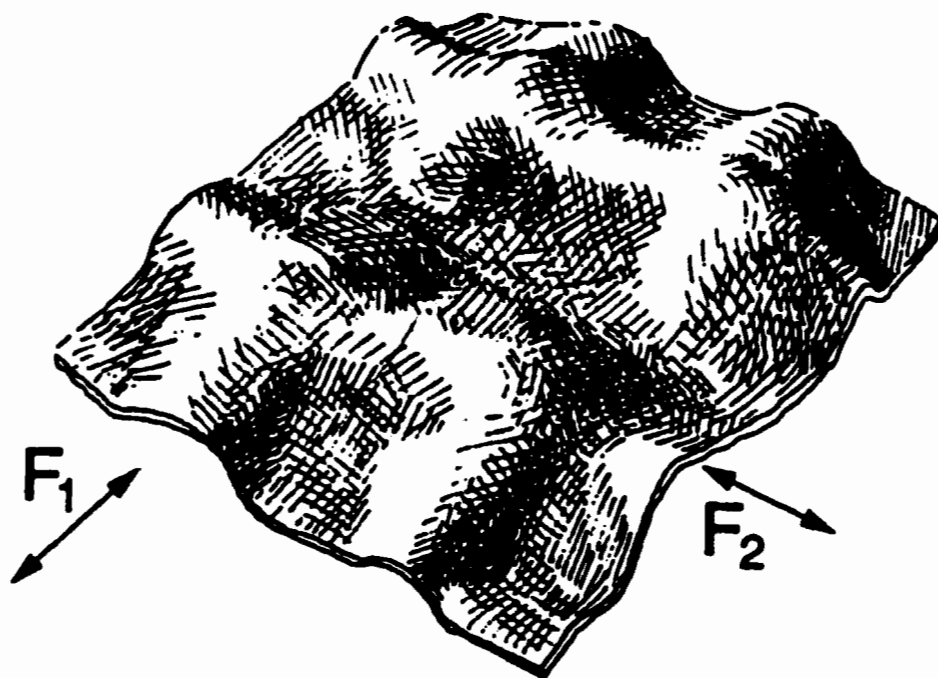


Figure 72. Illustration of a superposed deformation experiment conducted by Ghosh et al. (1993). Domal, noncylindrical folds were produced by shortening early formed folds (F_1) about an axis (F_2) oriented nearly perpendicular to F_1 .

the middle of a flow ridge trending approximately N70E, subparallel to the fold axis indicated by flow layering measurements. Cavity SNJ shows a similar correspondence of fold axis orientation with surface ridge geometry. Cavity A lies within a coarsely vesicular pumice flow ridge trending approximately N35W which is subparallel to the cavities F₁ fold axis. If ridge axes form normal to the flow direction (e.g., Fink, 1980), the agreement between cavity fold geometry flow ridge axes suggests that cavities formed during flow advance as compression ridges grew.

Summary

Analysis of small scale structures in cavities in the Big Obsidian Flow suggests an alternative mechanism for the formation of "giant gas cavities" and lends insight into the deformation mechanisms operating during the effusive stages of obsidian eruptions. Stereographic relations of flow layering, lineation, striation, and mesoscopic fold axes indicate that cavities can be described as near cylindrical and noncylindrical folds. Compatibility between cavity fold axes and large scale compressional flow ridges suggests that cavities form during flow advance as the upper 10-20 meters (i.e., the approximate depth of cavities in explosion pits) of the flow buckles. Pull-apart folding is a plausible mechanism for creating open space during deformation, as cavities are recognized on other scales in rhyolite flows (cf. Figure 73). Figure 75 shows a schematic model of cavity formation by buckling of the upper flow surface. According to this model, folding occurs in response to compression parallel to the flow direction. Compressive stress arises due to interaction between the advancing flow and the talus apron that forms directly in front of the flow; the talus apron offers resistance to the advancing flow. Since the upper surface of the flow is unconfined, it will buckle in response to compression (e.g., Fink and Fletcher, 1978). Continued extrusion of lava will promote growth of surface folds and eventually cavities will form in their hinges. Degassing of volatiles into newly formed cavities will

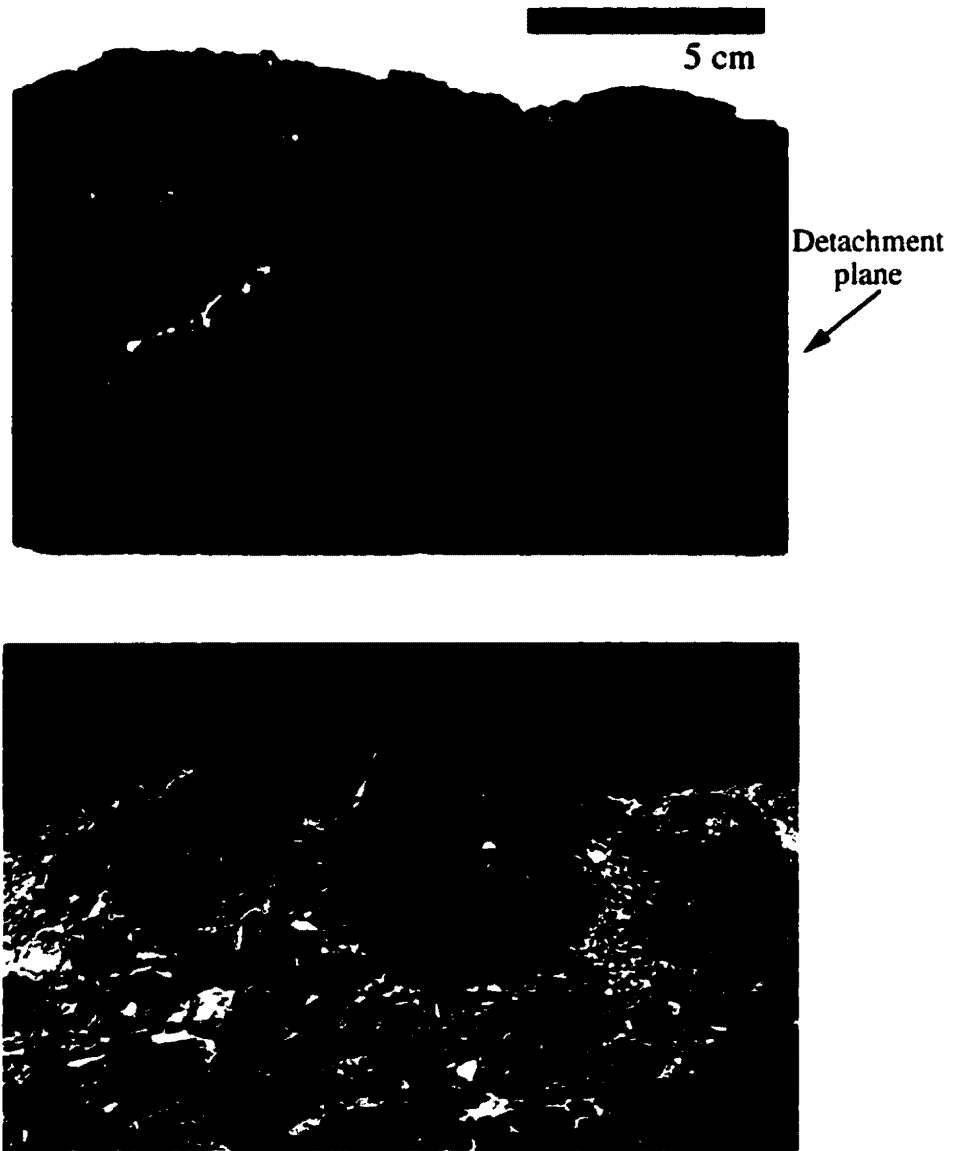


Figure 73. (a) Mesoscopic pull-apart fold in interlayered obsidian and pumice. A small cavity (~2 cm) formed in the hinge of the fold as the folded layer slid along a detachment plane. (b) Buckle folds on the surface of Big Glass Mountain, California. Note ~1.5 meter tall cavity in the hinge zone.

take place until the vapor pressure exceeds the confining pressure, at which time explosion occurs. Judging from the size of many explosion pits on the surface of Big Obsidian Flow, the amount of energy released by such an explosion would be great. The frequency of explosions can be crudely estimated on the basis of two assumptions. First, If we assume explosions took place while the flow was still hot and potentially flowing and also that the emplacement duration was approximately fifty days. Given these assumptions, and that the Big Obsidian Flow contains approximately 50 explosion pits (Jensen, 1993), the average frequency of cavity explosions would be about one per day. Cavities may vent preferentially on the axes of anticlines, where extensional strain is the greatest.

Results from this study support the hypothesis that there is a genetic link between cavity formation and hazardous explosions and crater formation. Explosion pits tend to occur as single large pits (e.g., crater G) or in groups of several smaller pits aligned subparallel to flow ridges (e.g., craters w, x, y; Figure 74). On the Big Glass Mountain obsidian flow at Medicine Lake, explosion pits tend to form lineaments parallel to surface ridges and synformal depressions (Figure 76). Although cavity structures have not been identified in explosion pits on Big Glass Mountain (Jensen, 1993), the spatial correlation between explosion pits and large scale surface ridges may reflect cavity formation along axes of antiformal surface ridges. Cavities on Big Glass Mountain range in size from 10-30 meters in diameter. In the base of several cavities are outcrops of dense obsidian with puzzle-patterned jointing. Rarely is coarsely vesicular pumice exposed in the bottom of explosion pits. There is a paucity of explosion pits on smaller domes and flows. This may reflect both lower volatile contents of smaller eruptions and the lack of structural development of smaller flows. Cavity structures can serve as centers for volatile accumulation during late stages of degassing (e.g., Fink et al., 1992) and ultimately a source of hazardous explosions. Hazards associated with cavity formation have not been

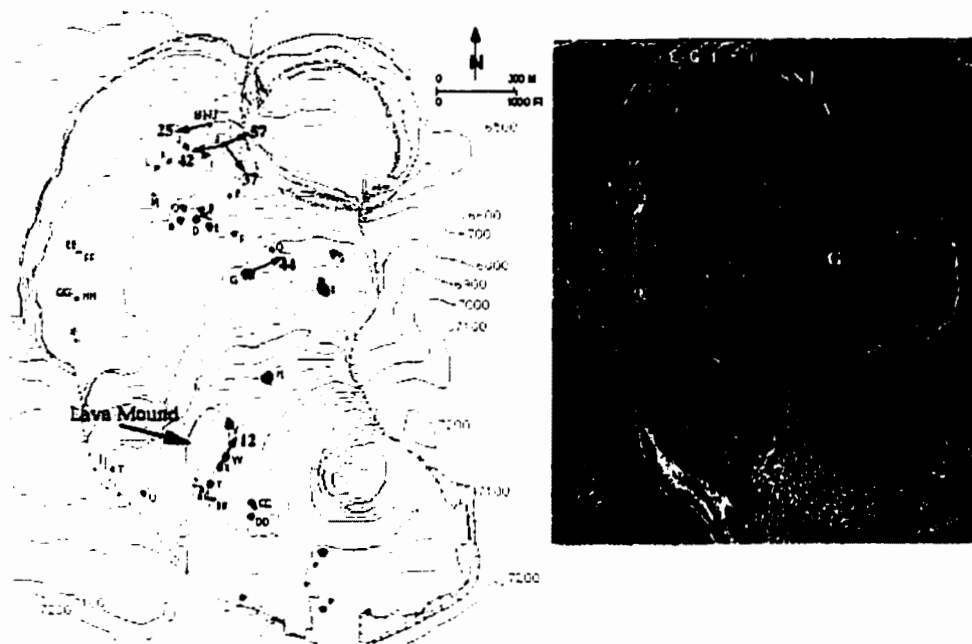


Figure 74. Topographic map and aerial photomosaic of the Big Obsidian Flow showing fold axis orientations (trend and plunge) in cavity structures. Numbers refer to the plunge of cavity fold axes. Letters on aerial photograph mark the approximate locations of cavity structures.

witnessed in recent dacite and andesite dome eruptions (e.g., Unzen, Mount St. Helens, Redoubt, Montserrat).

The goal of this project was to understand the causes of late stage explosive activity on the Big Obsidian Flow at Newberry Volcano, Oregon. While the research presented here does not disprove previous models regarding cavity structure formation, it does contribute to a better understanding of obsidian dome emplacement mechanisms.

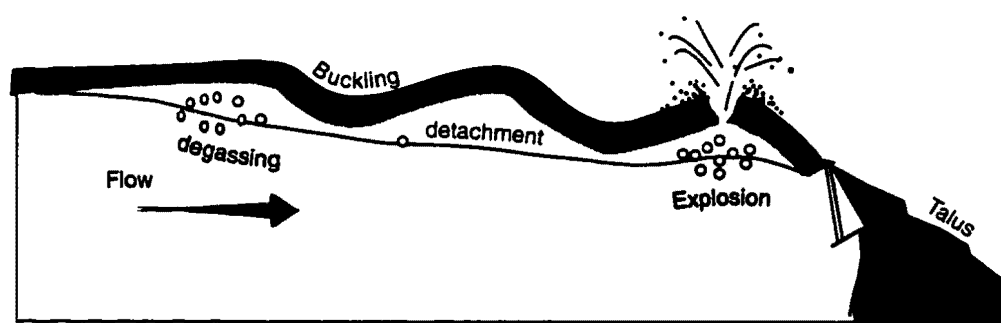


Figure 75. Schematic model of the formation of cavity structures and explosion pits. Arrow indicates flow direction. Buckling of the upper surface occurs as the flow front becomes impeded by the talus apron. Surface folds grow as the flow advances and void space is created in the hinge zones of folds. Volatiles exsolve in the cavity structures and eventually burst to form explosion pits.



Figure 76. Circular and elliptical explosion pits (outlined) on the surface of Big Glass Mountain, CA. Pits are aligned parallel to synformal depressions (black lines) and antiformal ridges.

CHAPTER V

SUMMARY AND CONCLUSIONS

The studies presented in this dissertation provide quantitative textural and structural constraints on processes responsible for obsidian dome emplacement. The fundamental volcanologic contributions of this work are: (1) order of magnitude estimates of Obsidian Dome strain rates (10^{-6} s^{-1}) and effusion rates ($10^6 \text{ m}^3 \text{ day}^{-1}$), (2) qualitative and quantitative constraints on the relative viscosities of bubbly and bubble-free rhyolitic melts, and (3) insight into large scale deformation mechanisms and associated syn- and post-emplacement explosive hazards. Existing models for obsidian dome eruptions (e.g., Fink et al., 1992; Eichelberger et al., 1986) do not incorporate structural data into their interpretations of emplacement mechanisms, despite ubiquitous evidence of flow on all scales. However, textural-stratigraphic evidence (Manley and Fink, 1987) and corresponding water content variations (Taylor et al., 1983) documented in the Inyo Drilling Program provide an important framework with which to integrate the results of this study. Figure 77 shows porosity data for the distal drill core through Obsidian Dome. The plot shows three vesicular zones, corresponding to an upper finely vesicular pumice carapace, a central coarse pumice zone, and a lower coarse pumice zone. The central coarse pumice zone has slightly elevated H_2O contents ($\sim 0.4 \text{ wt}\%$; Taylor et al., 1983) relative to the rest of the section, which has only $0.1 \text{ wt}\%$. The elevated H_2O and bubble content of this layer may have effectively reduced the viscosity of the layer (e.g., Chapter III), thereby allowing the overlying obsidian and pumice layers to deform

independently from the base of the flow. Similar behavior may occur in the basal parts of the flow where a third pumiceous layer was detected. This decoupling of the flow may operate to form cavity structures and flow ridges.

Future work on obsidian domes should include detailed textural and chemical analysis of the four end-member lava types composing late Holocene obsidian flows. Efforts should be made to measure groundmass crystallinity in finely vesicular pumice and coarsely vesicular pumice to characterize possible differences in degassing histories (e.g., Fink and Manley, 1987). If indeed differences in microlite crystallinity reflect variations in eruptive parameters such as ascent rate, cooling history, and degassing, then quantifying textural variations may prove a useful tool for interpreting historic eruptions. Preliminary investigation suggests that coarsely vesicular pumice is relatively rich in microlites while finely vesicular pumice is microlite poor. The periodic distribution of these lava types suggests that eruptions may be pulsatory, or characterized by episodes of fast and slow extrusion. Bubble shapes in pumiceous lavas are a primary indication of the relative timing of vesiculation and flow. Finely vesicular pumice typically has flattened vesicles with pointed ends. These shapes suggest vesiculation during flow. In contrast, coarsely vesicular pumice typically has round vesicles, indicating vesiculation in the absence of a significant deformation field. The nature of color variation amongst the textural lava types is enigmatic in that the effects of light scattering, along with differences in groundmass crystallinity will give rise to observed color differences. Microstructural studies of the transition between the uppermost finely vesicular pumice layer and the subjacent obsidian layer may reveal clues to the location, timing, and extent of surficial vesiculation, as these are important parameters in the structural evolution of obsidian flows.

Continued research should be conducted on the contact between the upper obsidian layer and the overlying pumiceous carapace represents not only a thermal boundary, but also a mechanical boundary. At the contact, the deformation behavior changes from brittle

to ductile. This boundary is likely controlled by the relative rates of cooling and flow advance.

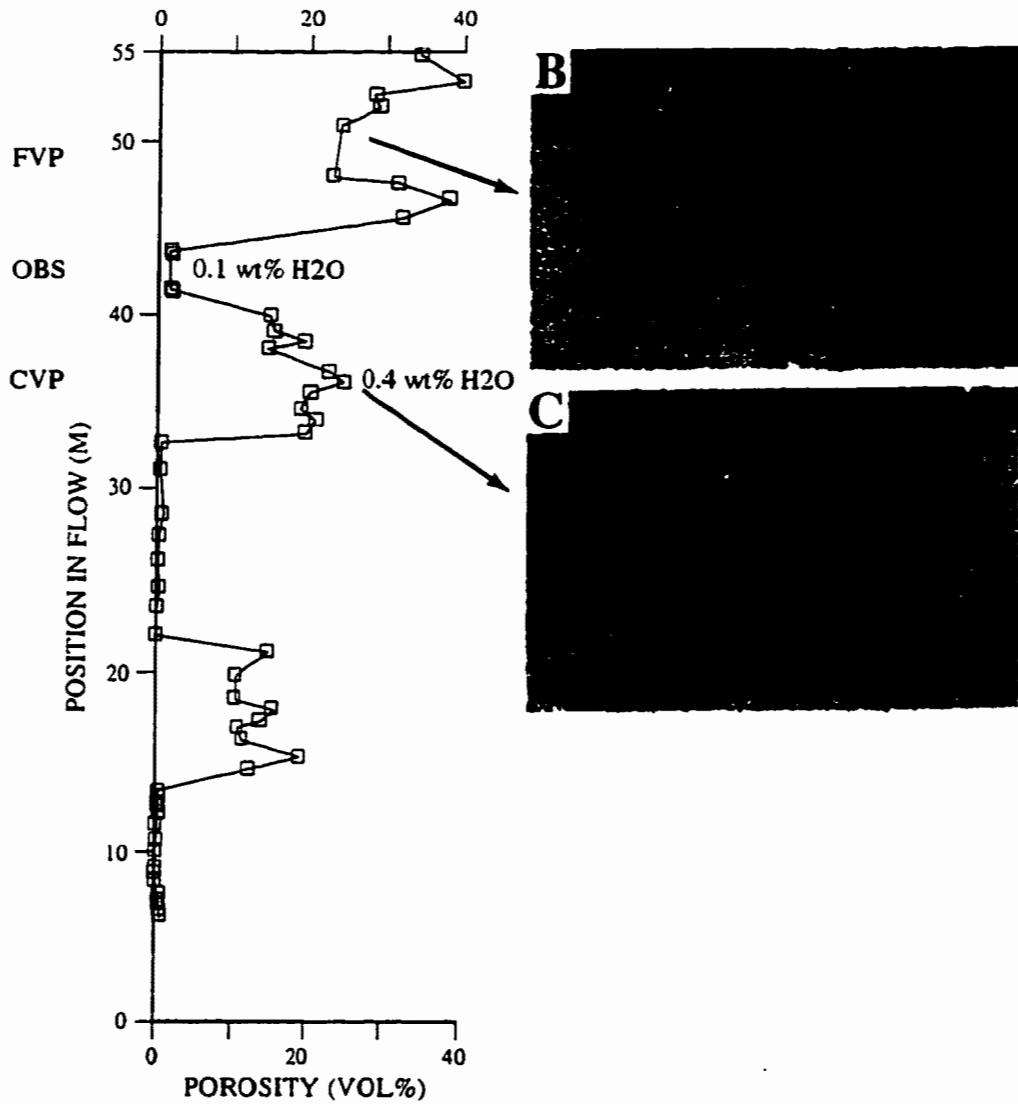


Figure 77. Cross section (A) of distal Obsidian Dome showing vesicular lavas found in RDO-2A drill core. Note vesicular zone at approximately 40 meters (corresponding to 20 meters depth). Elevated H₂O contents of this layer act to decrease effective viscosity and may promote deformation of the upper obsidian layer. From Fink et al. (1992).

APPENDIX

**MINERAL MYTHS: A BOOK THEME BY JON CASTRO AND
BRETAGNE HYGELUND**

The purpose of this Appendix is to document a works in progress on a geological novel authored by Bretagne Hygelund and Jonathan Castro. We believe the ideas herein to be original and therefore have placed this brief draft in this appendix for the purpose of copyright.

In the year 100,534 A.D. the world was a mysterious place, the people ever changing and evolving with the physical forces. The atmosphere surrounding the Earth consisted of a mixture of Helium, Nitrogen dioxide and Carbon dioxide. Continental configuration arose from many eons of drift and change within the Earth's soft interior. The scene is a coastline dotted with small worm like ridges and hills oriented west towards the ocean. In the valleys between these ridges lived bands of people, much evolved and in a sense much digressed. The people are warriors fueled by the urge to convert others to their cause. The cause: hydration.

The people of the ridge and valley province have bodies of flesh and bone yet in their eyes and grins lie vestiges of hydrous silicate minerals. Minerals incorporated into the soft tissue by many years of exposure to acid rain, extreme temperatures, and time. These minerals are serpentine, talc, tremolite, sericite and chrysotile. People of this mineral alteration live in the roots of ancient oceanic lithosphere, a land called *OPHIOS*. Depending on ones state of hydration, a dwellers role in this society may be that of ruler (very hydrated; due to ones existence through time) a serpentinite or of peasant palagonite (hydrated basaltic glass).

The leader of the people of ophios is Sebastian Serpentine. He rose through the ranks of service displaying a gift, an ability to convert humans of non-hydrous silicate affinity to hydrated minerals instantaneously by lancing them with fibrous needles of serpentine emanating from the tips of his fingers.

REFERENCES

- Anderson, S.W., and Fink, J.H., 1992. Crease structures: indicators of emplacement rates and surface stress regimes of lava flows. *Geological Society of America Bulletin* 104, 615-625.
- Bagdassarov, N. and Dingwell, D.B., 1992. A rheological investigation of vesicular rhyolite. *Journal of Volcanology and Geothermal Research* 50, 307-322.
- Bailey, R.A., 1982. Other potential eruption centers in California; Long Valley-Mono Lake, Coso, and Clear Lake volcanic fields, Status of Volcanic Prediction and Emergency Response Capabilities in Martin, R.C., and Davis, J.F. (ed.) Special publication of the California Department of Mines and Geology 63, 17-28.
- Biot, M.A., 1961. Theory of folding of stratified viscoelastic media and its implication in tectonics and orogenesis. *Geological Society of America Bulletin* 72, 1595-1620.
- Brantley, S., 1995. Volcanoes of the United States. U.S.G.S. general interest publication. 1-44.
- Cashman, K.V., 1988. Crystallization of Mount St. Helens 1980-1986 dacite: A quantitative textural approach. *Bulletin of Volcanology* 50, 194-209.
- Cashman, K.V., 1992. Groundmass crystallization of mount St. Helens dacite, 1980-1986: a tool for interpreting shallow magmatic processes. *Contributions to Mineralogy and Petrology* 109, 431-449.
- Cashman, K.V., and Marsh, B.D., 1988. Crystal size distribution (CSD) in rocks and the kinetics and dynamics of crystallization. II. Makaopuhi lava lake. *Contributions to Mineralogy and Petrology* 99, 292-305.
- Coward, M.P., 1980. The analysis of flow profiles in a basaltic dike using strained vesicles. *Journal of the Geological Society of London* 137, 605-615.
- Davis, G., 1989. *Structural Geology of Rocks and Regions*. John Wiley and Sons publishing, New York.
- Dobran, F., 1992. Nonequilibrium flow in volcanic conduits and application to eruptions of Mt. St. Helens on May 18, 1980, and Vesuvius in AD 79. *Journal of Volcanology and Geothermal Research* 49, 285-311.
- Eichelberger, J.C., Carrigan, C.R., Westrich, H.R., Price, R.H., 1986. Non-explosive silicic volcanism. *Nature* 323, 589-602.
- Eichelberger, J.C., Miller, C.D., and Younker, L.W., 1985. 1984 drilling results at Inyo Domes, California: EOS Transactions of the American Geophysical Union 66, 384.

- Eichelberger, J.C. and Westrich, H.R., 1981. Magmatic volatiles in explosive rhyolitic eruptions. *Geophysical Research Letters* 8, 757-760.
- Emerman, S.H. and Turcotte, D.L., 1984. A back-of-the-envelope approach to boudinage mechanics. *Tectonophysics* 110, 333-338.
- Fink, J.H., 1980. Surface folding and viscosity of rhyolite flows. *Geology* 8, 250-254.
- Fink, J.H., 1982. Surface Structure of Little Glass Mountain, In: Johnston, D.A. and Donnelly-Nolan, J., (Eds.), *Guides to Some Volcanic Terranes in Washington, Idaho, Oregon, and Northern California*. U.S.G.S. Survey Circular 838, pp. 171-176.
- Fink, J.H., 1983. Structure and emplacement of a rhyolitic obsidian flow: Little Glass Mountain, Medicine Lake Highland, northern California. *Geological Society of America Bulletin* 94, 362-380.
- Fink, J.H., 1984. Structural geologic constraints on the rheology of rhyolitic obsidian. *Journal of Non-crystalline Solids* 67, 135-146.
- Fink, J.H., Anderson, S.W., Manley, C.R., 1992. Textural constraints on silicic volcanism: beyond the permeable foam model. *Journal of Geophysical Research* 97, 77-88.
- Fink, J.H., and Fletcher, R.C., 1978. Ropy pahoehoe: Surface folding of a viscous fluid: *Journal of Volcanology and Geothermal Research* 4, 151-170.
- Fink, J.H. and Manley, C.R., 1987. Origin of pumiceous and glassy textures in rhyolite flows and domes. In: Fink, J.H., *The Emplacement of Silicic Domes and Lava Flows*. Geological Society of America Special Paper 212, pp. 77-89.
- Fink, J.H. and Manley, C.R., 1989. Explosive volcanic activity generated within advancing silicic lava flows, in *Volcanic Hazards*, edited by J. Latter, International Association of Volcanology and Chemistry of the Earth's Interior Proceedings in Volcanology 1, 169-179.
- Fink, J.H., and Pollard, 1983. Structural evidence for dikes beneath silicic domes, Medicine Lake Highland Volcano, California. *Geology* 11, 458-461.
- Geshwind, C., and Rutherford, M.J., 1995. Crystallization of microlites during magma ascent: the fluid mechanics of recent eruptions at Mount St. Helens. *Bulletin of Volcanology* 57, 356-370.
- Groshong, R.H., 1975. Strain, fractures, and pressure solution in natural single-layer folds. *Geological Society of America Bulletin* 86, 1363-1376.
- Hammer, J.E., Cashman, K.V., Hoblitt, R.P., and Newman, S., 1999. Degassing and microlite crystallization during pre-climactic events of the 1991 eruption of Mt. Pinatubo, Philippines. *Bulletin of Volcanology* 60, 355-380.
- Hess, K.U., and Dingwell, D.B., 1996. Viscosities of hydrous leucogranitic melts: A non-Arrhenian model. *American Mineralogist* 81, 1297.

- Higgins, M.D., 1994. Numerical modeling of crystal shapes in thin sections: estimation of crystal habit and true size. *American Mineralogist* 79, 113-119.
- Higgins, M.D., 1998. CSD corrections: the right way and wrong way to do crystal size distributions. Geological Society of America abstracts with programs.
- Houghton, B.F., Wilson, C.J.N., Hassan, M., 1988. Density measurements for pyroclasts and pyroclastic rocks. *New Zealand Geological Survey Record* 35, 73-76.
- Jaupart, C. and Allegre, C.J., 1991. Gas content, eruption rate and instabilities of eruption regime in silicic volcanoes. *Earth and Planetary Science Letters* 102, 413-429.
- Jensen, R.A., 1993. Explosion craters and giant gas bubbles on Holocene rhyolite flows at Newberry Crater, Oregon. *Oregon Geology* 55, 13-19.
- Johnson, A.M. and Fletcher, R.C., 1994. *Folding of Viscous Layers*. Columbia University Press, New York.
- Ghosh, S.K., Mandal, N., Sengupta, S., 1993. Superposed buckling in multilayers. *Journal of Structural Geology* 15, 95-111.
- Kushiro, I., 1975. On the nature of silicate melt and its significance in magma genesis: regularities in the shift of the liquidus boundaries involving olivine, pyroxene, and silicate minerals. *American Journal of Science* 275, 411-431.
- Lofgren, G. 1971. Experimentally produced devitrification textures in natural rhyolitic glass. *Geology Society of America Bulletin* 82, 111-124.
- Lofgren, G. 1974. An experimental study of plagioclase crystal morphology: Isothermal crystallization. *American Journal of Science* 274, 243-273.
- Lofgren, G. 1980. Experimental studies on the dynamic crystallization of silicate melts. In: R. Hargraves (ed.) *Physics of magmatic Processes*, Princeton University Press, Princeton, NJ, pp. 487-551.
- MacLeod, N.S., and Sherrod, D.R., 1988, Geologic evidence for a magma chamber beneath Newberry volcano, Oregon. *Journal of Geophysical Research*, 93, no. B9, 10,067- 10,079.
- MacLeod, N.S., Sherrod, D.F., and Chitwood, L.A., 1982. Geologic map of Newberry Volcano, Deschutes, Klamath, and Lake Counties, Oregon: U.S.G.S. Open-File Report 82-847, scale 1:62,500.
- Manga, M., 1998. Orientation distribution of microlites in obsidian. *Journal of Volcanology and Geothermal Research* 86, 107-115.
- Manga, M., Castro, J.M., Cashman, K.V., Loewenberg, M., 1998. Rheology of bubble-bearing magmas. *Journal of Volcanology and Geothermal Research* 87, 15-28.
- Manley, C.R. and Fink, J.H., 1987. Internal textures of rhyolite flows as revealed by research drilling. *Geology* 15, 549-552.

- Marsh, B., 1988. Crystal size distributions (CSD) in rocks and the kinetics and dynamics of crystallization I: Theory. *Contributions to Mineralogy and Petrology* 99, 277-291.
- Miller, C.D., 1985. Holocene eruptions at the Inyo volcanic chain, California: Implications for possible eruptions in Long Valley Caldera. *Geology* 13, 14-17.
- Murase, T. and McBirney, A.R., 1973. Properties of some common igneous rocks and their melts at high temperatures. *Geological Society of America Bulletin* 84, 3563-3592.
- Nakada, S., 1992. Lava domes and pyroclastic flows of the 1991-1992 Eruption at Unzen volcano. in Yangi, T., Okada, H., and Ohta, K. (ed) *Unzen Volcano. The Nishinippon&Kyushu University Press.* 56-66
- Nakada, S., Miyake, Y., Sato, H., Oshima, O., Fujinawa, A., 1995. Endogenous growth of dacite dome at Unzen volcano Japan. *Geology* 23, 157-160.
- Naney, M.T., 1983. Phase equilibria of rock-forming ferromagnesian silicates in granitic systems. *American Journal of Science* 283, 993-1033.
- Naney, M.T., and Swanson, S.E., 1980. The effect of Fe and Mg on crystallization in granitic systems. *American Mineralogist* 65: 639-653.
- Nichols, R.L., 1941. The velocity of the Big Obsidian Flow, Bend, Oregon. *Transactions of the American Geophysical Union* , 504-505.
- Peterson, T.D., 1996. A refined technique for measuring crystal size distributions in thin section. *Contributions to Mineralogy and Petrology* 124, 395-405.
- Pollard, D.D., Fink, J.H., and Delaney, P.T., 1984. Igneous dikes at Long Valley, CA: Emplacement mechanism and associate geologic structures, U.S.G.S. Open File Report, 84-939, 130-144.
- Ramberg, H., 1960. Relationship between length of arc and thickness of pygmatically folded veins. *American Journal of Science* 258, 36-46.
- Ramberg, H., 1963. Strain distribution and geometry of folds. *Uppsala University Geology Institute Bulletin* 42, 1-20.
- Ramsay, J.G. and Huber, M., 1987. *The Techniques of Modern Structural Geology. Volume 2: Folds and Fractures.* Academic Press, London.
- Randolf, A.D., and Larson, M.A., 1971. *Theory of particulate processes.* Academic Press, New York, 251 pp.
- Russell, I.C., 1905. Preliminary report of the geology and water resource of central Oregon: *U.S.G.S Bulletin* 252, 138p.
- Sampson, D.E., 1987. Textural heterogeneities and vent area structures in the 600-year-old lavas of the Inyo volcanic chain, eastern California: *Geological Society of America Special Paper* 212, 89-101.

- Sampson, D.E., and Cameron, K.L., 1987. The geochemistry of the Inyo volcanic chain: multiple magma systems in the Long Valley Region, eastern California. *Journal of Geophysical Research* 92, 10,403-10,421.
- Sharp, T., Stevenson, R., and Dingwell, D., 1996. Microlites and "nanolite" in rhyolitic glass: microstructural and chemical characterization. *Bulletin of Volcanology* 57, 631-640.
- Shaw, H.R., 1972. Viscosities of magmatic silicate liquids: an empirical method of prediction. *American Journal of Science* 266, 225-264.
- Shelley, D., 1985. Determining paleo-flow directions from groundmass fabrics in the Lyttelton radial dykes, New Zealand: *Journal of Volcanology and Geothermal Research* 25, 69-79.
- Sibree, J.O., 1933. The viscosity of froth. *Transactions of the Faraday Society* 28, 325-331.
- Smith, R.B., 1975. A unified theory of the onset of folding, boudinage, and mullion structure. *Geological Society of America Bulletin* 86, 1601-1609.
- Smith, R.B., 1977. Formation of folds, boudinage, and mullions in non-Newtonian materials. *Geological Society of America Bulletin* 88, 312-320.
- Smith, R.B., 1979. The folding of a strongly non-Newtonian layer. *American Journal of Science* 279, 272-287.
- Smith, J.V. and Houston, H.C., 1994. Folds produced by gravity spreading of a banded rhyolite flow. *Journal of Volcanology and Geothermal Research* 63, 89-94.
- Spera, F.J., Borgia, A., Strimple, J., Feigenson, M.D., 1988. Rheology of melts and magmatic suspensions: Design and calibration of concentric cylinder viscometer with application to rhyolitic magma. *Journal of Geophysical Research* 93, 10,273-10,294.
- Stein, D.J. and Spera, F.J., 1992. Rheology and microstructure of magmatic emulsions: theory and experiments. *Journal of Volcanology and Geothermal Research* 49, 157-174.
- Stevenson, R.J., Briggs, R.M., and Hodder, A.P.W., 1993. Emplacement history of a low-viscosity, fountain-fed pantelleritic lava flow. *Journal of Volcanology and Geothermal Research* 57, 39-56.
- Swanson, D.A., and Holcomb, R.T., 1990. Regularities in Growth of the Mount St. Helens Dacite Dome, 1980-1986. in J. Fink (ed.) *Lava Flows and Domes Emplacement Mechanisms and Hazard Implications*.
- Swanson, S.E., 1977. Relation of nucleation and crystal-growth rate to the development of granitic textures. *American Mineralogist* 62, 966-978.
- Swanson, S.E., Naney, M.T., Westrich, H.R., Eichelberger, J.C., 1989. Crystallization history of Obsidian Dome, Inyo Domes, California. *Bulletin of Volcanology* 51, 161-176.

- Taylor, B.E., 1991. Degassing of Obsidian Dome rhyolite, Inyo volcanic chain, California. *Stable Isotope Geochemistry: A Tribute to Samuel Epstein*. The Geochemical Society, Special Publication No. 339-353.
- Underwood, E.E., 1970. *Quantitative Stereology*. Addison-Wesley Reading, Mass.
- Vogel, T.A., Eichelberger, J.C., Younker, L.W., Schuraytz, B.C., Horkowitz, J.P., Stockman, H.W., Westrich, H. R., 1989. Petrology and emplacement dynamics of intrusive and extrusive rhyolites of Obsidian Dome, Inyo Craters Volcanic Chain, Eastern California. *Journal of Geophysical Research* 94, 17,937-17956.
- Vogel, T.A., Younker, L.W., Schuraytz, B.C., 1987. Constraints on magma ascent, emplacement and eruption: Geochemical and mineralogical data from drill-core samples at Obsidian Dome, Inyo Chain, California. *Geology* 15, 405-408.
- Webb, S.L. and Dingwell, D.B., 1990. Non-Newtonian rheology of igneous melts at high stresses and strain rates: Experimental results for rhyolite, andesite, basalt, and nephelinite. *Journal of Geophysical Research* 95, 15,659-15,701.
- Westrich, H.R., Stockman, H.W., and Eichelberger, J.C., 1988. Degassing of rhyolitic magma during ascent and emplacement. *Journal of Geophysical Research* 93, 6503-6511.
- Williams, H., 1935. Newberry volcano of central Oregon: *Geological Society of America Bulletin* 46, 253-304.
- Wylie, J.J. and Lister, J.R. 1998. Stability of straining flow with surface cooling and temperature-dependent viscosity. *Journal of Fluid Mechanics* 365, 369-381.